Mémoire

Auteur : Hemmen, Elise
Promoteur(s) : Jehin, Emmanuel
Faculté : Faculté des Sciences
Diplôme : Master en sciences spatiales, à finalité approfondie
Année académique : 2023-2024
URI/URL : http://hdl.handle.net/2268.2/21540

Study of the activity and composition of the periodic comets 67P/Churyumov-Gerasimenko and 103/Hartley 2 at two different perihelion passages with the TRAPPIST telescopes

Hemmen Elise

Supervisor: Dr. Emmanuel Jehin

Master in Space Sciences, Research focus
Faculty of Sciences
Université de Liège

Academic year 2023-2024

Contents

Acknowledgements

This work is the completion of five long years of study in Chemistry and Space Sciences. I sincerely wish to thank all the people who have accompanied me on this journey, and in particular those who have contributed, directly or indirectly, to the completion of this work.

First and foremost, many thanks to my supervisor, Emmanuel Jehin. His expertise and passion for the study of comets have been a true source of inspiration. I am grateful to him for introducing me to this fascinating field, as well as for mentoring and guiding me throughout this project. His encouragement and insightful advice have significantly helped me to progress. I would also like to thank Mathieu Vander Donckt, whose invaluable assistance was of great help at many stages of this work. His advice, technical expertise, and most importantly, his patience in the face of the numerous challenges encountered during data reduction, were crucial to the completion of this work. I am particularly grateful for the time he devoted to carefully reading and correcting the first version of this thesis, thereby contributing to its improved quality. I also wish to express my gratitude to the members of my reading committee, Hervé Lamy, Bertrand Bonfond, and Benoit Hubert. Thank you to each of them for dedicating some of their time to reading and evaluating this work.

And above all, a thousand thanks to the Didiers, my companions on this journey throughout the year. More than just office colleagues, they have been my best friends, sharing the joys and challenges of this journey. Their unwavering support has been invaluable. The lunch breaks, coffee breaks, and countless moments of laughter we shared made this year memorable and much more enjoyable. I extend a heartfelt thank you to them for their simple presence and friendship. They have made the success of this project even more rewarding, and I sincerely hope to share my future career in Space Sciences with them.

Introduction

Among all the objects in the Solar System, comets - fascinating and mysterious celestial objects - are probably the ones that have most captivated human minds and imaginations. Their nature has remained misunderstood for centuries. Their unpredictable appearance in the night sky in the form of spectacular streaks of light was long seen as an ominous sign of impending disaster. However, the evolution of scientific knowledge has profoundly transformed our understanding of these celestial bodies. The advent of modern science, thanks in particular to the work of pioneers such as Isaac Newton and Edmund Halley, has revealed the true nature of comets as celestial bodies orbiting the Sun.

Comets play a crucial role in exploring the history of the Solar System, as they are considered to be its most primitive objects. Formed around 4.6 billion years ago, cometary nuclei have been preserved in the cold, remote regions of the Solar System, retaining their original chemical composition almost intact. Mainly under the influence of gravitational forces, some of these nuclei are sometimes deflected towards the Sun. As they approach, solar heat sublimates the ices they contain, releasing grains of cometary dust and creating a vast luminous envelope around the nucleus, known as the coma. This coma is very bright, making it easy to observe and analyze from Earth. The study of comets is a key branch of astronomy, since it offers a unique window on the conditions and chemical composition of the regions of the Solar System where they formed. It is in this context that this research project is being carried out. It aims to deepen our understanding of comets through the analysis of observational data from two Jupiter-family comets already visited by space missions: comet 67P/Churyumov-Guerasimenko, visited in 2014 and 2015 by ESA's Rosetta probe, and comet 103P/Hartley 2, visited in 2010 by NASA's EPOXI probe.

These two comets were intensively observed in the visible domain during two separate passages close to the Sun, using the twin 60-cm TRAPPIST telescopes. The latter are equipped with the Johnson-Cousins broad-band filters, as well as with a narrow-band filter set designed for cometary observations. The large number of high-quality images collected during the surveys enabled us to analyze the comets' magnitudes, measure the production rates of some gaseous molecules (OH, NH, CN, C_2, and C_3) in the comae, and quantify the dusty activity around the cometary nuclei. The

main objective of this work was to compare the data obtained during these two passages, in order to assess possible variations in cometary activity from one perihelion passage to the next.

The first chapter gives a brief introduction to comets. We address the composition of cometary nuclei, their origin and formation process, and we emphasize the mechanism of formation of the coma and tails when they approach the Sun. We also describe the different types of comets and their respective reservoir in the Solar System. The second chapter is related to the observation methods and conditions. We start by giving a detailed description of the TRAPPIST telescopes, and then we present our target comets and their orbital properties. The results of our photometric analysis of the comets are given in Chapter 3. We first explain in detail the processes of data reduction and flux calibration. Then, we discuss the light curves obtained for each comet and analyze the colors of their coma. In chapter 4, we describe the Haser model, widely used by astronomers for the computation of cometary gas production rates, and we present our results obtained on the basis of this simplistic model. We also classify the comets according to their chemical composition. In chapter 5, we analyse the dust activity of comets through the calculation of the so-called "Afrho" parameter, and we compute dust-to-gas ratios in order to evaluate their dust content. Finally, we performe an analysis of comae's morphological features. The resulting images are presented and discussed in chapter 6.

Chapter 1

Theoretical concepts about comets

Humans have long been interested in comets. Since the brightest comets can be seen in the sky with the naked eye, the first observations of these bodies date back to Antiquity, well before the telescope invention. People were afraid of these unknown objects. Seen as bright fireballs passing through the night sky, they were interpreted as bad omens or signs indicating an upcoming disaster.

Over time, scientists have observed a large number of comets, and their ideas about the nature of these objects evolved significantly, from wandering planets passing near the Earth to meteorological phenomena happening in the atmosphere. Actually, the real cometary science began at the end of the seventeenth century, thanks to the British astronomers Isaac Newton and Edmund Halley. They made an important insight by realizing that, actually, comets are celestial bodies in orbit around the Sun (De Pater, Lissauer, 2015; Festou et al., 2004).

1.1 The comet nucleus

Comet nuclei are small frozen celestial bodies, composed of dust grains and volatile chemical compounds (mainly water) in the form of ices. They are often called "dirty snowballs", with reference to the first physically correct model describing the formation and composition of comets, which was proposed by Fred Whipple in 1950 (Whipple, 1950). However, the term "ball" is not really appropriate for describing comet nuclei because, in reality, these objects are not spherical at all, but rather have an irregular shape. Regarding their physical characteristics, they are generally quite small, measuring from a few hundred meters to a few kilometers in diameter, and have a high degree of porosity (Thomas, 2020; Meierhenrich, 2014). They have a very dark rocky surface, their albedo being typically lower than 0.1 in the visible domain (Lamy et al., 2004).

These small bodies are thought to have formed at the time of the birth of the Solar System, 4.6

billion years ago, due to accretion processes that occurred in some regions of the protoplanetary nebula. According to the observed structure and composition of comets, the places in which they formed probably displayed specific physical properties. First, the temperature should be low enough to enable the existence of water ice, but still greater than 25 K, as indicated by the absence of highly volatile species in the composition of cometary nuclei. Then, the density should be high enough such that some accretion processes could occur and give rise to kilometer-sized bodies. These temperature and density requirements might both have been met in the outer parts of the solar nebula. In these regions, microscopic particles of dust and frozen water in movement might have collided and agglomerated, producing bigger and bigger porous bodies on which gases of other elements were condensing and accumulating. Finally, these processes might have resulted in the formation of comets. Since then, the icy planetesimals have remained in the coldest and most isolated regions of the Solar System. They have been traveling on very large and eccentric orbits, and most of the time, they have thus been located far from the Sun. Consequently, they have conserved their ices and have nearly not undergone any physicochemical processes likely to alter their composition.

Due to their good preservation, comets are considered the most primitive objects in the Solar System. Their composition is thought to be representative of the solar nebula's material, hence the interest in studying these small celestial bodies. Indeed, they could provide some clues about the chemical composition of the regions where they formed in the protoplanetary nebula, as well as the conditions that were prevailing in the early Solar System. (Meierhenrich, 2014; Weidenschilling, 2004).

1.2 The coma and tails

When a cometary orbit is perturbed (generally because of gravitational effects, see below), the nucleus can enter the inner Solar System. Consequently, it progressively heats up as it approaches the Sun. Once the heliocentric distance becomes small enough, the ices contained inside the comet sublimate and escape from the nucleus by taking away some light cometary dust grains on their path. This leads to the formation of a large atmosphere of gas and dust particles, called the coma, which surrounds the nucleus and can have a diameter reaching 10^5 km. The comet is then said to be active.

When a comet is active, the dust grains released in the coma are pushed away from the Sun because of the solar radiation pressure. Therefore, a tail formed of these grains, called the dust tail, appears. This tail can extend up to 10^7 km, and bends in the opposite direction to the comet motion, as a result of the angular momentum conservation principle. Moreover, since the constituting dust grains reflect sunlight, the tail displays a white color corresponding to the emission continuum of the solar spectrum. In addition to this curved white tail, another tail can be observed.

This one is called the ion tail or plasma tail since it is formed of the ions present in the coma. These ionic species originate from the photo-reaction processes occurring due to the high-energy photons emitted by the Sun that interact with the gaseous molecules. Once ionized, the species are taken away by the solar wind, thus forming a tail oriented in the anti-solar direction. This ion tail can be distinguished from the dust tail because it is generally thinner but more extended. It can indeed reach 10^8 km long. Moreover, unlike the dust tail, it displays a bluish color due to the fluorescence processes of CO^+ ions, which are part of the primary components of cometary plasma tails.

These two long tails are specific to comets and allow their distinction among all small bodies of the Solar System, especially asteroids. For that matter, the word "comet" originates from the Greek word "$\kappa o \mu \eta \tau \eta \varsigma$" ("kometes"), which literally signifies "long hair", in reference to the most prominent characteristic of these bodies.

Finally, when a comet is observed from space, an additional feature can be seen around it: the hydrogen envelope. Indeed, as cometary ices are mostly composed of water, gaseous H_2O molecules are very numerous in the coma. Their dissociation by solar UV photons leads to the production of hydrogen atoms. Because the latter are much lighter than the other atoms and molecules present in the coma, they can travel over longer distances before being ionized by energetic photons and then carried away by the solar wind. This results in the formation of a hydrogen cloud around the nucleus, much larger than the coma. Its diameter can reach 10^7 km. However, despite its imposing size, this cloud can only be observed with spatial satellites, because H atoms only emit in the ultraviolet domain. Since UV photons are absorbed by the terrestrial atmosphere, they can not be observed from the surface of the Earth (De Pater, Lissauer, 2015).

Figure 1.1 displays a schematic representation of an active comet, showing its nucleus, coma, tails, and hydrogen cloud, as well as an image of a long-period comet, on which the coma and tails can be identified.

At large distances from the Sun, comets' parent bodies are usually not visible. On the contrary, active comets are very bright and can easily be observed. This is because the dust grains of the coma reflect and scatter solar light much more intensively than the low-albedo surface of the nucleus. As a consequence, while a comet approaches the Sun, its coma and tails extend and thus, it progressively becomes brighter, reaching a maximum brightness near the perihelion (i.e., the closest point to the Sun in the comet orbit). Then, the comet goes back to colder regions and gets fainter as the coma and tails disappear. It has been observed that most comets display a significant increase in their brightness when they are localized at less than 3 astronomical units (AU) from the Sun. In addition to their lower magnitude, comets in activity are easy to identify in the sky. Indeed, the comae give comets a fuzzy appearance, making them distinguishable from the background stars when observed

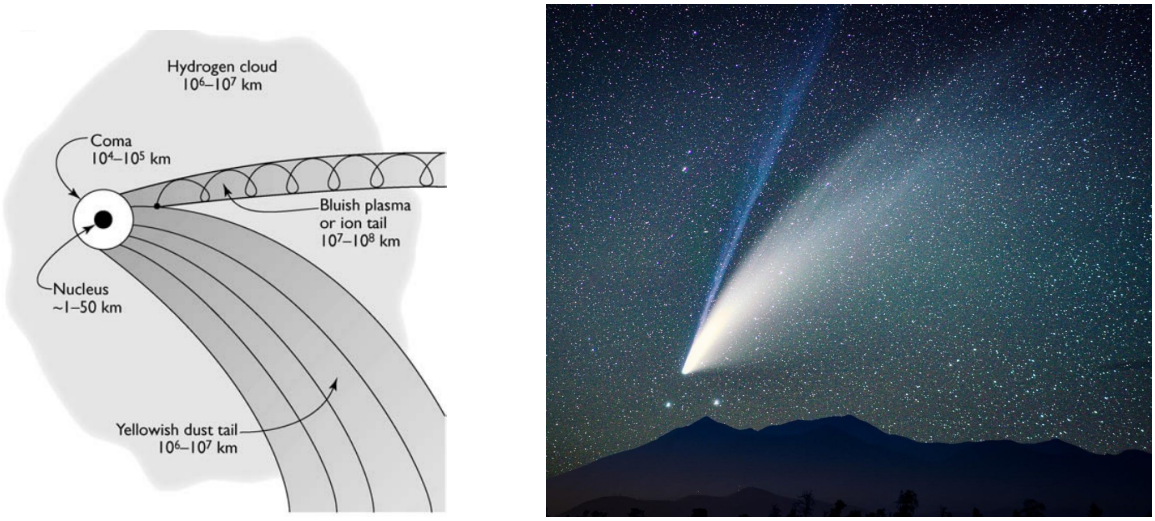

Figure 1.1. Left: Schematic representation of an active comet (De Pater, Lissauer, 2015). Right: Long-period comet C/2020 F3 (NEOWISE) during its passage close to the Earth in July 2020 (picture taken above San Fransisco by K. Schindler from Lowell Observatory).

through a telescope. However, comae also hide cometary nuclei, hence the difficulty of determining accurately their size and chemical composition through remote observations (De Pater, Lissauer, 2015; Meierhenrich, 2014).

Thus, the presence of the coma prevents a direct determination of the chemical composition of cometary nuclei. Nevertheless, the nucleus composition can still be inferred from spectroscopic analysis of the gas composition of the coma. Actually, in the visible domain, a few chemical components can be identified in comae. They correspond to daughter (or granddaughter) species, originating from parent species that were part of the cometary ice composition, and that have been transformed in the coma due to photodissociation and photoionization processes. For instance, the H_2, H, O, and OH daughter species found in cometary comae come from the frozen water present in large quantities in the nucleus. In addition, carbonated, nitrated, and a few sulfured species can be observed, along with their associated ions. Finally, some heavier elements such as alkalies and metals have also been identified in the visible range in some comae. All these atoms, molecules, and ions might be the fragments of various parent molecules such as H_2O, CO_2, CH_4, HCN, NH_3, N_2, and many others, even implying more complex organic species. These parent species can be observed at larger wavelengths, especially in the infrared and sub-millimeter domains. Actually, more than 100 parent species have been identified in cometary comae so far, while the daughter species observed at visible wavelengths only constitute a minor part of the molecular composition, according to current knowledge (Swamy, 2010; Cochran et al., 2015).

1.3 The different comet types

Comets can be divided into two main classes, according to their orbital period. Comets whose orbital period is shorter than 200 years are called short-period comets (or periodic comets), while comets that have a longer orbital period are called long-period comets (or non-periodic comets). The periodicity of comets was discovered in 1704 by the British astronomer Edmond Halley. He published a classification of the orbital parameters of twenty-four observed comets and realized that, among these objects, the three comets observed respectively in 1531, 1607, and 1682 might correspond to one single object traveling on an elliptical orbit. He then predicted the following return of the comet in 1758, and his theory was confirmed when the comet was observed at the expected moment. This comet, known as comet 1P/Halley, is now famous and displays a periodicity of a bit less than 76 years. Since Halley's discovery, astronomers have been able to predict the appearance of short-period comets in the inner planetary region of the Solar System.

Another classification method, based on the dynamical properties of small bodies (comets and asteroids) is also widely used. This classification makes use of the Tisserand parameter, which is a quantity defined by Carusi, Valsecchi (1987) to describe the orbital motion of an object with respect to a planet. For comet classification, the Tisserand parameter is calculated with respect to Jupiter, and is given by

$$T_J = \frac{a_J}{a} + 2\sqrt{\frac{a}{a_J}(1-e^2)}\cos i \tag{1.1}$$

where a, e, and i are respectively the semi-major axis (in AU), eccentricity, and inclination (in degrees) of the comet's orbit, and a_J is the semi-major axis of Jupiter's orbit ($a_J = 5.2$ AU).

Comets can be separated into two families depending on the value of their Tisserand parameter. In general, they have a T_J value lower than 3 (contrarily to asteroids). On one hand, comets characterized by $2 < T_J < 3$ are called ecliptic comets. They are all gathered in a range of low orbital inclinations (median inclination of about 11°) with respect to the ecliptic plane. On the other hand, nearly isotropic comets are characterized by $T_J < 2$, and have higher orbital inclinations than ecliptic comets (De Pater, Lissauer, 2015; Meierhenrich, 2014; Thomas, 2020). The first category notably includes the so-called "Jupiter-family comets" (JFCs). This branch gathers comets that typically display a very short orbital period of less than 20 years, and whose aphelion is located near Jupiter's orbit. Consequently, they have a strong connection with Jupiter (hence their name). Actually, their orbit is controlled by the gravitational attraction of the giant planet. This work mainly focuses on this type of comet.

1.4 Reservoirs of comets

Comets might be much more numerous than any other type of object in the Solar System. They originate from two different reservoirs: the Oort cloud and the Kuiper belt (De Pater, Lissauer, 2015; Meierhenrich, 2014). Figure 1.2 shows an illustration of these two reservoirs.

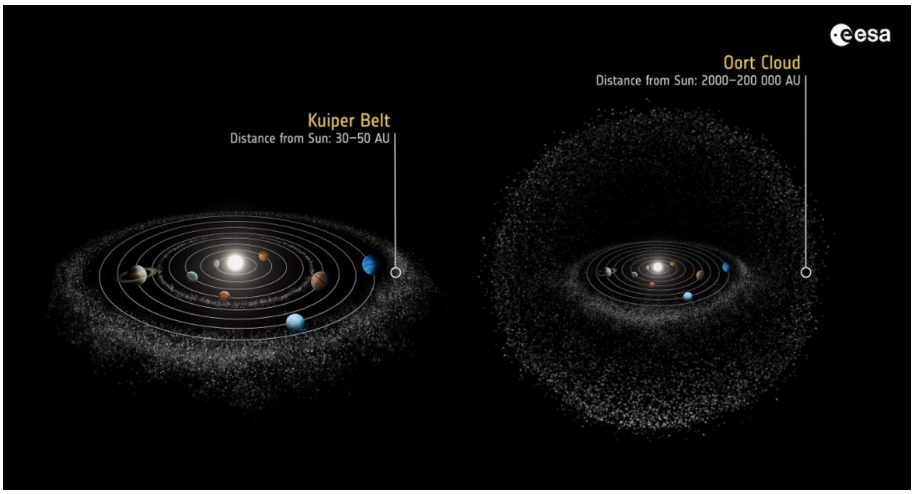

Figure 1.2. Illustration of the Kuiper belt and Oort cloud. The image was taken from ESA's website (`https://www.esa.int/ESA_Multimedia/Images/2014/12/Kuiper_Belt_and_Oort_Cloud_in_context`).

The Oort cloud is a hypothetical huge spherical region surrounding the whole Solar System. This region owes its name to the Dutch astronomer Jan Oort, who first postulated its existence in 1950, in order to explain the origin of long-period comets. It has never been directly observed, but it is thought to be formed of more than 10^{12} comets and to extend from about 20,000 AU to more than 200,000 AU from the Sun. Actually, the Oort cloud is considered the most distant region of the Solar System. Comets' parent bodies that originate from this reservoir have probably formed in the same region as giant planets, and have then been ejected toward more distant regions due to some gravitational perturbations caused by giant planets. Indeed, the very low gas and dust particle density in the external part of the protoplanetary nebula (corresponding now to the location of the Oort cloud) could not have allowed the formation of planetesimals of such a size. Now, these bodies are orbiting the Sun on very large and extremely eccentric orbits, that can have any inclination with respect to the ecliptic plane, as a result of the spherical shape of the reservoir. Their orbit is sometimes subject to change. The main reason for this perturbation is the galactic tidal field, but it can also be due to the passage of nearby stars or the approach of a giant molecular cloud. When this occurs, comets might enter the inner Solar System from any direction, consequently to their randomly inclined orbit trajectory, and thus pass near the planetary region. When they are observed during their passage close to the Sun, their orbit is so eccentric that they seem to follow a parabolic trajectory. Finally, they leave the inner Solar System and return to distant regions for

a long period of time. Basically, the Oort cloud is the reservoir of long-period comets and some short-period comets (the so-called "Halley-type comets").

The Kuiper belt is an annulus-shaped region made of thousands of asteroids, comets, and a few dwarf planets. All these celestial bodies are referred to as transneptunian objects. Astronomers started to believe in the existence of the belt in 1930, after the discovery of the dwarf planet Pluto, localized in this region. However, the first observations that confirmed it only occurred more than sixty years later. Oddly, it was called after the Dutch astronomer Gerard Kuiper who proposed, in the 1950's, the hypothesis that a region made of small bodies and containing Pluto might indeed have existed billion years ago, but the comets and asteroids might have then been ejected outside the Solar System because of the dwarf planet. According to his theory, the belt would thus no longer exist today. Actually, this region is localized beyond the orbit of Neptune and extends from about 30 to 50 AU from the Sun. Comets' parent bodies coming from this region display a low orbital inclination with respect to the ecliptic plane, and a much smaller orbital eccentricity than Oort cloud's comets. Moreover, most of them have a prograde direction of rotation around the Sun. Gravitational interactions with the giant planets, especially Neptune, can perturb their trajectory in the Kuiper belt and cause them to enter the planetary region. JFCs, which constitute the major part of short-period comets, are thought to originate from this region.

Chapter 2

Observations

All the comet images used in this work were obtained using the TRAPPIST telescopes of the University of Liège. This chapter provides a description of the telescopes, with an emphasis on the high-quality filters they are equipped with, specially designed for comet observations. Moreover, two Jupiter-family comets were analyzed based on images obtained during two different passages close to the Sun. The two targets are briefly presented at the end of this chapter.

2.1 TRAPPIST

The TRAPPIST (TRAnsiting Planets and PlanetesImals Small Telescope)[1] project is led by the group COMETA (COmets METeors and Asteroids) of the Department of Astrophysics, Geophysics and Oceanography (AGO) of the University of Liège (Jehin et al., 2011). It is dedicated, on the one hand, to the detection of transiting exoplanets, and on the other hand, to the study of the Solar System planetesimals such as comets and asteroids. TRAPPIST consists of a pair of twin telescopes: TRAPPIST-South (hereafter TS) and TRAPPIST-North (hereafter TN). Together, they allow to conduct observations both from the South and the North hemispheres of the Earth. TS is located in Chile, in the Atacama desert. It was installed in 2010 at the ESO's La Silla Observatory, at an altitude of 2315 meters. TN is located in Morocco, in the Atlas Mountains. It was installed in 2016 at the Oukaïmeden Observatory, at an altitude of 2751 meters (Figure 2.1).

TS and TN are 60-cm robotic telescopes of the Ritchey-Chrétien type. They were built by the German company ASTELCO and placed on an equatorial mount designed by the company, allowing accurate target pointing and tracking. The telescope functioning is completely automatized thanks to computer programs, and the observations can be remotely launched from the University of Liège. The 5-meter dome covering both telescopes opens at sunset, and a meteorological station

[1]TRAPPIST website: `https://www.trappist.uliege.be/`

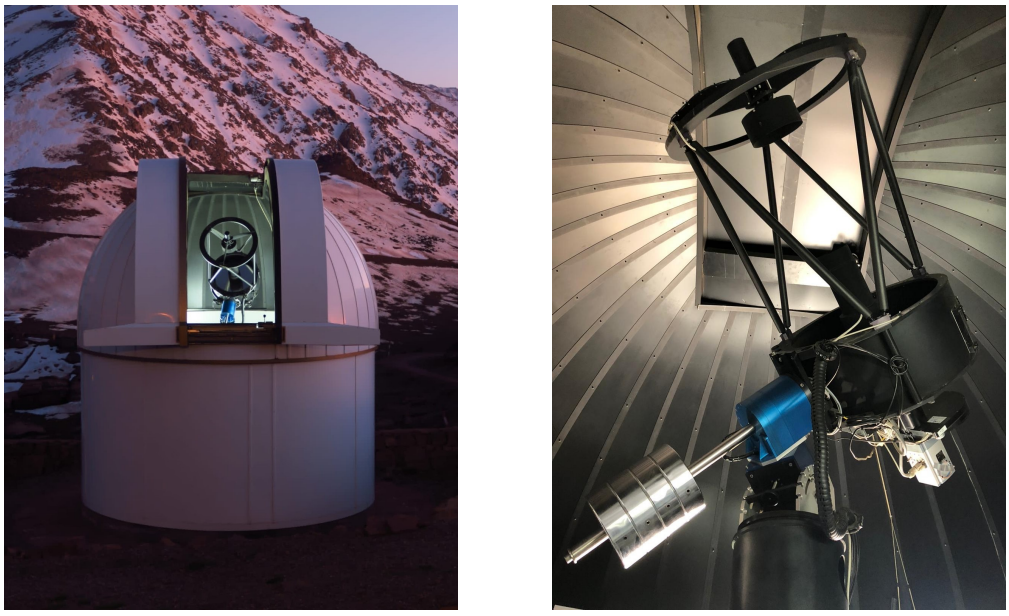

Figure 2.1. Left: TRAPPIST-North seen from the exterior, with dome open. Right: TRAPPIST telescope inside the dome.

permanently records the weather conditions to ensure its closing in case of bad conditions (rain, snow, or strong wind).

Both telescopes are equipped with a highly sensitive CCD camera of 2048 × 2048 15-µm pixels, covering a field of view of 22 × 22 arcminutes. The camera includes a double filter wheel that can hold several different filters. The first wheel contains filters meant to isolate broad wavelength bands. These are the four Johnson-Cousins filters for visible and near-infrared light (B, V, R, and I), the Sloan filter z, and a special filter provided for exoplanet transit observations (I + z). However, for this work, only data obtained with the Johnson-Cousins filters were used. Their transmission profiles are shown in Figure 2.2. With TRAPPIST, observations with these filters are generally performed according to the following sequence: R, B, R, V, R, I, R. The repetitive observations with the R filter are necessary to verify the atmospheric conditions during the observations (i.e., the absence of clouds), by checking that the light flux measured with a given filter remains unchanged throughout the observation night.

On the second filter wheel, a Hale-Bopp (HB) high-quality filter set is loaded (Farnham et al., 2000). This set was specially designed by NASA for cometary observations and is so called because it was initially intended for the observation of Comet Hale-Bopp, during its passage at perihelion in 1997. The HB filters are very useful for calculating some parameters such as the cometary gas production rates and dust outgassing. Indeed, they enable the isolation of narrow wavelength bands that correspond, on one hand, to the main emission bands observed in the optical spec-

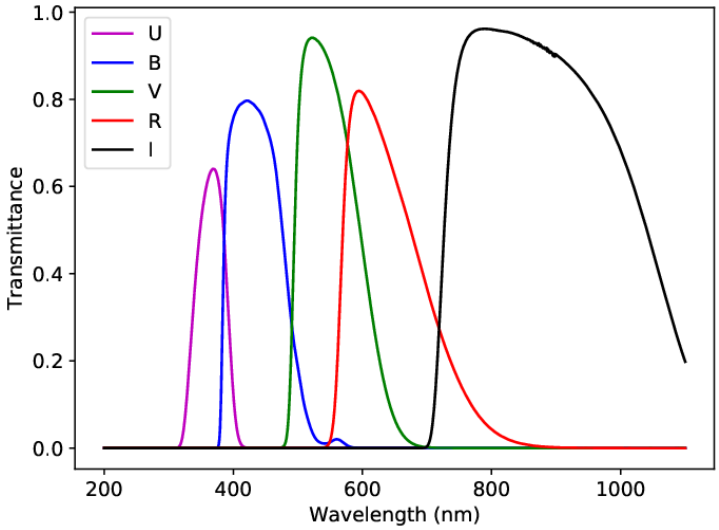

Figure 2.2. Transmission profiles for the Johnson-Cousins filters.

trum of comets due to the most abundant chemical species in comae, and on the other hand, to the emission-free continuum regions characterizing the sunlight reflected by dust grains. Figure 2.3 displays the transmission profiles of the filters. The narrow bands that can be isolated are the emission bands of OH, NH, CN, C_3, CO^+, C_2, and H_2O^+, as well as the UC (ultraviolet), BC (blue), GC (green), and RC (red) dust continuum regions. Detailed characteristics about the filters are given in Table 2.1. Again, it is worth mentioning that the data used for this work did not include any images obtained with the CO^+ and H_2O^+ ion gas filters and with the UC dust filter.

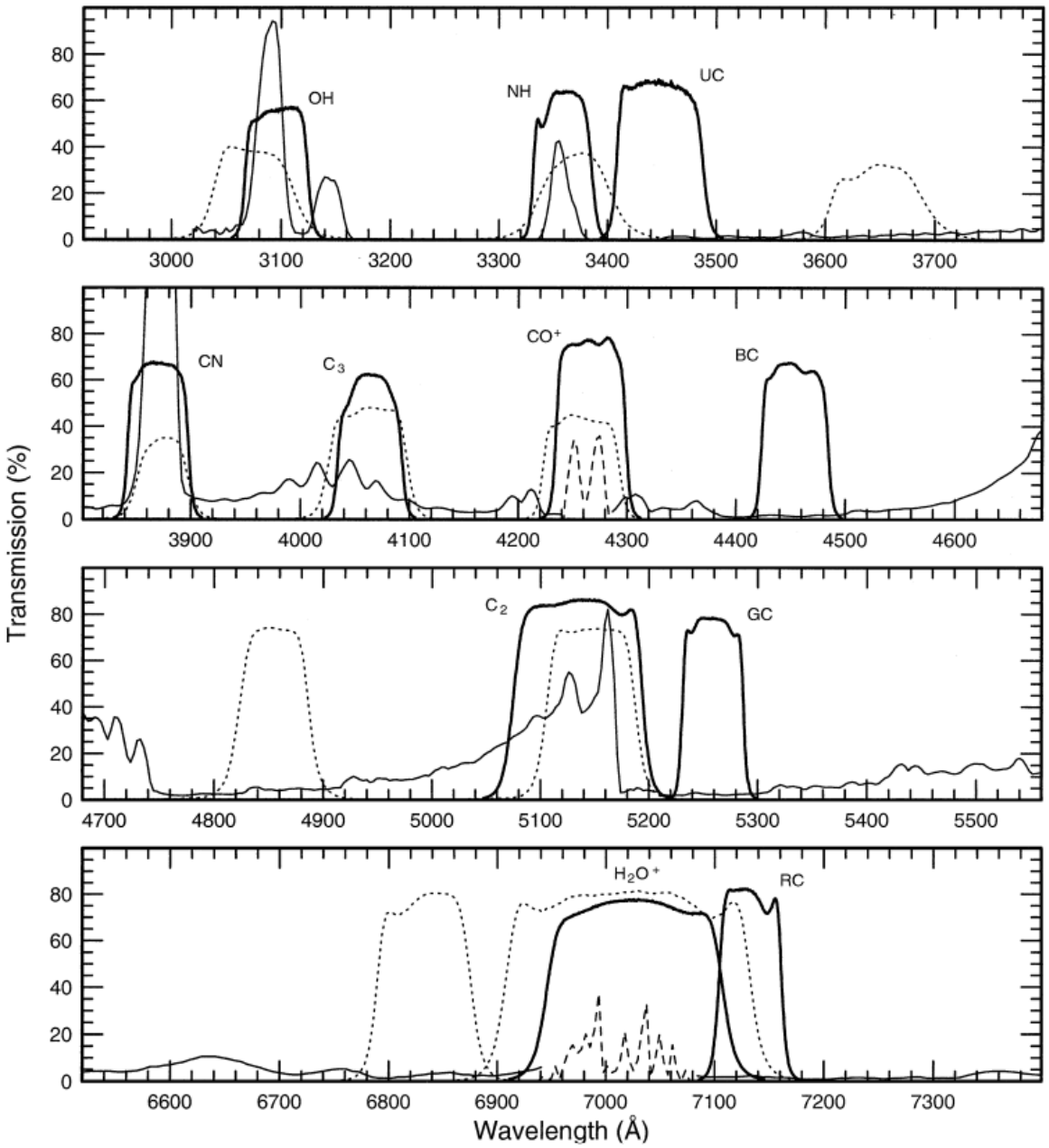

Figure 2.3. Transmission profiles for the narrow-band HB filters (thick solid lines). This figure is from Farnham et al. (2000). The thin solid lines illustrate the different cometary emission bands measured on several comets (122P/de Vico, 8P/Tuttle, 29P/Schwassmann-Wachmann 1, and Kohoutek 1973 E1). Note that the dotted lines show the transmission profiles of the previous generation of narrow-band filters used, known as the International Halley Watch (IHW) filter set.

Table 2.1. Characteristics of the narrow-band HB filters.

Filter ID	Species	λ_{central} (nm)	FWHM (nm) [a]	Transmission (%)
OH	OH(0-0)	309.5	5.65	58.4
NH	NH(0-0)	336.3	5.18	61.8
UC	UV Continuum	344.2	8.35	66.4
CN	CN($\Delta\nu = 0$)	387.1	5.84	66.3
C3	C_3	405.6	5.69	63.7
CO	CO^+(2-0)	426.2	5.70	73.6
BC	Blue Continuum	444.9	5.98	58.4
C2	$C_2(\Delta\nu = 0)$	513.5	11.7	85.0
GC	Green Continuum	525.7	5.65	78.7
H2O	H_2O^+(0,6,0)	701.6	15.7	75.0
RC	Red Continuum	713.0	6.30	80.5

[a] Full Width at Half Maximum. This quantity corresponds to the band pass width (in nm) that would be observed if the profile of the filter was gaussian.

2.2 Observation targets

The aim of this work was to analyze the changes in the activity and composition of periodic comets between two passages at perihelion. For this purpose, two comets that have already passed two times near the Sun since the start of the TRAPPIST project have been selected for the study. This section provides a short description of the targets and their orbital properties. Both of them have been observed over several months before and after the perihelion. Large data sets were thus available, and we were able to follow the evolution of their activity and chemical composition as a function of their heliocentric distance.

2.2.1 Comet 67P/Churyumov-Gerasimenko

67P/Churyumov-Gerasimenko (hereafter called 67P) is a famous comet of the Solar System since it has been thoroughly observed for more than two years by the European Space Agency's Rosetta mission (Snodgrass et al., 2017). In terms of shape, the nucleus of 67P has a bi-lobe appearance, as can be seen in Figure 2.4, taken by a camera on board the Rosetta spacecraft.

Before its discovery, this comet was traveling on an orbit whose closest distance from the Sun was 2.7 AU. At such a distance, the nucleus was not heated enough to lead to the formation of an observable coma. However, its orbit was significantly modified due to a close encounter with Jupiter (closest distance of 0.05 AU) which occurred in February 1959. The perihelion distance then dropped to 1.3 AU, which triggered the comet's activity. Consequently, the planetesimal was discovered by accident ten years later (during the comet's second perihelion passage after the 1959 event), by the astronomers Klim Churyumov and Svetlana Gerasimenko, who were actually studying

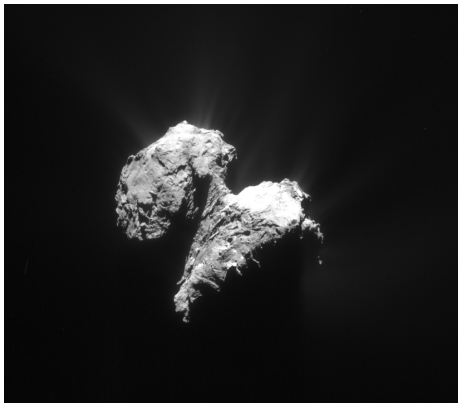

Figure 2.4. Nucleus of Comet 67P/Churyumov-Gerasimenko in activity. The image was taken by the navigation camera (NavCam) aboard ESA's Rosetta spacecraft on 19 August 2014 (`https://imagearchives.esac.esa.int/`). The nucleus is about 4.3 km in length.

another comet (32P/Comas-Solá) (Lamy et al., 2007). The calculation of its orbit then revealed a revolution period around the Sun of a bit more than 6.5 years, thus classifying it in the short-period comet category. Moreover, with a Tisserand parameter of 2.75 with respect to Jupiter, 67P belongs to the JFCs.

67P was observed with TRAPPIST during its last two passages near the Sun, that is in 2015 and 2021. For each passage, observations have been performed over several months before and after the perihelion, while the comet was evolving on its orbit. However, between the two observation periods, the comet's orbit has slightly changed because of the gravitational influence of Jupiter and non-gravitational forces (i.e., momentum transferred to the nucleus by the gas and dust escaping the comet). The main orbital parameters of the comet, as well as the Earth-comet distance at perihelion, are given in Table 2.2 for both the first and the second observed passages.

The first perihelion passage occurred on August 13, 2015. The observations of the comet were conducted with TS (TN was not installed yet at that time) over a total of 79 nights spread between April 2015 (heliocentric distance: $r_h = 1.8$ AU) and July 2016 ($r_h = 3.4$ AU). The upper part of Figure 2.5 gives the number of images collected with the different filters during each observation nights. As it can be seen, mainly the broad-band filters have been used for the observations, while very few images have been collected with the HB filters. In the lower part of the figure, the blue, purple, and red curves show respectively the evolution of the heliocentric and geocentric distances of the comet and the phase angle (i.e., the Sun-comet-Earth angle) during the observation period. The second passage was recorded simultaneously with both TS and TN. The comet passed at perihelion on November 2, 2021. The observations were performed from May 2021 ($r_h = 2.3$ AU) to February 2022 ($r_h = 1.8$ AU), during 67 nights in total. The number of collected images, as well as the evolution of the heliocentric distance, the geocentric distance, and the phase angle of the comet

Table 2.2. Main orbital parameters of comet 67P at the time of its perihelion passages in 2015 and 2021.

Parameter	Value in 2015	Value in 2021
Orbital period P^{a}	6.44 yr	6.42 yr
Perihelion distance q^{a}	1.24 AU	1.21 AU
Semi-major axis a^{a}	3.46 AU	3.46 AU
Eccentricity e^{a}	0.64	0.65
Inclination w.r.t. the ecliptic plane i^{a}	7.04°	3.78°
Longitude of ascending node Ω^{a}	50.14°	36.33°
Argument of perihelion ω^{a}	12.80°	22.14°
Distance to the Earth at perihelion[b]	1.77 AU	0.42 AU

[a] Values taken from Seiichi Yoshida's website (`http://aerith.net/`).
[b] Values obtained with the Horizons System on NASA's Jet Propulsion Laboratory website (`https://ssd.jpl.nasa.gov/horizons/`).

over this ten-month observation period, are shown in Figure 2.6.

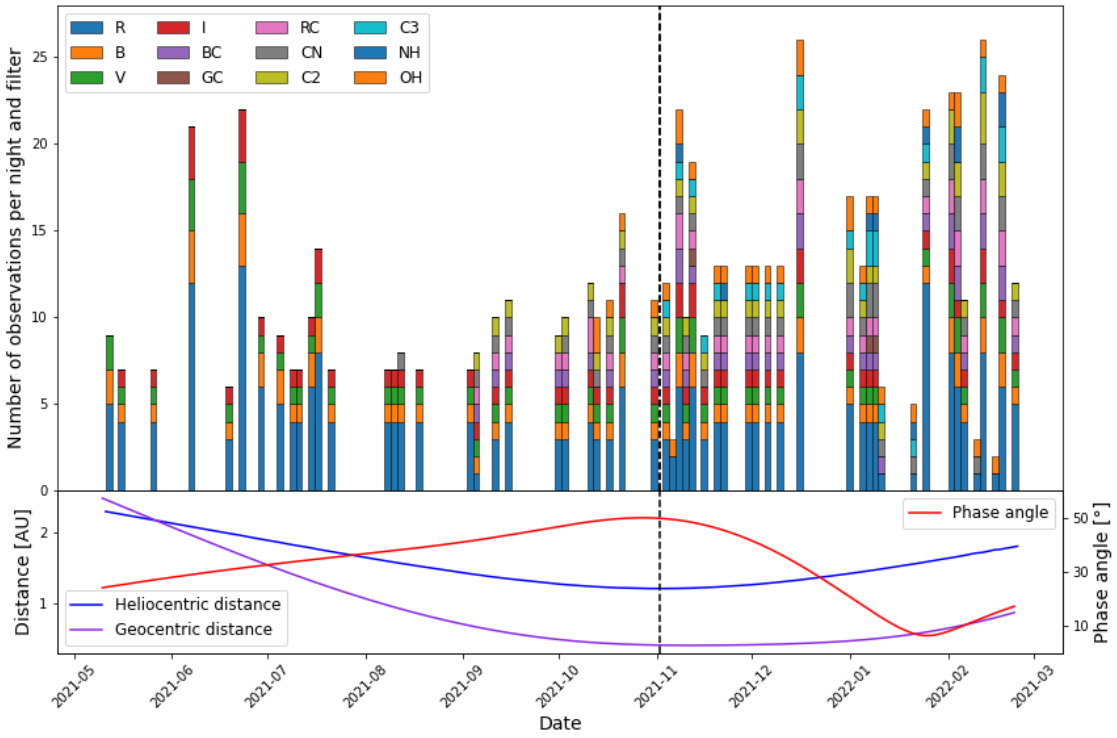

Figure 2.6. Upper part: representation of the number of observations performed with the different broad-band and narrow-band filters during each observation nights, for the 2021 perihelion passage of comet 67P. Lower part: evolution of the heliocentric distance, geocentric distance and phase angle of the comet over the observation period. These parameters were computed by NASA's JPL Horizons System (`https://ssd.jpl.nasa.gov/horizons.cgi`). The dashed, black line gives the perihelion date, i.e., November 2, 2021.

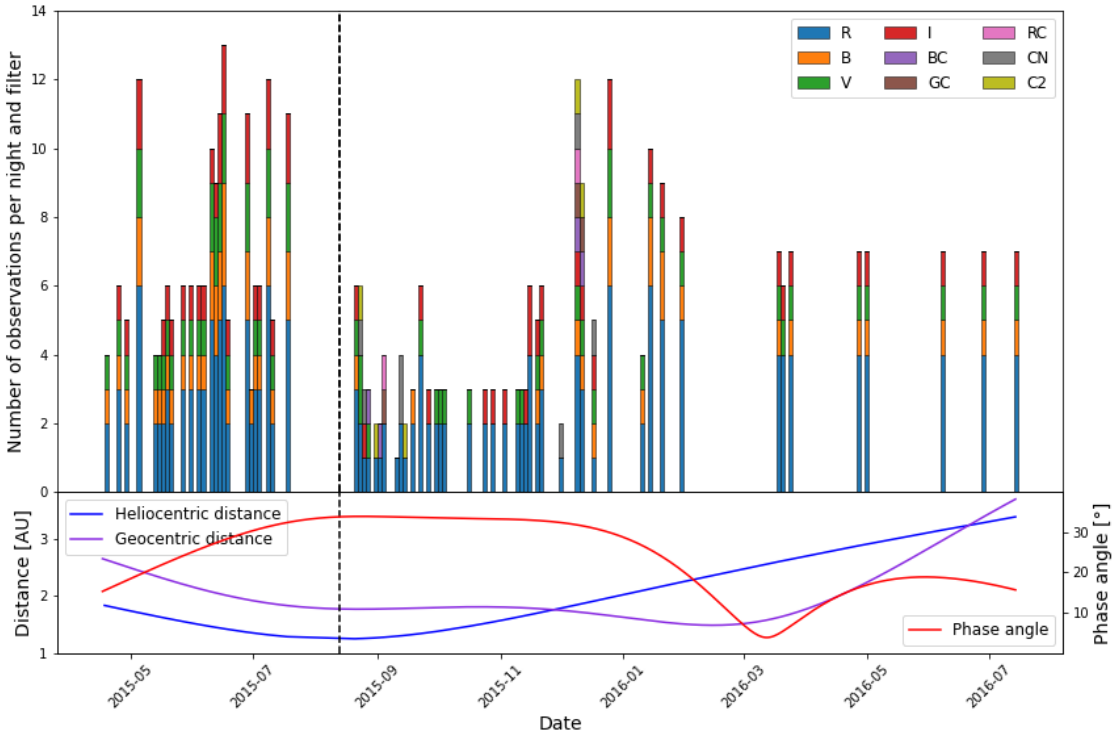

Figure 2.5. Upper part: representation of the number of observations performed with the different broad-band and narrow-band filters during each observation nights, for the 2015 perihelion passage of comet 67P. Lower part: evolution of the heliocentric distance, geocentric distance and phase angle of the comet over the observation period. These parameters were computed by NASA's JPL Horizons System (`https://ssd.jpl.nasa.gov/horizons.cgi`). The dashed, black line gives the perihelion date, i.e., August 13, 2015.

2.2.2 Comet 103P/Hartley 2

Comet 103P/Hartley 2 (hereafter called 103P) was discovered in March 1986 by the British astronomer Malcolm Hartley, who was working with the Schmidt Telescope at the Siding Spring Observatory in Australia. In 2005, for the Deep Impact mission, NASA sent a spacecraft toward Comet 9P/Tempel 1 to observe it and realize a large number of measurements, including a collision with the comet. When the Deep Impact objectives were reached, the spacecraft still had plenty of propellant and was therefore recycled for a second mission called EPOXI (Extrasolar Planet Observation and Deep Impact Extended Investigation). One of the goals of this extended mission was to visit another comet, and 103P became the new target to reach. In November 2010, the spacecraft thus realized a flyby of 103P and approached it at the closest distance of about 694 kilometers. The study of 103P by the EPOXI spacecraft lasted for three weeks and allowed to obtain a lot of images of the comet. As it can be seen in Figure 2.7, taken during the EPOXI mission, the nucleus of 103P has also a bi-lobe shape.

Figure 2.7. Nucleus of Comet 103P/Hartley 2 in activity. The image was taken by the Medium Resolution Instrument (MRI) aboard NASA's EPOXI spacecraft on 4 November 2010 (`https://photojournal.jpl.nasa.gov/mission/EPOXI`). The nucleus is about 2.3 km in length.

Similarly to 67P, 103P is a short-period comet and belongs to the class of JFCs ($T_J = 2.64$). Its last three passages close to the Sun occurred in 2010, 2017, and 2023. However, only the 2010 and 2023 perihelion passages were observed with TRAPPIST, since the position of the comet during its passage in 2017 did not allow any observation from the surface of the Earth. The changes in the orbital parameters of the comet between the two observed passages due to non-gravitational forces and Jupiter's gravitational attraction are given in Table 2.3, although these changes are not as significant as those observed for 67P.

Table 2.3. Main orbital parameters of comet 103P at the time of its perihelion passages in 2010 and 2023.

Parameter	Value in 2010	Value in 2023
Orbital period P[a]	6.47 yr	6.48 yr
Perihelion distance q[a]	1.06 AU	1.06 AU
Semi-major axis a[a]	3.47 AU	3.48 AU
Eccentricity e[a]	0.70	0.69
Inclination w.r.t. the ecliptic plane i[a]	13.62°	13.61°
Longitude of ascending node Ω[a]	219.76°	219.75°
Argument of perihelion ω[a]	181.20°	181.30°
Distance to the Earth at perihelion[b]	0.14 AU	0.41 AU

[a] Values taken from Seiichi Yoshida's website (`http://aerith.net/`).
[b] Values obtained with the Horizons System on NASA's Jet Propulsion Laboratory website (`https://ssd.jpl.nasa.gov/horizons/`).

The first perihelion passage of 103P occurred on October 28, 2010. The comet was observed with TS from December 2010 (heliocentric distance: $r_h = 1.2$ AU), so about a month and a half after the perihelion, to May 2011 ($r_h = 2.5$ AU), during a total of 64 nights. The number of images acquired with the different filters is given in Figure 2.8. For this passage, the data collection has

been highly intensive, with tens of images collected during each observation night, especially with the gas filters. The variations of the heliocentric and geocentric distances of the comet and the phase angle are represented as a function of time over the observation period in the lower part of the figure. The second perihelion passage occurred on October 12, 2023. The observations started several months before that date, in June 2023 (r_h = 1.8 AU), and ended in March 2024 (r_h = 2.1 AU). Data have been collected over 68 nights spread between these two dates. The number of images obtained is given in Figure 2.9, along with the evolution of the geometric configuration between the Sun, the Earth, and the comet during the observation period.

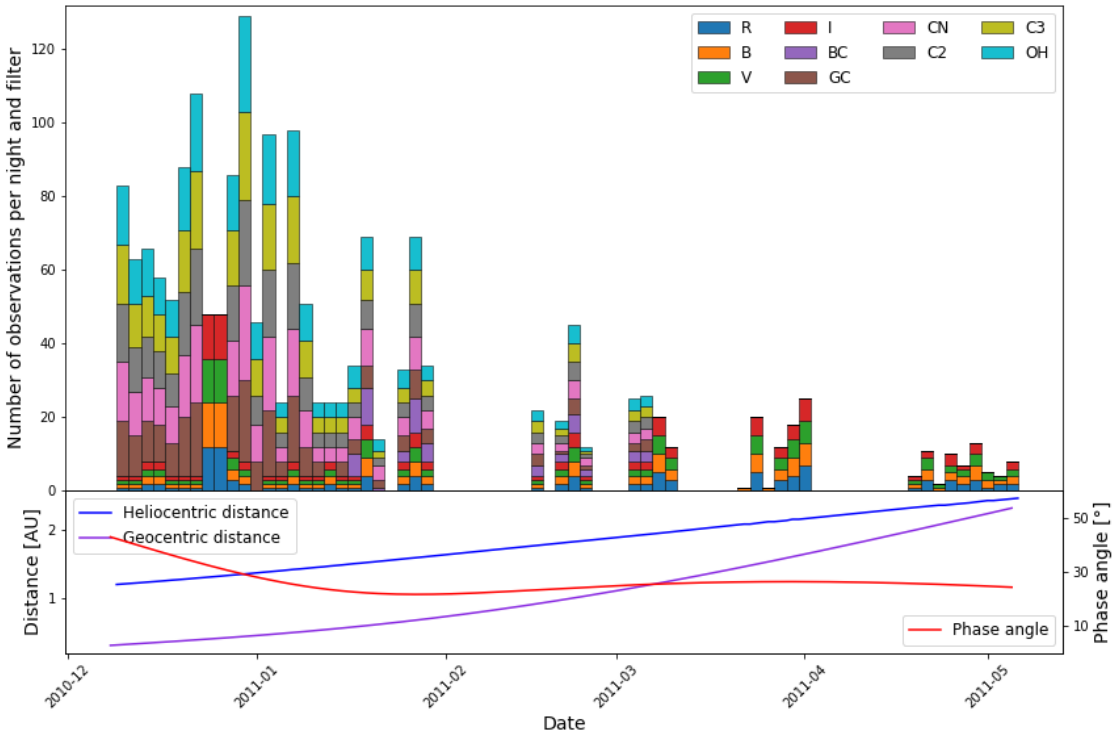

Figure 2.8. Upper part: representation of the number of observations performed with the different broad-band and narrow-band filters during each observation nights, for the 2010 perihelion passage of comet 103P. Lower part: evolution of the heliocentric distance, geocentric distance and phase angle of the comet over the observation period. These parameters were computed by NASA's JPL Horizons System (`https://ssd.jpl.nasa.gov/horizons.cgi`)

.

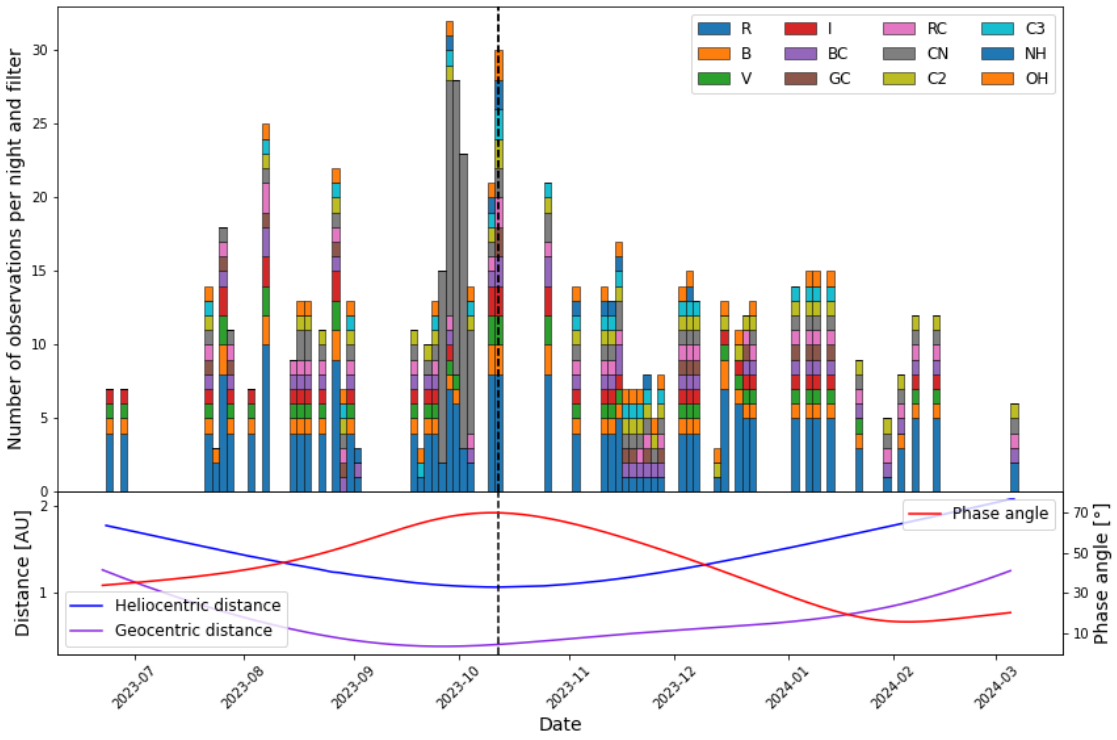

Figure 2.9. Upper part: representation of the number of observations performed with the different broad-band and narrow-band filters during each observation nights, for the 2023 perihelion passage of comet 103P. Lower part: evolution of the heliocentric distance, geocentric distance and phase angle of the comet over the observation period. These parameters were computed by NASA's JPL Horizons System (`https://ssd.jpl.nasa.gov/horizons.cgi`). The dashed, black line gives the perihelion date, i.e., October 12, 2023.

Chapter 3

Data reduction and photometry

The observation methods and targets of this study have been presented. A great number of images of the two comets have been collected over several months. However, before being used for the computation of parameters such as the cometary gas production rates and dust activity, the comet images had to be corrected for several effects, both from instrumental and natural origins. Once the corrections were applied to the images, radial brightness profiles of the comets were computed numerically. Then, the measured flux was converted into a physical unit, and finally, we were able to plot magnitude curves for each comet and each perihelion passage.

This chapter describes the methods used in this work for image reduction and briefly explains how the radial brightness profiles are computed. Then, the formula used for the conversion of flux values is given and explained in detail. Finally, both for 67P and 103P, we present the light curves obtained for the two perihelion passages and compare them together to spot the differences in magnitude from one passage to another.

3.1 Reduction of TRAPPIST data

The reduction of the comet images aimed at removing the instrumental effects through a calibration process in order to increase the signal-to-noise ratio of the data. For this work, it was realized notably using Python codes in addition to the Image Reduction and Analysis Facility (IRAF). IRAF is a software system used for the reduction and analysis of astronomical data. It was developed by astronomers and programmers from the National Optical Astronomy Observatory (NOAO) in the United States. It allows the automation of the image reduction process and was thus very useful in our case, given the very large amount of images used for this work.

3.1.1 Image calibration

The first part of the reduction consists of a correction of the comet images for three different kinds of defects caused by the telescope instruments. This correction is realized by using calibration frames (i.e., images taken in specific conditions):

- Bias frames are used to correct the images from the bias effect. Due to read-out noise producing small flux fluctuations, each pixel has a slightly different base level. Consequently, a constant value is added to each pixel value in order to avoid some of them being negative. The bias corresponds to this constant value and needs then to be subtracted from the images. Bias frames are collected with the camera shutter closed and an exposure time of zero seconds.

- Dark frames are used to correct the images from the electronic noise produced because of the sensor heat that can cause dark current (i.e., production of thermal electrons instead of photo-electrons). This effect mainly depends on the temperature of the camera and the exposure time. Dark frames are thus taken with the shutter closed, at the same temperature, and with the same exposure time as the images of interest.

- Flat frames are used to remove the artifacts produced on images because of the optical system. This can be due to vignetting (i.e., darkening of the image corners with respect to the center) or to some dust located in the optical path, for instance. This results in a non-homogeneity in the image brightness. Flat frames are blank images of a uniform light source, on which the brightness variations due to the optics can be seen. Astronomical images are divided by these flat frames, so that all the pixels give the same flux value when exposed to the same amount of light.

Figure 3.1 shows an example of a bias, dark, and flat frames taken with TS. Bias, dark, and flat frames are recorded every day with TRAPPIST. Then, the calibration images obtained over several days are combined, and by taking their median, we create respectively a master bias, a master dark, and a master flat. This notably allows to reduce the noise due to data reduction, and in the case of the master flat, to get rid of the changes that could appear from one frame to another due to the deposition of new dust grains. Finally, we subtracted the master bias and the master dark frames from the raw comet images, and then we divided by the master flat frame to obtain reduced images, as illustrated by the following equation:

$$\boldsymbol{reduced\ image} = \frac{\boldsymbol{raw\ image} - master\ bias - master\ dark}{master\ flat}$$

As an example, a raw image (before calibration) of 67P collected with the R-filter is shown in Figure 3.2, as well as the corresponding reduced image (after calibration) obtained by using master calibration frames that notably include the calibration images shown in Figure 3.1.

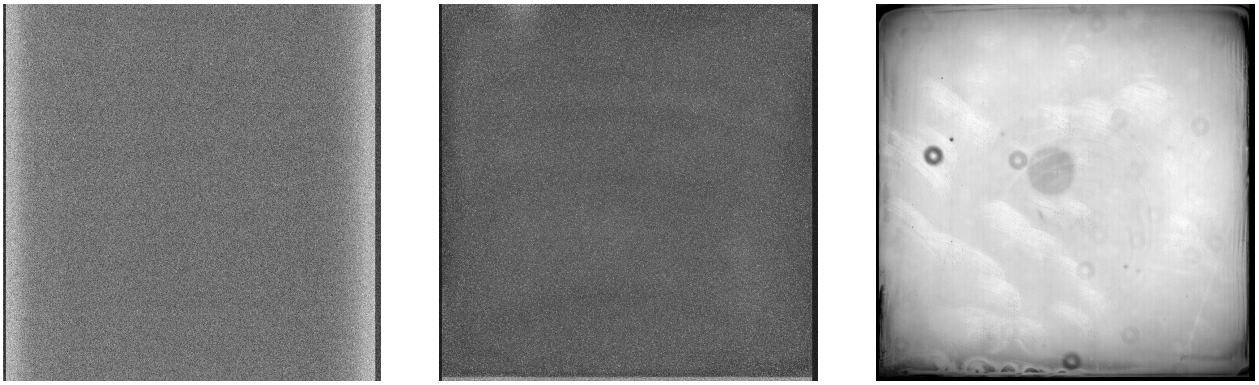

(a) Bias **(b)** Dark **(c)** Flat

Figure 3.1. Bias, dark (obtained with an exposure time of 60 seconds), and flat (obtained with the R-filter) frames obtained with TS and used for the calibration of a R-image of comet 67P collected on November 19, 2021.

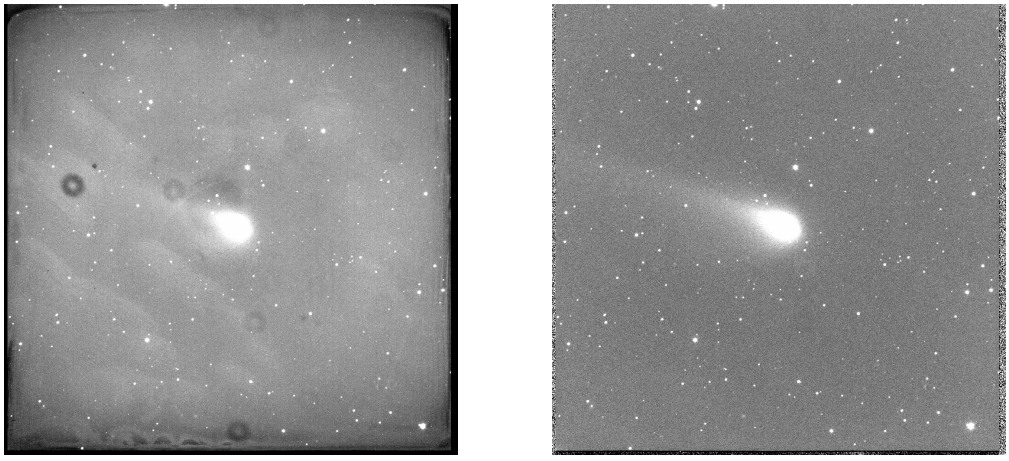

Figure 3.2. R-images of comet 67P obtained on November 19, 2021, before (left) and after (right) the calibration.

3.1.2 Removal of the sky contribution

After the reduction, another correction had to be applied to the images. Indeed, the light coming from the background sky contributes to the measured flux and thus had to be removed. This light can have different origins such as the reflection of solar light by the Moon, atmospheric activity, or light pollution emitted from the surface of the Earth.

To remove this contribution, it is necessary to find an area within the comet images that is, on one hand, far enough from the center of the comet, so that the flux measured is free from any cometary contribution. On the other hand, this area should not be too far from the comet center because, for a correct estimation of the flux to remove, the background sky in the chosen area has to be the same as in the area where the comet is located. This area has thus to be carefully

selected, especially because comets are extended objects, and so it can be difficult to estimate the limit between a region on an image that is contaminated by cometary light, and a region that is not. This was, however, possible in our case, since the field of view of the TRAPPIST telescopes is quite large (22 × 22 arcmin).

In practice, the estimation and removal of the sky contribution was done numerically. On each image, the coordinates of the optocenter (i.e., the brightest point of the coma) were determined by using the IRAF *imcntr* method. After a verification of the obtained coordinates (and a manual correction if necessary), the code searched for the closest region from the center in which the flux did not contain any contribution due to the coma or the background stars. Finally, the median flux of the selected region was measured and subtracted from the whole image. Moreover, the standard deviation of the flux values measured in the different pixels of the region was used in order to estimate the uncertainty on the computed sky background flux (see Section **??**).

3.2 Computation of the radial brightness profiles

Once a comet image has been corrected for the instrumental noise and sky contribution, a radial brightness profile is extracted. This profile is computed by taking successive one-pixel-wide circles, from the optocenter to the edge of the image. For each circle, the median flux of all the constituting pixels is calculated, so that at each unit of nucleocentric distance (in pixels) corresponds a median value of the cometary flux. Finally, a profile is established, representing the evolution of the flux (expressed in ADU s^{-1}) in a given filter as a function of the distance to the optocenter. It is worth mentioning that it is also possible to compute average brightness profiles, instead of median brightness profiles. However, computing median fluxes allows to avoid outliers (mainly high flux values due to cosmic rays) to contribute significantly to the shape of the profiles.

As an example, Figures 3.3, 3.4, and 3.5 show the radial brightness profiles of 67P obtained respectively with the broad-band filters, the narrow-band dust filters, and the narrow-band gas filters, during the night of January 24, 2022. Note that the red, grey, and blue dotted lines on these profiles show the boundaries used for the computation of the magnitude and the cometary gas and dust production rates (see below).

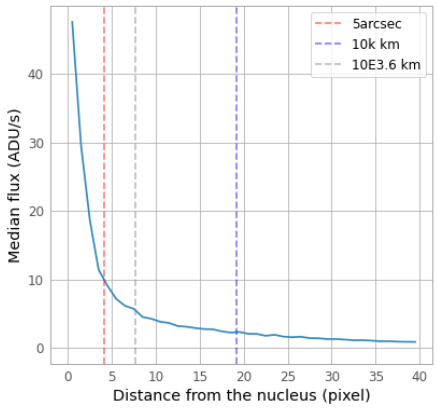

(a) B filter

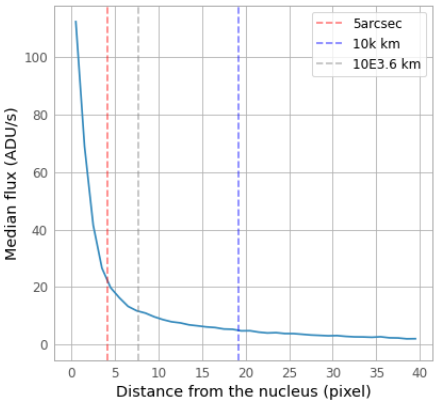

(b) V filter

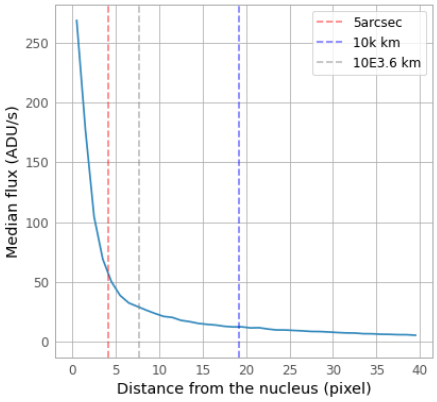

(c) R filter

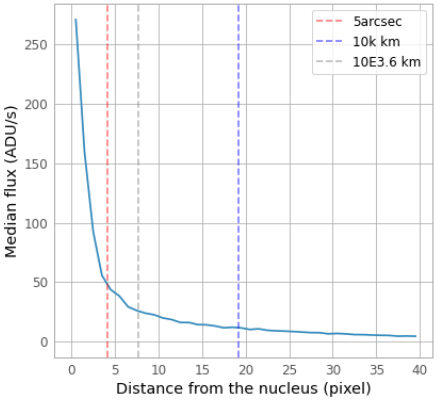

(d) I filter

Figure 3.3. Radial brightness profiles of comet 67P obtained with the broad-band filters (B, V, R, I) on January 24, 2022.

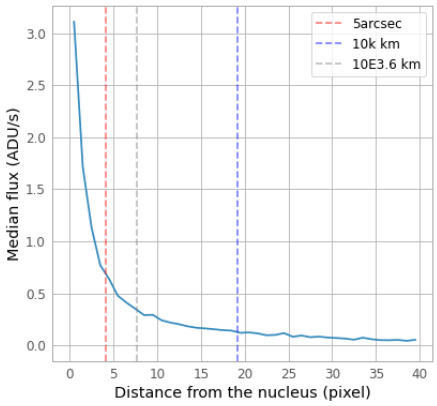

(a) BC filter

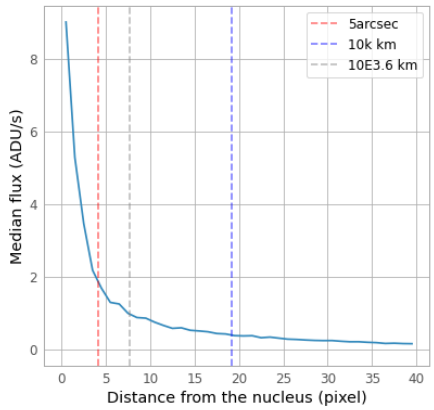

(b) RC filter

Figure 3.4. Radial brightness profiles of comet 67P obtained with the narrow-band dust filters (BC, RC) on January 24, 2022.

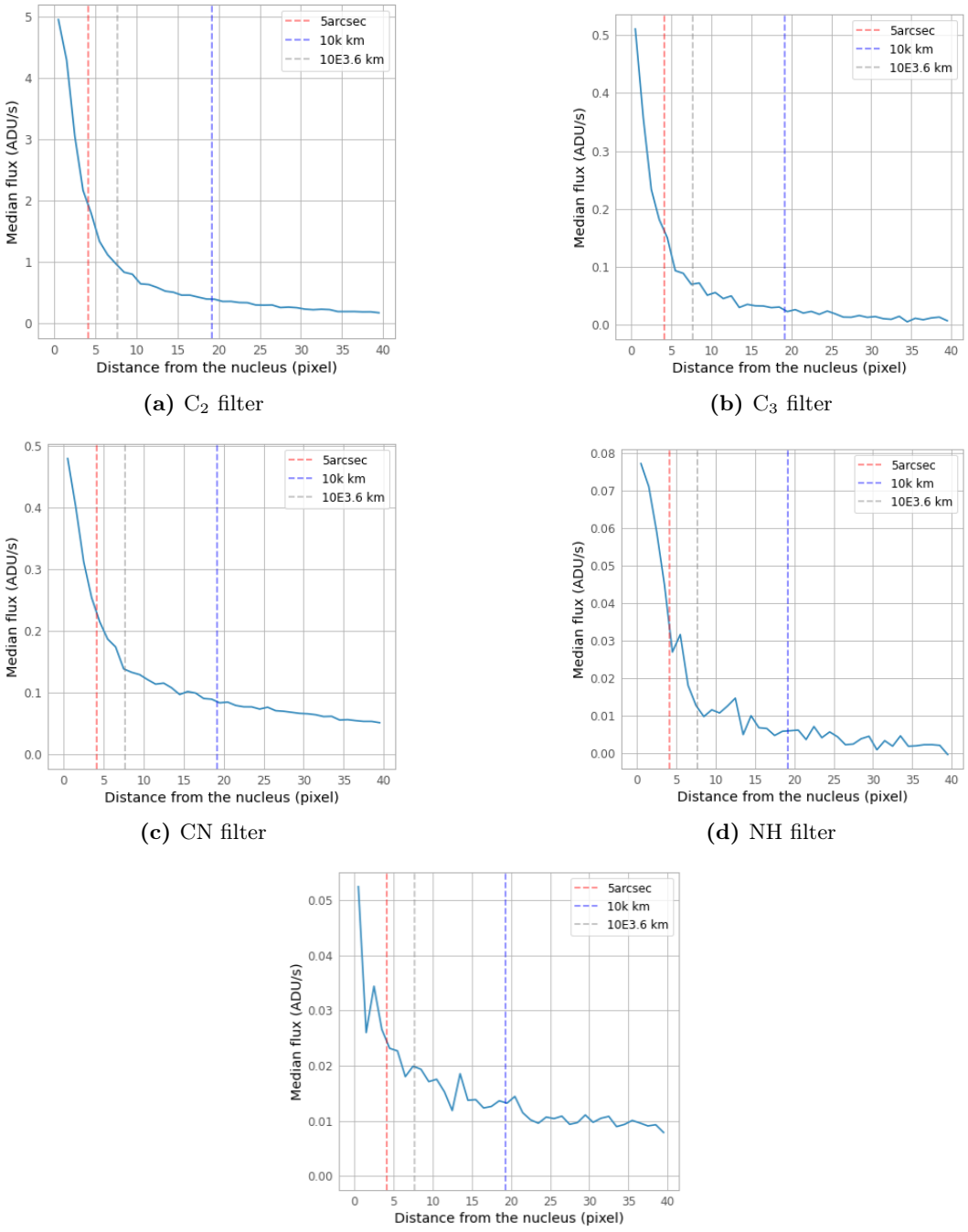

(a) C_2 filter

(b) C_3 filter

(c) CN filter

(d) NH filter

(e) OH filter

Figure 3.5. Radial brightness profiles of comet 67P obtained with narrow-band gas filters (C_2, C_3, CN, NH, OH) on January 24, 2022.

In the BVRI and dust profiles, we can see that, although the exact curve shape slightly changes depending on the filter used, they all show a sharp decrease in the median flux of the coma within a 5-arcsecond distance, followed by a slower decrease. The flux finally reaches a value close to zero

at very large distances from the nucleus. At the contrary, in the gas radial profiles, we observe a significant variation in shape from one curve to another. This is because the measured fluxes are contaminated by the solar light reflected by cometary dust grains. This is especially the case for C_2 and C_3 images, although the OH, NH, and CN images are also slightly contaminated. For that reason, a last correction had to be applied on the radial profiles obtained with the gas filters.

In order to estimate the dust contamination in gas filters, dust filters are used since the light fluxes collected with the latter basically consist of solar light reflected by the dust. In particular, we chose to use BC images, because the flux in the blue continuum is not itself contaminated by gas emissions. RC images could be used as well, but the RC filter's bandpass is further away from the other filters' bandpass (see Figure 2.3). So, the dust contribution estimation would be less reliable. In practice, for each observation night for which images have been collected with the gas filters, the BC image obtained during the same night was used for the correction. A radial profile of the BC flux was computed and then scaled with a factor f_c that depends on the importance of the dust contamination in each gas filter. The f_c values for each filter are given in Table 3.1. Finally, the scaled dust profile was subtracted from the corresponding gas radial profiles. Please note that, for some nights, data have been collected with the gas filters but not with the BC filter. In this case, we used the BC radial profile obtained the most recently for the correction.

Table 3.1. Values of the scaling factor f_c for the different gas filters.

Filter	f_c
OH	19
NH	24
CN	30
C_2	170
C_3	248

3.3 Flux calibration of the radial profiles

To be able to calculate some quantities such as the cometary gas production rates and dust activity based on the measured cometary flux, it was necessary to convert the pixel values to express them in a physics unit. For the conversion of cometary flux units from ADU arcsec^{-2} s^{-1} to erg cm^{-2} s^{-1} Å^{-1}, we used a formula developed by Farnham et al. (2000). The latter realized observations of standard stars with the HB cometary filters. The flux of these stars in erg cm^{-2} s^{-1} Å^{-1} was already known, and the flux in ADU arcsec^{-2} s^{-1} was measured through the observations, allowing the authors to establish a relationship between the two quantities. In this way, they obtained

a conversion formula, which is given by:

$$F_c = F_0 \times F \times 10^{0.4\ (K\ \times\ am\ -\ 25\ +\ ZP)}, \tag{3.1}$$

where F_c is the cometary flux (measured with a given filter) in erg cm^{-2} s^{-1} Å^{-1}, F_0 is the flux of a zero-magnitude star (in erg cm^{-2} s^{-1}) that would be observed with the same filter, and F is the cometary flux in ADU arcsec^{-2} s^{-1}.

The remaining quantities in the equation allow us to account for the wavelength-dependent extinction of the cometary flux when the light passes through the atmosphere. K is the extinction coefficient of the atmosphere for a given filter. Its value changes as a function of the place where the observations are performed, time, and meteorological conditions. However, by simplicity, we always use the same values and consider a 5%-uncertainty on them. ZP is the zero point of the filter, i.e., a reference value corresponding to the flux of a theoretical star of magnitude zero that would be measured with the considered filter. Its value changes from one night to another, and in general, a median value computed over a month is used. Table 3.2 gathers the F_0 values and the extinction coefficients for the different filters. As an example, the median values of the zero points measured during July 2012 are also given.

Table 3.2. Filter parameters used for the flux calibration of the radial brightness profiles.

Filter	F_0 [10^{-9} erg cm^{-2} s^{-1} Å^{-1}][a]	K	ZP[b]
OH	10.560	1.60	6.493
NH	8.420	0.65	6.183
CN	8.6	0.36	5.743
C3	8.160	0.29	5.693
C2	3.887	0.15	5.010
BC	6.210	0.25	5.890
GC	3.616	0.14	5.931
RC	1.316	0.05	6.447
B	6.4	0.25	2.452
V	3.76	0.14	2.545
R	1.92	0.098	2.357
I	0.939	0.043	3.039

[a] Values taken from Farnham et al. (2000).
[b] Median value of the zero points measured in July 2012.

Finally, am represents the airmass at the moment of the observations. This quantity gives the thickness of terrestrial atmosphere through which the light passes before reaching the telescope. It thus depends on the position of the comet in the sky during the observations through the approximate relation $am = 1/\cos(z)$ (where z is the zenith angle, i.e., the angle between the position of the comet and the zenith). If the comet is located at the zenith (directly above the telescope), the

thickness of atmosphere crossed by the light is the smallest, and the airmass value is thus the lowest ($am = 1$). As the angle z increases (i.e., the comet approaches the horizon), the airmass value increases because the light has to cross a larger thickness of atmosphere. This effect is illustrated in Figure 3.6. The airmass values of 67P and 103P can be found in the header of each image obtained with TRAPPIST. Since the atmospheric particles can significantly affect the signals by absorbing and scattering photons, it is important to take this parameter into account during the observations. Its value must be as small as possible to ensure accurate data.

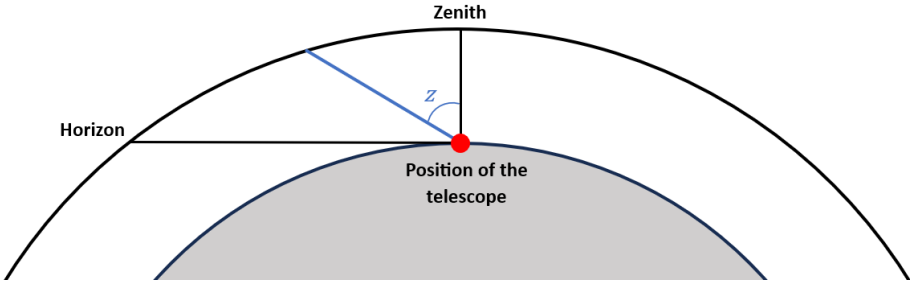

Figure 3.6. Illustration of the airmass. The blue line represents the path followed by the light inside the atmosphere, and z is the zenith angle.

In the process of data reduction and flux calibration, a significant source of uncertainty comes from determining the sky contribution. To estimate the error in the calculated sky background flux, we use a value equal to three times the standard deviation (3σ) of the computed flux. Additionally, the extinction coefficient values add a bit to the uncertainty, especially at high airmass. To account for this, an error of 5% of the coefficient values is used, as already mentioned above. The total uncertainties in the cometary fluxes, and thus in the gas and dust production rates, are then calculated by combining the errors from the sky background flux and the extinction coefficients in quadrature (i.e., using the square root of the sum of the squares of these uncertainties).

3.4 Light curves of the comets

After the conversion of flux units from ADU arcsec^{-2} s^{-1} to erg cm^{-2} s^{-1} Å^{-1}, we computed, for each observation night and each filter, the cometary flux integrated inside a 5-arcsec circular aperture (see the dashed, red line in Figure 3.3). We then plotted the results of our measurements as a function of time and heliocentric distance in order to study the evolution of the magnitude of the comets during their perihelion passages. Please note that, in the plots presented in this section and the following chapters, some data points are missing. They have been removed either because we noticed bad observation conditions (e.g., passage of a cloud in the field of view during the observations) leading to significantly different flux values measured with the R filter, or because

some elements in the images seemed to have an impact on the results (e.g., crowded field of view, star trail behind or close to the comet, etc.).

Comet 67P/Churyumov-Gerasimenko

The light curves obtained for the first and second passages of 67P are shown in Figure 3.7 as a function of time, expressed in Modified Julian Day (MJD = JD − 2400000.5), and heliocentric distance. Please note that negative heliocentric distances stand for the pre-perihelion phase (comet approaching the Sun) and positive distances stand for the post-perihelion phase (comet going away from the Sun).

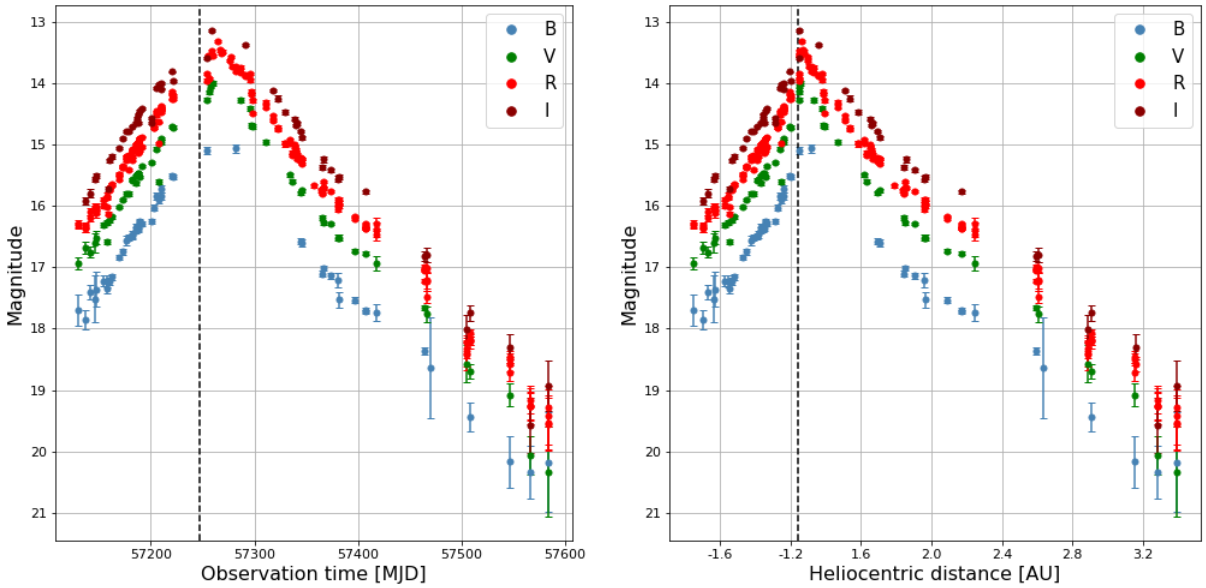

(a) Light curves of 67P during its 2015 passage.

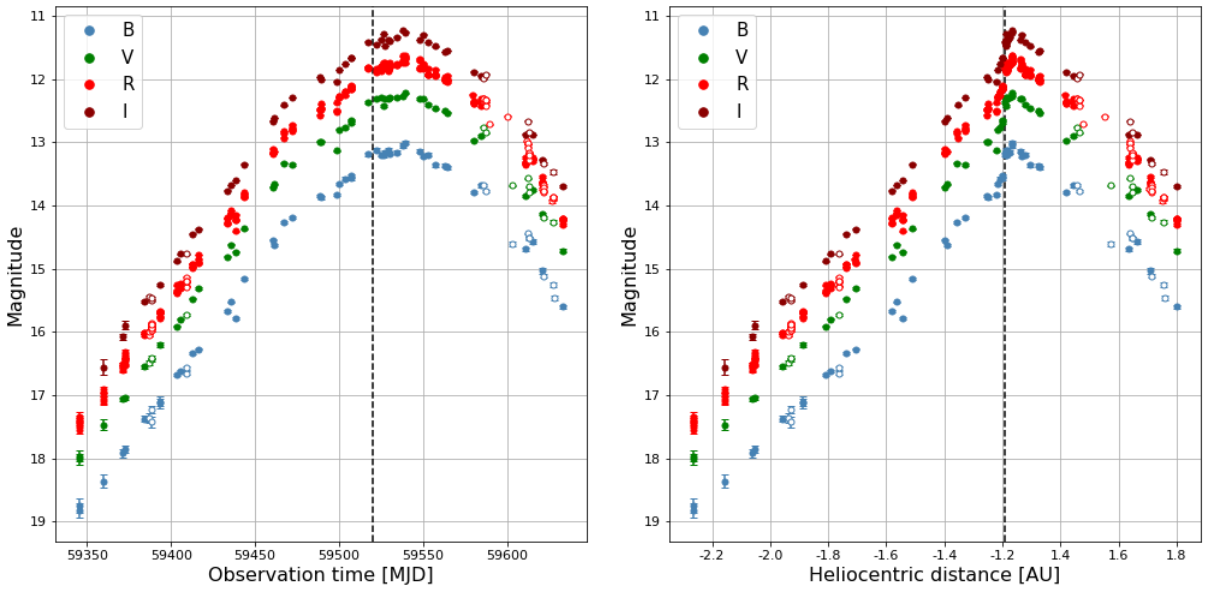

(b) Light curves of 67P during its 2021 passage.

Figure 3.7. Evolution of the magnitude of comet 67P as a function of time (left) and heliocentric distance (right) from April 2015 to July 2016 (upper panels) and from May 2021 to February 2022 (lower panels). The dashed, black line in the left-hand plots represents the perihelion date, i.e., August 13, 2015 (in the upper panel) and November 2, 2021 (in the lower panel). Solid and empty points stand for TS and TN data, respectively. Note that the error bars are shown for all data points, but some are smaller than the point size and thus not visible.

In these curves, we see that the magnitude of 67P increases in the pre-perihelion phase as a result

of the increasing insulation, and decreases in the post-perihelion phase as the comet is moving away from the Sun. We do not observe any outburst (i.e., intense and brief increase in the outgassing). This result is interesting because, during its passage at perihelion in 2015, 67P was accompanied by the Rosetta spacecraft. Orbiting the nucleus, the probe has realized detailed observations of the comet during its whole activity period. It was very close to it and has thus been able to measure several small outbursts (see for example Feldman et al. (2016) and Rinaldi et al. (2018)). However, these outbursts are not visible in our light curves. This indicates that, when observing the coma with ground-based instruments, the global magnitude that we can measure is insensitive to the small changes that actually occur in the coma. Despite the great accuracy reached with the TRAPPIST telescopes, such small outbursts are imperceptible.

Another interesting point observed with these curves is about the position of the maximum brightness of the comet. Indeed, we see that this maximum does not occur at the time of perihelion, as could be expected, but several days later. This causes an asymmetry in the light curves with respect to perihelion. Actually, this result is often observed in comet light curves and can be attributed to several effects. On one hand, let's remember that the shape of cometary nuclei is generally far from the symmetry of a sphere. Their irregular shape and the presence of some more active regions on their surface lead to a so-called "seasonal effect", and this sometimes causes an asymmetry in the light curves. On the other hand, the observed asymmetries can also be linked to the thermal inertia of cometary nuclei. Thermal inertia is a property that describes the ability of a body to accumulate heat and then progressively re-emit it. In the case of comet nuclei, they accumulate heat as they get closer to the Sun, and after their passage at perihelion, they re-emit this heat progressively as the insulation starts decreasing. This effect can be responsible for the fact that the cometary activity is sometimes the highest several days or weeks after perihelion. In particular, for the first passage of 67P, we observe the peak of magnitude on August 30, 2015, i.e., 17 days after perihelion, while for the second passage, we observe it on November 21, 2021, i.e., 19 days after perihelion. Note that this two-day shift observed is probably due to the low accuracy in the determination of the date of maximum brightness, so we consider it negligible. Thus, we detect for both passages the same time interval between the date of perihelion and the date of maximum brightness, although the comet was not oriented exactly the same way with respect to the Sun. This shows that the seasonal effect is effectively an intrinsic characteristic of comets.

The resulting asymmetry in the light curves of 67P is even more visible in Figures 3.8 and 3.9, respectively for the first and second passages. In these plots, the evolution of magnitude is represented as a function of the heliocentric distance of the comet, and the pre-perihelion and post-perihelion data points are shown in different colors. In this way, we can easily see that, at the same heliocentric distances, the post-perihelion apparent magnitude (represented in deeper colors) is definitely lower than the pre-perihelion apparent magnitude (represented in lighter colors), at least for $r_h < 1.8$ AU.

The pre-perihelion and post-perihelion data have been fitted separately with a straight line in order to retrieve the slopes of the different curves. The obtained values are given in Table 3.3 for the two passages of the comet.

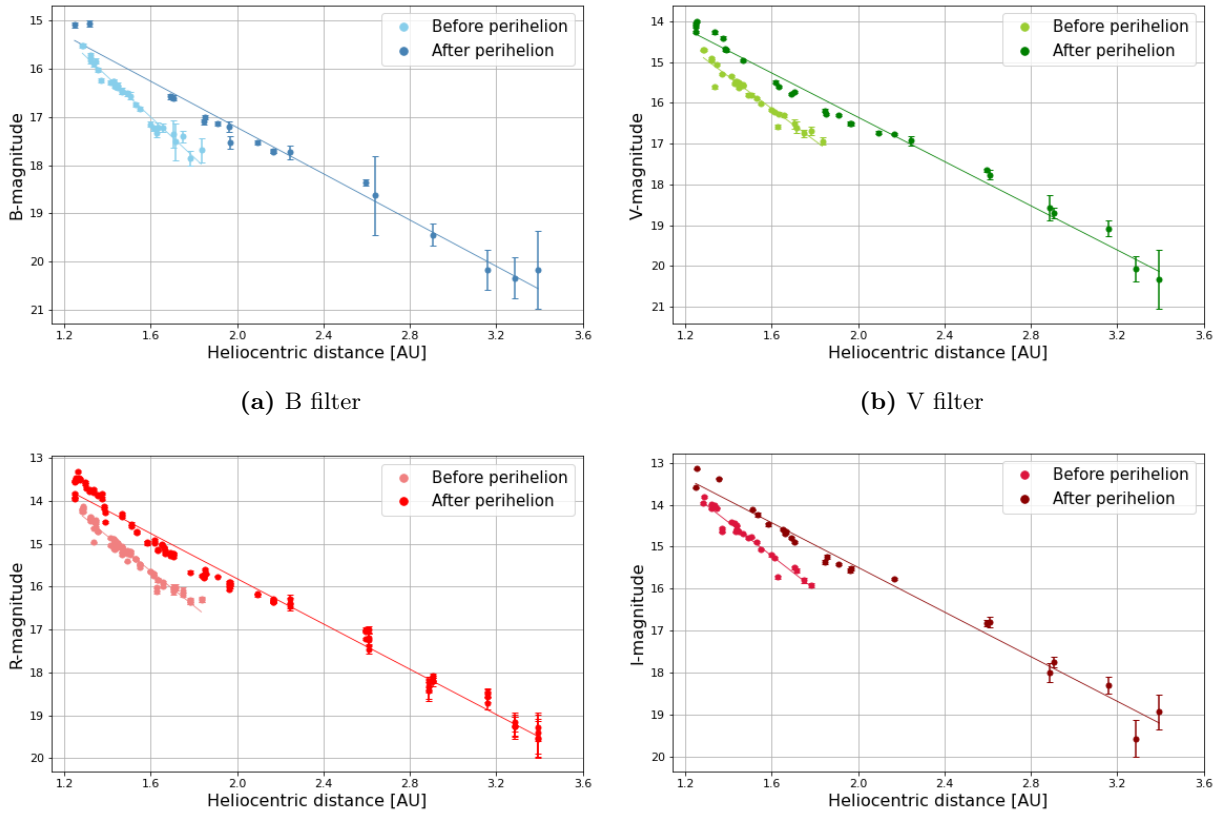

(a) B filter

(b) V filter

(c) R filter

(d) I filter

Figure 3.8. Evolution of the magnitude of comet 67P as a function of the heliocentric distance during its 2015 perihelion passage. Pre-perihelion and post-perihelion data points have been fitted separately with straight lines, represented in respective colors.

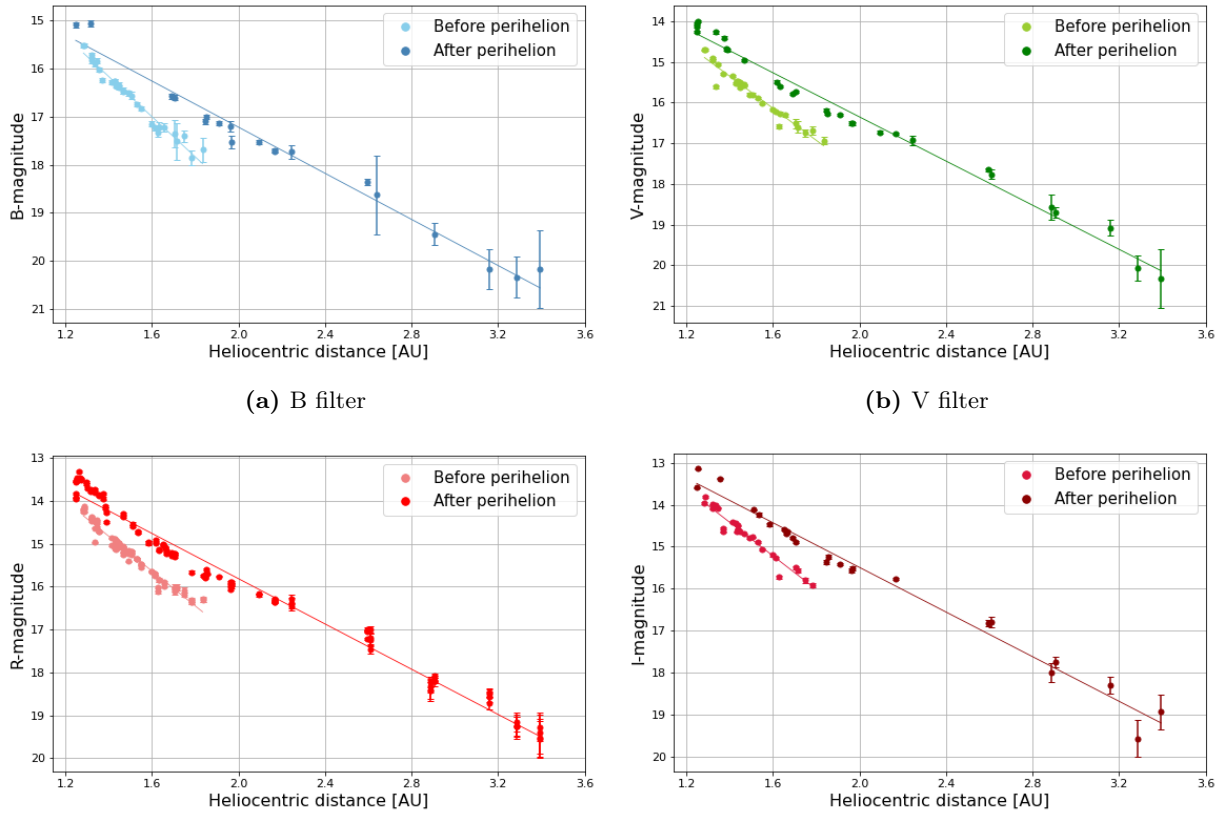

(a) B filter

(b) V filter

(c) R filter

(d) I filter

Figure 3.9. Evolution of the magnitude of comet 67P as a function of the heliocentric distance during its 2021 perihelion passage. Solid and empty points stand for TS and TN data, respectively. Pre-perihelion and post-perihelion data points have been fitted separately with straight lines, represented in respective colors.

Table 3.3. Slopes derived from the linear fit applied on the pre-perihelion and post-perihelion light curves of comet 67P.

		Slopes	
		Pre-perihelion	Post-perihelion
B filter	2015	4.17 ± 0.14	2.39 ± 0.09
	2021	5.04 ± 0.07	3.91 ± 0.15
V filter	2015	3.93 ± 0.17	2.71 ± 0.07
	2021	5.04 ± 0.06	3.74 ± 0.14
R filter	2015	4.06 ± 0.09	2.64 ± 0.04
	2021	5.07 ± 0.03	3.88 ± 0.08
I filter	2015	4.00 ± 0.20	2.66 ± 0.08
	2021	5.12 ± 0.06	3.85 ± 0.14

Afterward, we combined the data collected in 2015 and 2021 in order to study the differences and similarities in the activity of 67P between the two passages. The results are shown in Figure 3.10.

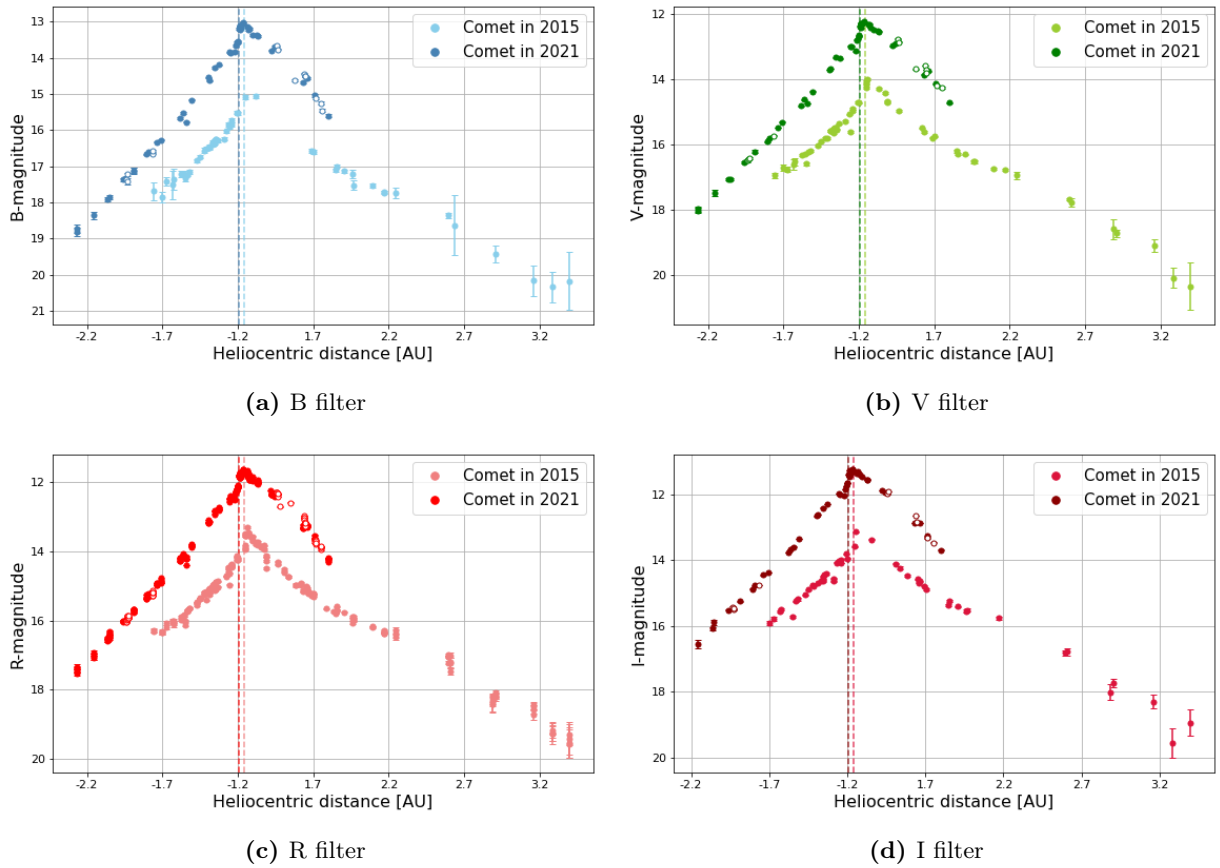

(a) B filter

(b) V filter

(c) R filter

(d) I filter

Figure 3.10. Comparison of the magnitude of comet 67P during the perihelion passages in 2015 and 2021. The dashed lines in deep and light colors represent respectively the heliocentric distances at perihelion for the first (1.24 AU) and second (1.21 AU) passages.

A comparison of the data can only be performed over a range of heliocentric distances going approximately from 1.7 AU before the perihelion to 1.7 AU after the perihelion. By analyzing the two curves within this range, we can see that the magnitude measured in 2021 (represented by the deep-colored data points) is clearly lower than the one measured in 2015 (represented by the light-colored data points). However, let's keep in mind that this does not necessarily indicate a more intense activity. Indeed, the observed apparent magnitude of the comet, as seen from Earth, is not solely dependent on its intrinsic activity but also on the geometry of the comet's orbit relative to the Sun and Earth's positions. Actually, two major geometric effects can sometimes enhance or diminish the observed brightness. First, the phase angle formed by the positions of the Sun, the comet, and the Earth plays a significant role in the apparent magnitude of the comet. Then, the distance between the Earth and the comet during the observations can also affect the measured magnitude. Indeed, the comet looks brighter when it is closer to Earth because the light it reflects has a shorter distance to travel before reaching our instruments, reducing the effects of distance

dimming. As a consequence, the differences in the magnitude of 67P observed between 2015 and 2021 might be due to different geometrical configurations during the two observation periods, rather than different cometary activities.

In order to check whether the apparent magnitude of 67P was lower in 2021 due to more intense intrinsic activity, or simply because of a different geometrical configuration than in 2015, we computed the so-called "heliocentric magnitude" of the comet. Basically, this corresponds to the apparent magnitude without the dependence to the Earth distance. The apparent magnitude of comets is given by the following formula:

$$m = M + 5 \log \Delta + 2.5n \log r_h \tag{3.2}$$

where m and M are respectively the apparent and absolute magnitude, Δ is the geocentric distance, r_h is the heliocentric distance, and n is the power-law exponent. Thus, removing the dependence on the Earth distance simply consists of subtracting the term $5 \log \Delta$ (as if the comet was localized at a geocentric distance $\Delta = 1$ AU) from the measured apparent magnitude. Then, the comet's observed brightness only depends on the heliocentric distance, which is the main driver of cometary activity. For the computation of the heliocentric magnitude, the Δ values were obtained with NASA's JPL Horizons System[1] (see the purple curve in the lower panel of Figures 2.5 and 2.6). After the subtraction, we plotted the apparent magnitude as a function of heliocentric distance, as for the above figures. The obtained results are shown in Figure 3.11.

By comparing Figures 3.10 and 3.11, we see that the position of the comet with respect to the Earth effectively plays an important role in the measured apparent magnitude. The removal of the geocentric-distance dependence seems to cancel the shift that was observed between the 2015 and 2021 curves, except near the perihelion. Indeed, within the heliocentric distance range from about -1.7 to 1.7 AU, the results still indicate a brighter coma in 2021 than in 2015. However, let's remind that the phase angle can also affect the apparent magnitude of comets. In the case of 67P, the angle angle was effectively different during the 2015 and the 2021 observations (see the red curve in the lower panel of Figures 2.5 and 2.6). For that reason, it would be interesting to correct our data for this phase-angle variation and then have a look at the apparent brightness of the comet without any dependence on the geometrical configuration.

[1]Horizons System: `https://ssd.jpl.nasa.gov/horizons.cgi`.

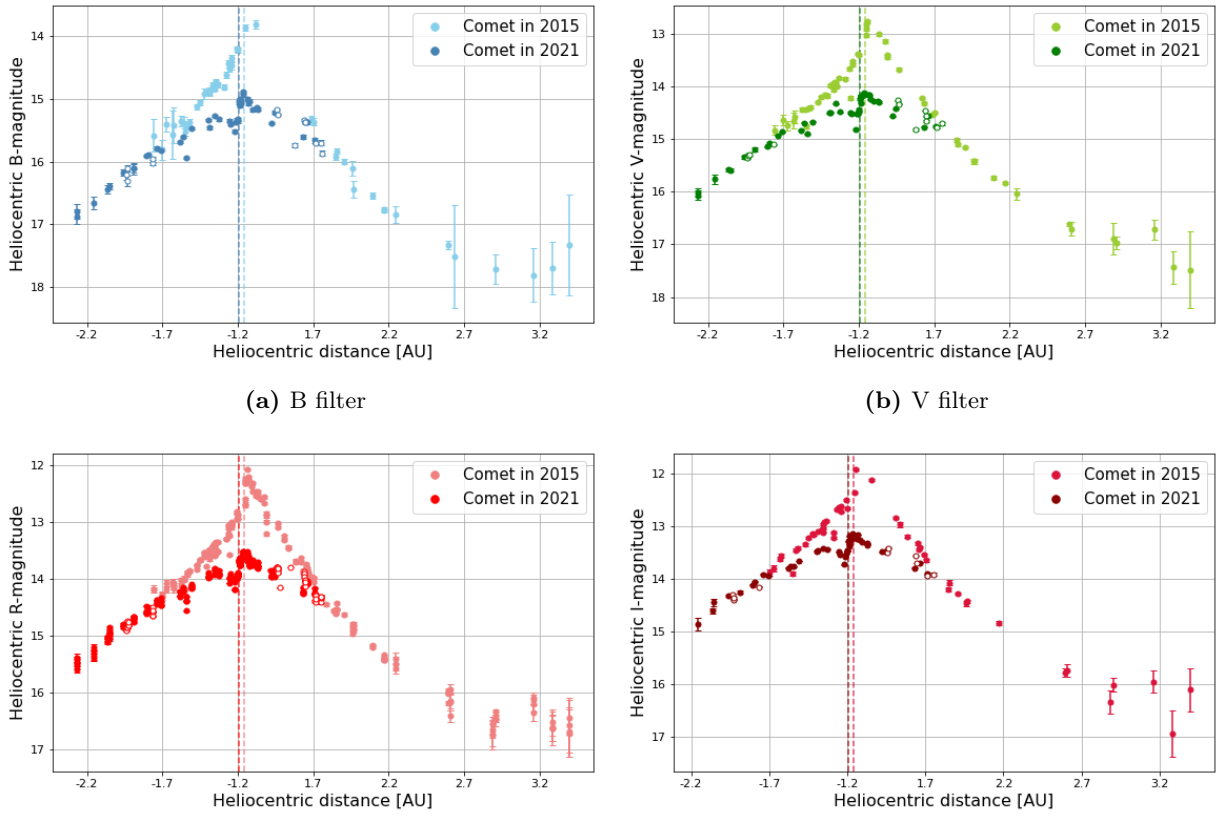

(a) B filter

(b) V filter

(c) R filter

(d) I filter

Figure 3.11. Comparison of the heliocentric magnitude of comet 67P during the perihelion passages in 2015 and 2021. The dashed lines in deep and light colors represent respectively the heliocentric distances at perihelion for the first (1.24 AU) and second (1.21 AU) passages.

The above curves have been separated into parts (before and after the brightness peak) and fitted in order to retrieve the M and n parameters of Equation 3.2. The obtained values, as well as 1σ-uncertainties computed based on these values, are given in Table 3.4 for the two passages of the comet. With all filters, we measure a lower absolute magnitude M in 2015 then in 2021. At the contrary, the power-law exponent n is systematically higher in 2015 than in 2021. Moreover, we measure similar slopes before and after the brightness peak.

Table 3.4. Absolute magnitude M and power-law exponent n of the equation of magnitude fitted for comet 67P.

		M		n	
		Before brightness peak	After brightness peak	Before brightness peak	After brightness peak
B filter	2015	13.20 ± 0.08	13.49 ± 0.28	3.99 ± 0.19	3.52 ± 0.31
	2021	14.66 ± 0.05	14.56 ± 0.10	2.15 ± 0.10	1.81 ± 0.22
V filter	2015	12.28 ± 0.12	11.96 ± 0.12	4.11 ± 0.28	4.35 ± 0.15
	2021	13.81 ± 0.06	13.79 ± 0.09	2.14 ± 0.11	1.57 ± 0.19
R filter	2015	11.76 ± 0.07	11.47 ± 0.07	4.14 ± 0.15	4.26 ± 0.09
	2021	13.28 ± 0.03	13.21 ± 0.04	2.14 ± 0.05	1.70 ± 0.09
I filter	2015	11.61 ± 0.11	11.04 ± 0.15	3.59 ± 0.25	4.34 ± 0.18
	2021	12.91 ± 0.05	12.72 ± 0.05	1.91 ± 0.10	1.88 ± 0.12

Comet 103P/Hartley 2

The light curves obtained for the first and second passages of 103P are shown in Figure 3.12 as a function of time and heliocentric distance. For the first passage of the comet, the observations only started on December 9, 2010, that is 42 days after the date of perihelion (October 28, 2010). As a consequence, for that passage, we were not able to study either the behavior of the comet at the moment of perihelion or the curve asymmetries with respect to the perihelion.

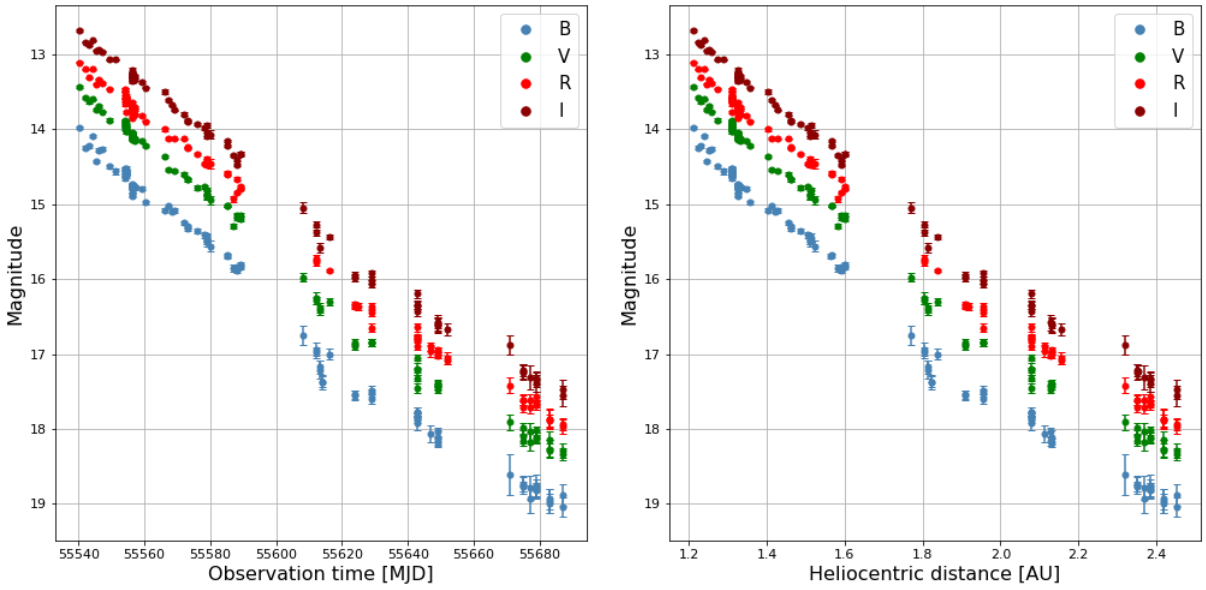

(a) Light curves of 103P during its 2010 passage.

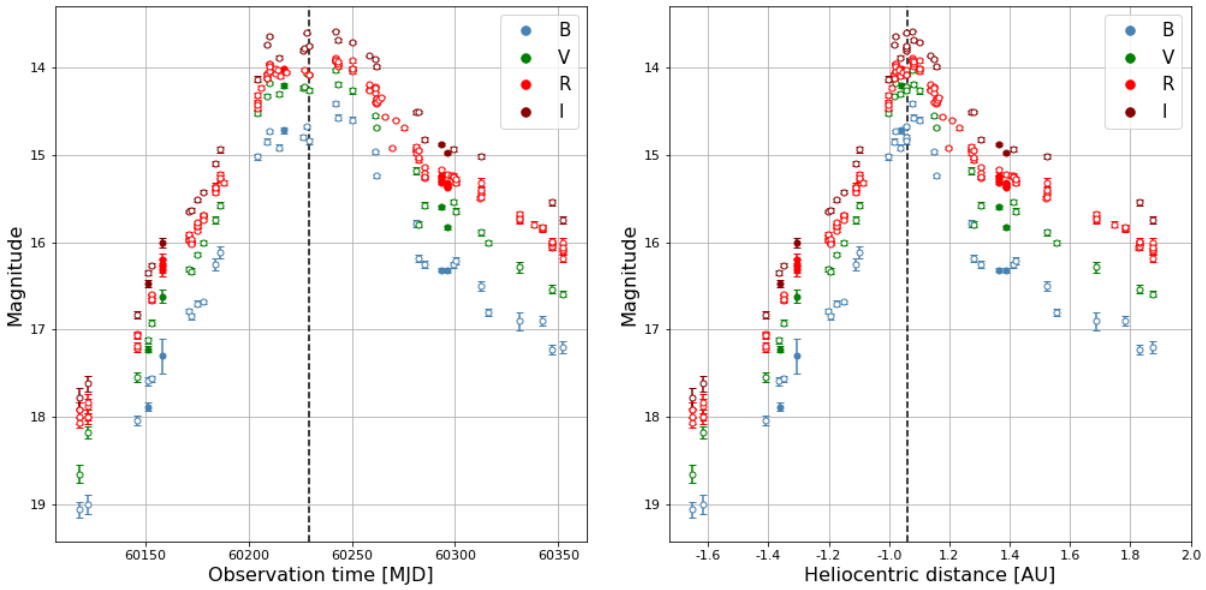

(b) Light curves of 103P during its 2023 passage.

Figure 3.12. Evolution of the magnitude of comet 103P as a function of time (left) and heliocentric distance (right) from December 2010 to May 2011 (upper panels) and from June 2023 to March 2024 (lower panels). The dashed, black line in the lower, left-hand plot represents the perihelion date, i.e., October 12, 2023. Solid and empty points stand for TS and TN data, respectively. Note that the error bars are shown for all data points, but some are smaller than the point size and thus not visible.

First of all, the peak of brightness, not visible in the 2010 light curves, seems to coincide with the date of perihelion in the 2023 light curves. For both passages, the heliocentric-distance-dependent

light curves have been fitted with straight lines in order to retrieve the slopes. The results are shown separately for the different broad-band filters in Figures 3.13 and 3.14 respectively for the first and second passages. Moreover, the computed slopes are given in Table 3.5.

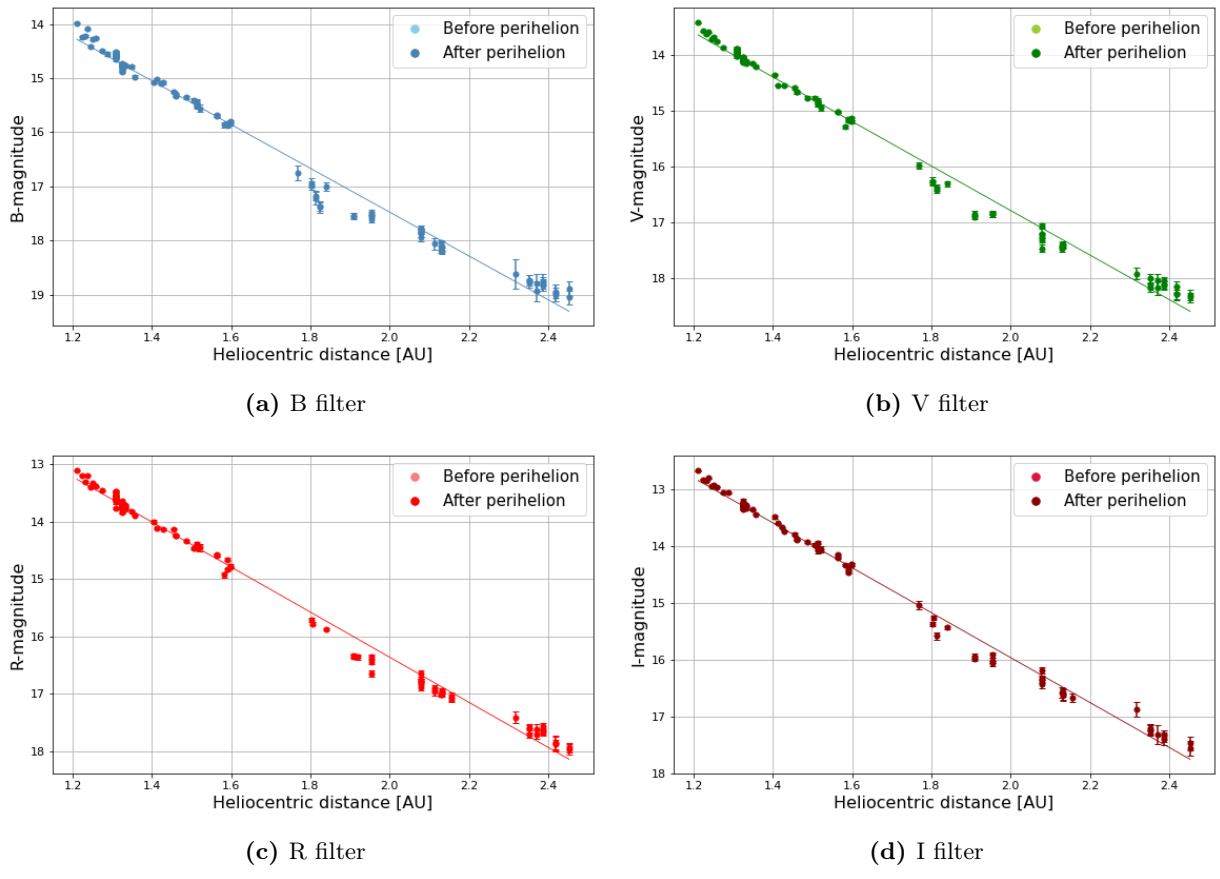

(a) B filter

(b) V filter

(c) R filter

(d) I filter

Figure 3.13. Evolution of the magnitude of comet 103P as a function of the heliocentric distance during its 2010 perihelion passage. Data points have been fitted with a straight line.

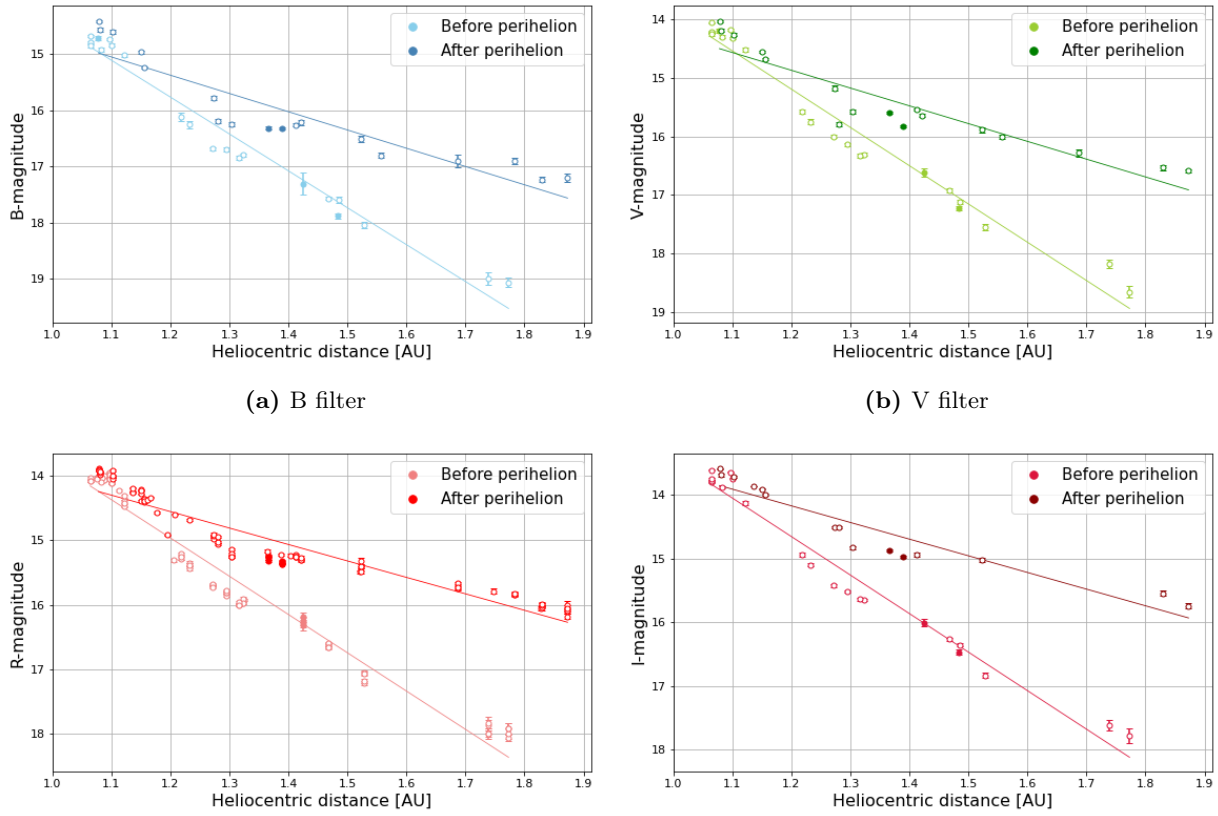

(a) B filter

(b) V filter

(c) R filter

(d) I filter

Figure 3.14. Evolution of the magnitude of comet 103P as a function of the heliocentric distance during its 2023 perihelion passage. Solid and empty points stand for TS and TN data, respectively. Pre-perihelion and post-perihelion data points have been fitted separately with straight lines, represented in respective colors.

Table 3.5. Slopes derived from the linear fit applied on the pre-perihelion and post-perihelion light curves of comet 103P.

		Slopes	
		Pre-perihelion	Post-perihelion
B filter	2010	-	4.04 ± 0.05
	2023	6.57 ± 0.27	3.25 ± 0.34
V filter	2010	-	3.97 ± 0.04
	2023	6.53 ± 0.26	3.03 ± 0.31
R filter	2010	-	3.93 ± 0.03
	2023	5.93 ± 0.15	2.55 ± 0.10
I filter	2010	-	3.95 ± 0.04
	2023	6.05 ± 0.23	2.62 ± 0.25

In Figure 3.14, a noticeable aspect of the light curves can be emphasized. We indeed observe a bend in the post-perihelion part (visible especially with the B, R, and I filters), causing a change in

the slope at around 1.4 AU. The comet brightness does not decrease linearly as expected. Several effects can be considered to explain this peculiar shape. However, at that heliocentric distance, neither the geocentric distance nor the phase angle significantly vary, and we did not notice any distinctive feature in the spatial configuration of the comet (e.g., crossing of the ecliptic plane). Since the bend in the light curves does not seem to be linked to geometrical effects, it would be interesting to investigate the orientation of the cometary tail, for example.

Finally, we have plotted together the light curves obtained during the two passages of 103P to compare them. The results are shown in Figure 3.15 for the different broad-band filters. In these plots, we see that the apparent post-perihelion magnitude measured for the 2010 passage is lower than the one measured for the 2023 passage. However, as explained above, it does not necessarily indicate that the comet activity has increased between the two passages, but it could be due to different geometrical configurations between the Earth, the Sun, and the comet during the observations. To check this, we computed the heliocentric magnitude of 103P, i.e., its apparent magnitude without the dependence on the Earth distance (see Equation 3.2). The results are shown in Figure 3.16.

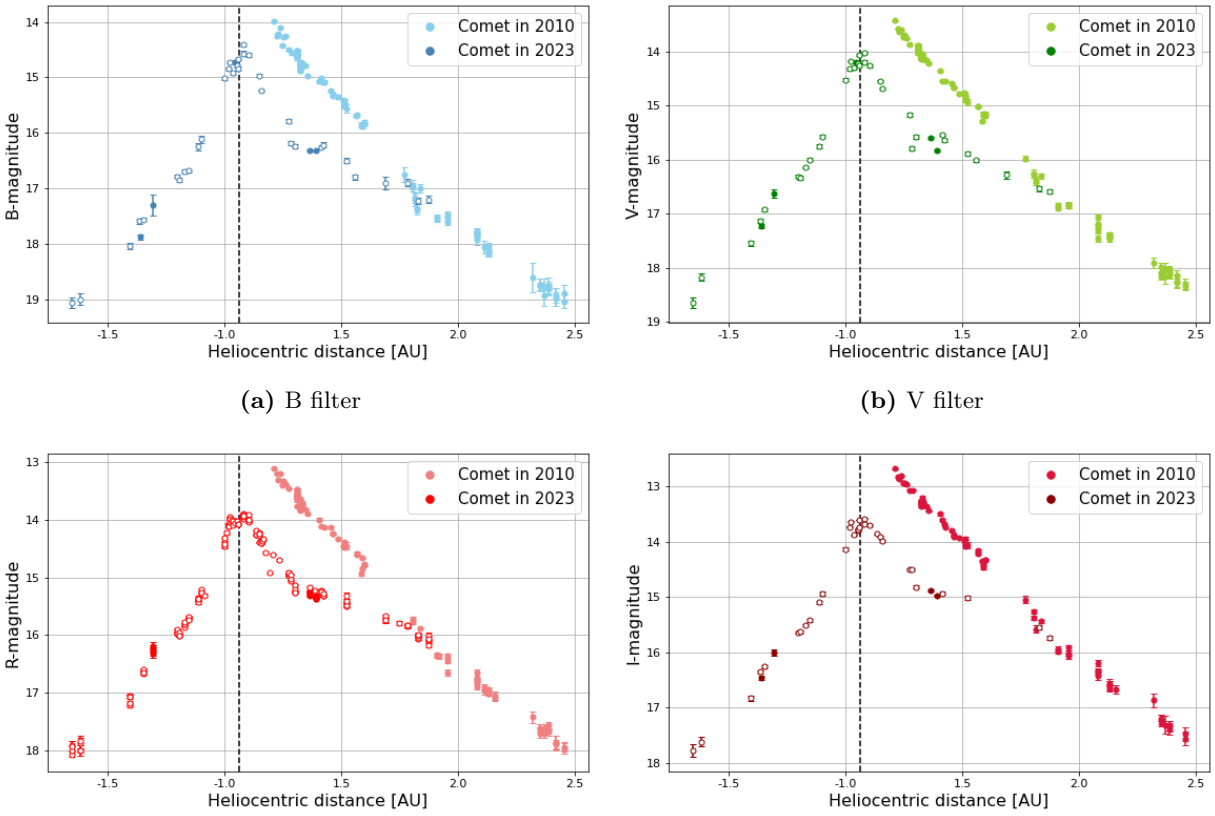

(a) B filter

(b) V filter

(c) R filter

(d) I filter

Figure 3.15. Comparison of the magnitude of comet 103P during the perihelion passages in 2010 and 2023. The dashed, black line in each panel represents the heliocentric distance at perihelion (1.06 AU).

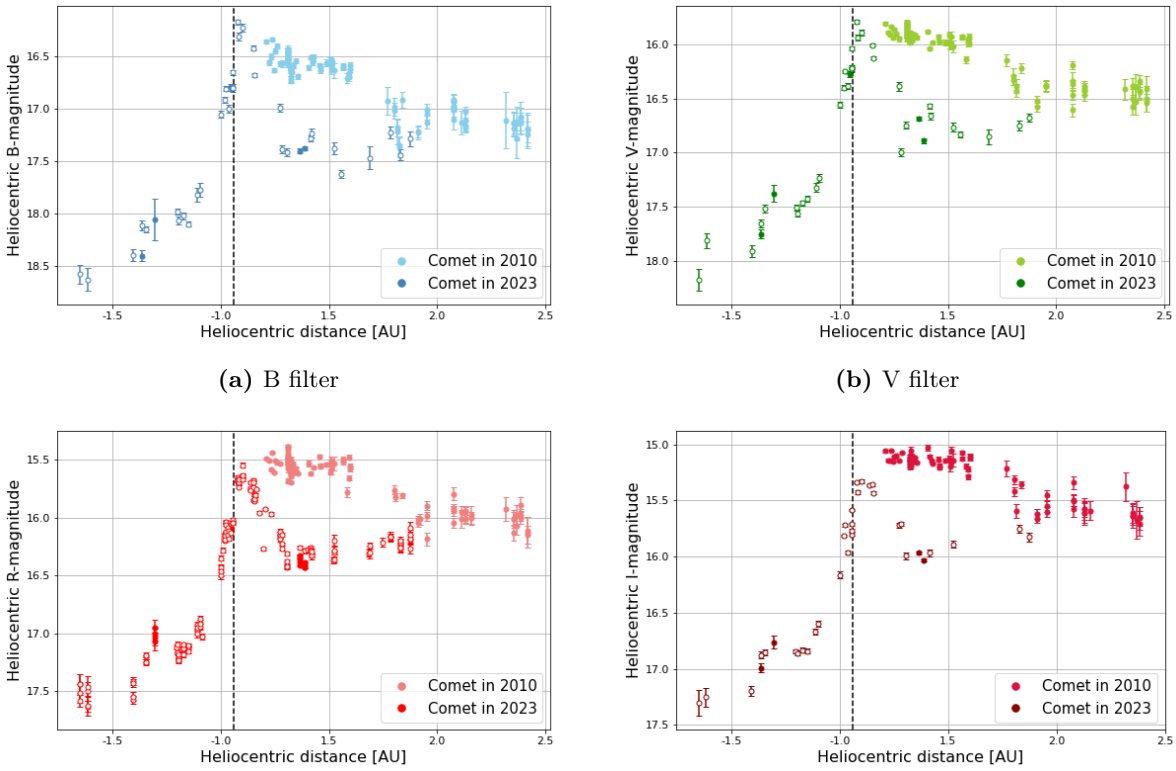

(a) B filter

(b) V filter

(c) R filter

(d) I filter

Figure 3.16. Comparison of the heliocentric magnitude of comet 103P during the perihelion passages in 2010 and 2023. The dashed, black line in each panel represents the heliocentric distance at perihelion (1.06 AU).

In the above plots, representing the heliocentric magnitude of the comet, the curves have a significantly different shape than those presented in Figure 3.15. Again, this shows the great impact of geocentric distance on the measured apparent magnitude. We observe notably that the heliocentric magnitude has not increased much during the first passage, within the heliocentric range from 1.2 to 2.5 after perihelion, contrarily to what was observed before the removal of the geocentric-distance dependence. We can also see the bend identified in Figure 3.14. However, the decreasing trend followed by post-perihelion data seems to reverse beyond this bend. For this reason, we divided the post-maximum part of the curve into two parts for fitting the curve: one part with data points for $r_h < 1.5$ AU (basically before the bend), and another part with data points for $r_h > 1.5$ AU. We then retrieved the M and n parameters of the equation of magnitude (see Equation 3.2) from the pre-perihelion and post-perihelion (before and after the bend) data points, separately. The obtained values are given in Table 3.6.

Table 3.6. Absolute magnitude M and power-law exponent n of the equation of magnitude fitted for comet 103P.

		M		n	
		Before brightness peak	After brightness peak	Before brightness peak	After brightness peak
B filter	2010	-	16.23 ± 0.03	-	1.05 ± 0.05
	2023	16.69 ± 0.10	16.02 ± 0.14 ($r_h > 1.5$ AU)	3.64 ± 0.30	3.66 ± 0.50 ($r_h > 1.5$ AU)
			18.36 ± 0.40 ($r_h < 1.5$ AU)		-1.58 ± 0.65 ($r_h < 1.5$ AU)
V filter	2010	-	15.63 ± 0.02	-	0.93 ± 0.04
	2023	16.12 ± 0.10	15.60 ± 0.06 ($r_h > 1.5$ AU)	3.62 ± 0.31	2.99 ± 0.41 ($r_h > 1.5$ AU)
			16.83 ± 0.13 ($r_h < 1.5$ AU)		-0.16 ± 0.28 ($r_h < 1.5$ AU)
R filter	2010	-	15.28 ± 0.02	-	0.82 ± 0.04
	2023	15.90 ± 0.06	15.24 ± 0.06 ($r_h > 1.5$ AU)	3.23 ± 0.20	3.58 ± 0.28 ($r_h > 1.5$ AU)
			16.51 ± 0.03 ($r_h < 1.5$ AU)		-0.48 ± 0.06 ($r_h < 1.5$ AU)
I filter	2010	-	14.86 ± 0.03	-	0.83 ± 0.05
	2023	15.57 ± 0.10	14.94 ± 0.08 ($r_h > 1.5$ AU)	3.29 ± 0.32	3.11 ± 0.36 ($r_h > 1.5$ AU)
			16.23 ± 0.08 ($r_h < 1.5$ AU)		-0.66 ± 0.15 ($r_h < 1.5$ AU)

3.5 Colors of the comets

Color indexes are commonly used in order to characterize the colors of a comet (or more exactly, the colors of the coma). Analyzing color indexes is very useful to compare the dust composition of different comets. Indeed, as the colors that we measure are due to the reflection and scattering of solar light by cometary dust grains, it can provide some information about the dust grains in the coma, especially their size.

To study the colors of 67P and 103P's coma, we used the magnitude of the comets measured with the BVRI Johnson-Cousins filters and computed the B−R, B−V, V−R, and R−I color indexes. We analyzed the evolution of these indexes as a function of the heliocentric distance, and we compared the results obtained for both comets and both passages of each comet. The results are presented in this section.

Comet 67P/Churyumov-Gerasimenko

Figures 3.17 and 3.18 show the evolution of the B−R, B−V, V−R, and R−I color indexes of 67P as a function of the heliocentric distance of the comet, respectively for its first and second perihelion passages.

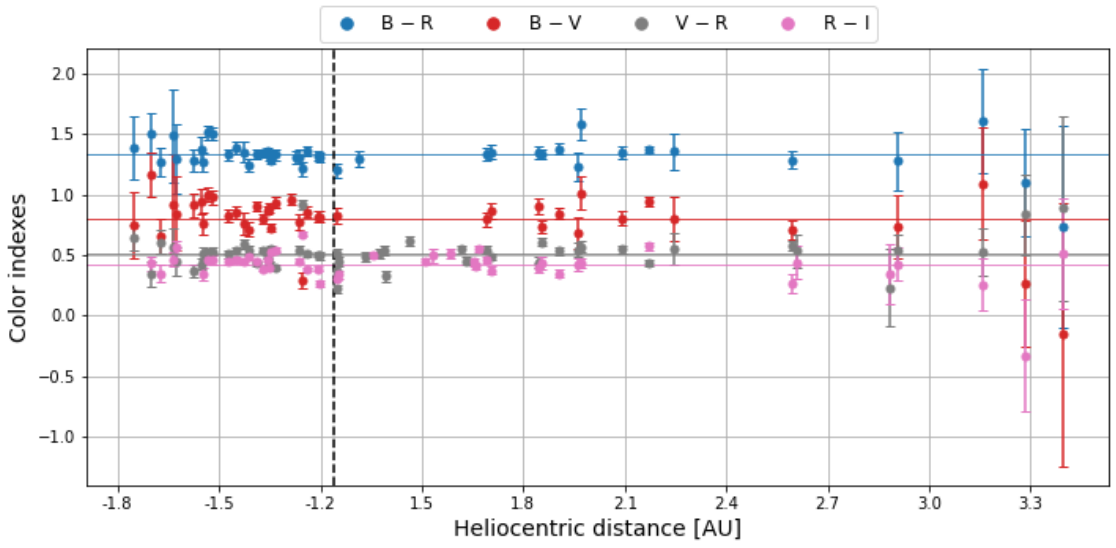

Figure 3.17. Variation of the color indexes of comet 67P as a function of heliocentric distance during its 2015 perihelion passage. The dashed, black line represents the heliocentric distance at perihelion, i.e., 1.24 AU. The mean value of each color index is represented as a horizontal line.

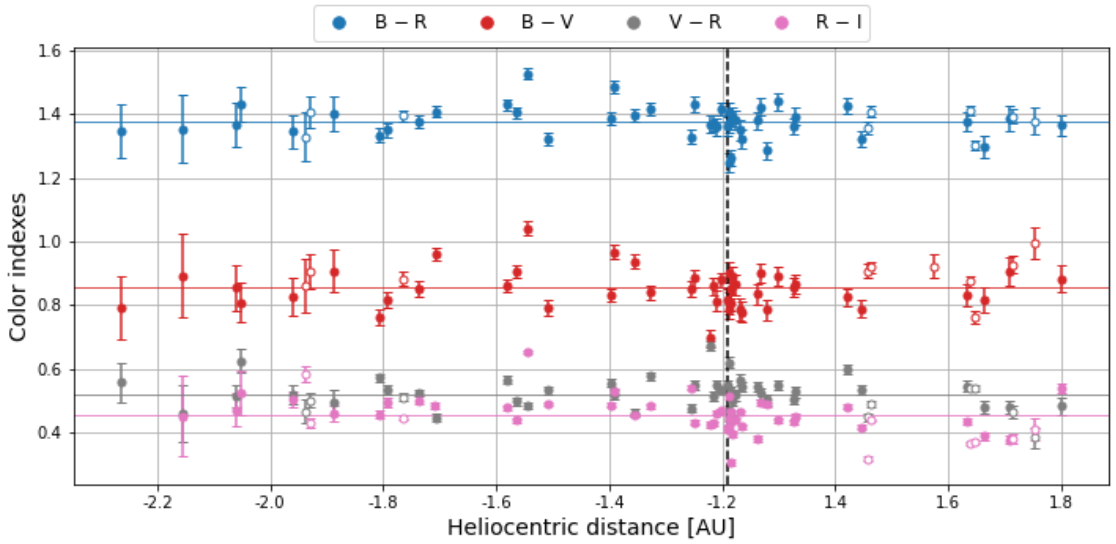

Figure 3.18. Variation of the color indexes of comet 67P as a function of heliocentric distance during its 2021 perihelion passage. The dashed, black line represents the heliocentric distance at perihelion, i.e., 1.21 AU. The mean value of each color index is represented as a horizontal line.

First of all, we do not detect any significant variation of the color indexes while the heliocentric distance changes, except the variation observed beyond $r_h = 3$ AU for the first passage, but given the large uncertainties, we do not consider it. We computed the mean value of each color index. The results are given in Table 3.7 and are overplotted in the above figures.

Table 3.7. Mean color indexes computed for comet 67P during its 2015 and 2021 perihelion passages.

	Mean color indexes		Mean color indexes for active JFCs[a]	Solar colors[b]
	2015	2021		
B − R	1.33 ± 0.03	1.38 ± 0.01	1.22 ± 0.02	0.99 ± 0.02
B − V	0.80 ± 0.04	0.86 ± 0.01	0.75 ± 0.02	0.64 ± 0.02
V − R	0.52 ± 0.02	0.52 ± 0.01	0.47 ± 0.02	0.35 ± 0.01
R − I	0.42 ± 0.02	0.45 ± 0.01	0.44 ± 0.02	0.33 ± 0.01

[a] Values taken from Solontoi et al. (2012).

[b] Values taken from Holmberg et al. (2006).

According to our results, the color indexes did not significantly change between 2015 and 2021. Our values are slightly higher but still consistent with the mean color indexes for active JFCs (see for example the values computed by Solontoi et al. (2012) that are given in the table). Moreover, as it is expected for comets, the colors that we measured for 67P are redder than solar colors (if we compare our results with the solar colors given in Holmberg et al. (2006)).

Comet 103P/Hartley 2

The variation of B−R, B−V, V−R, and R−I color indexes of 103P as a function of the heliocentric distance is plotted in Figures 3.19 and 3.20, respectively for the first and second passages of the comet. The mean value for each index has also been computed. The results are shown as horizontal lines in the plots and given in Table 3.8.

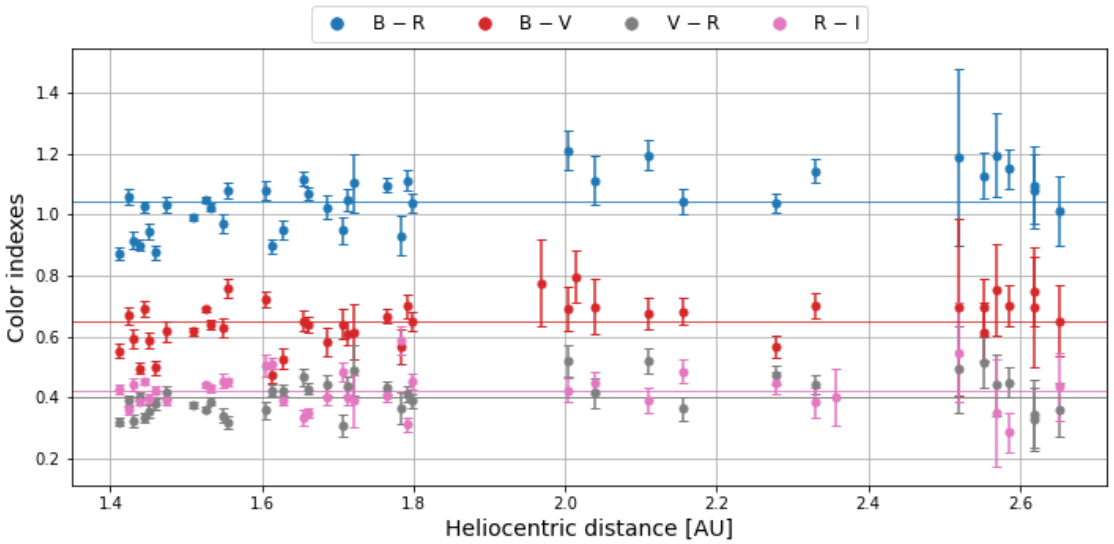

Figure 3.19. Variation of the color indexes of comet 103P as a function of heliocentric distance during its 2010 perihelion passage. The dashed, black line represents the heliocentric distance at perihelion, i.e., 1.06 AU. The mean value of each color index is represented as a horizontal line.

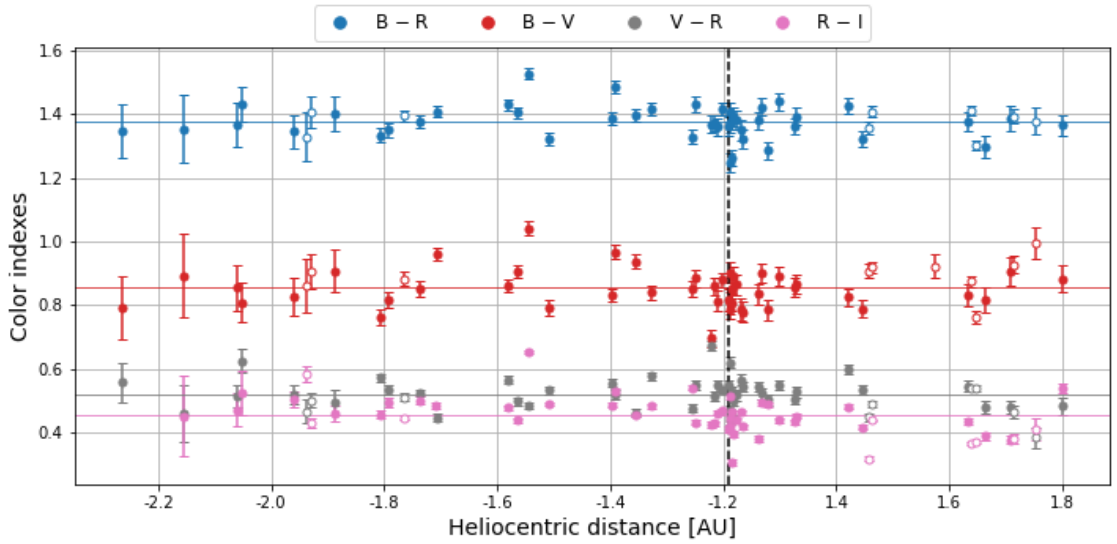

Figure 3.20. Variation of the color indexes of comet 103P as a function of heliocentric distance during its 2023 perihelion passage. The dashed, black line represents the heliocentric distance at perihelion, i.e., 1.06 AU. The mean value of each color index is represented as a horizontal line.

Table 3.8. Mean color indexes computed for comet 103P during its 2010 and 2023 perihelion passages.

	Mean color indexes		Mean color indexes for active JFCs[a]	Solar colors[b]
	2010	2023		
B − R	1.04 ± 0.01	0.90 ± 0.01	1.22 ± 0.02	0.99 ± 0.02
B − V	0.65 ± 0.01	0.56 ± 0.01	0.75 ± 0.02	0.64 ± 0.02
V − R	0.40 ± 0.01	0.34 ± 0.01	0.47 ± 0.02	0.35 ± 0.01
R − I	0.42 ± 0.01	0.33 ± 0.01	0.44 ± 0.02	0.33 ± 0.01

[a] Values taken from Solontoi et al. (2012).

[b] Values taken from Holmberg et al. (2006).

Contrarily to what we noticed for 67P, we detect here a clear decrease in all the color indexes between 2010 and 2023. This might be due, for example, to a change in the surface's dust composition of the comet between the two passages. For both passages, we observe color indexes that are consistent with the mean values for JFCs (given in the table), although, except for the R − I color index measured in 2023, they are slightly lower. We also observe that, as for 67P, the comet colors are redder than solar colors. However, we can notice that the difference between solar colors and the colors measured for 103P is much lower than what we obtained for 67P.

Chapter 4

Molecular production rates

The OH, NH, CN, C_2, and C_3 molecules are generally easy to detect in cometary comae. However, they do not directly come from the sublimation of cometary ices, but are formed from parent molecules that were part of the cometary ice composition. Indeed, further to solar radiation absorption by the nucleus, these parent molecules sublimate and are then dissociated or ionized by the solar UV photons, giving rise to numerous daughter molecules. By using the narrow-band gas filters mounted on the TRAPPIST telescopes, the daughter molecules can be detected in cometary comae. Their production rates correspond to the number of molecules released in the coma per second. To be able to calculate the cometary gas production rates based on comet observations, a modeling of the temporal evolution of chemical species in the coma is necessary.

This chapter describes the Haser model, that is commonly used to compute the production rates of daughter species in the coma of comets. We present our results obtained by employing this model. We also used the calculated C_2 and CN production rates in order to classify our target comets according to their chemical composition, based on a criterion defined by A'Hearn et al. (1995). Finally, we derived the water production rate in the coma of 67P and 103P, starting from their respective OH production rates. The results are presented at the end of this chapter.

4.1 The Haser model

In 1957, Leo Haser, from the Astrophysics Institute of the University of Liège, developed a model describing the density distribution of daughter molecules in the expanding coma of comets (Haser, 1957). See Haser et al. (2020) for the English version of his paper. This model allows an estimation of the cometary gas production rates.

4.1.1 Description of the model

The Haser model is based on a few straightforward hypothesis:

- The cometary nucleus is spherical, and its radius is given by r_0.
- As the nucleus absorbs solar radiation, its iced chemical components sublimate and escape from the nucleus in every directions with a constant radial velocity v_0, thus forming a spherically symmetric coma.
- The gaseous parent species are disintegrated by photodissociation to form daughter species, which also flow in the radial direction. These daughter species can then also be photodissociated, leading to the formation of granddaughter species. No other chemical process of production or destruction of molecules is taken into account.
- The molecular photodissociation follows a first-order kinetic law given by the equation

$$n = n_0 \exp\left(\frac{-t}{\tau_0}\right), \tag{4.1}$$

  where n_0 is the number of molecules present at time $t = 0$, and τ_0 is the average lifetime of a parent molecule in the coma before being photodissociated. τ_0 thus depends on several parameters such as the solar activity, the heliocentric distance of the comet, etc.

It it worth mentioning that this model is rather simple but not physically accurate. Indeed, in reality, neither the cometary nucleus nor the coma are spherically symmetric, and the gas is not ejected uniformly from the nucleus surface, some regions of the comet being more active than others. Moreover, photodissociation is not the only chemical process likely to happen in the coma. Some more complex reactions might also lead to significant changes in the gas composition of the coma, and so, the identified daughter species probably originate from more than one parent molecule. However, although the model does not describe cometary comae with precision, it is currently the best model to constrain comet activity. It is based on an empirical calculation of the molecular scale lengths (see below), which compensates for the simplicity of the model. Thus, it provides a good approximation of the molecular production rates in cometary comae, and consequently, it is widely used by astronomers. Furthermore, let's remind that, as explained in the previous chapter, the observations of 67P with TRAPPIST did not allow the identification of outbursts, although the instruments abroad the Rosetta spacecraft had measured some very small ones. Since the telescopes were not able to detect the small outbursts occurring in the coma, the model to use for the computation of some parameters linked to the comet activity does not need to be more precise to be in accord with our data. The Haser model is thus relevant in the case of our work. We could also eventually turn to the vectorial model for the calculation of gas production rates. The vectorial

model is a more realistic model describing cometary comae, developed by Festou (1981). It notably takes into account the non-radial motion of neutral species in comae due, on one hand, to the collisions between the gaseous molecules, and on the other hand, to the energy released during the production of daughter molecules. However, this model is mathematically much more complicated, and does not provide significantly different results.

The Haser model consists in computing the density profile of the dissociation products (i.e., the daughter molecules) in the coma of a comet. By integrating this density profile in the line of sight, we can then obtain the column density of the daughter molecules, and by establishing a link between the column density and the brightness profile of the comet, the molecular production rates can be estimated.

First of all, the density distribution of the daughter molecules in the coma can be computed based on the above assumptions. If $N(r_0)$ is the number of molecules that escape from the nucleus per second and per unit area, and if $N(x)$ is the number of molecules that arrive at a distance X from the nucleus per second and per unit area, then the total number of molecules crossing a sphere of radius X is given by

$$4\pi\ X^2\ N(X) = 4\pi\ r_0^2\ N(r_0)\ \exp\left[-\frac{1}{v_0\tau_0}\ (X - r_0)\right], \tag{4.2}$$

where v_0 and τ_0 respectively correspond to the velocity and lifetime of parent molecules. Thus, the production rate of daughter molecules (per second and per unit area) in a shell of thickness dX located at a distance X from the nucleus is given by

$$-\frac{d}{dX}\ [4\pi\ X^2\ N(X)] = 4\pi\ r_0^2\ N(r_0)\ \frac{1}{v_0\tau_0}\ \exp\left[-\frac{1}{v_0\tau_0}\ (X - r_0)\right]. \tag{4.3}$$

Once they are formed in the coma, the daughter molecules also undergo photodissociation processes due to solar photons. Therefore, when the daughter molecules formed at a distance X from the nucleus reach the distance r, their number has decreased by a factor $\exp\left[-\frac{r-X}{v_1\tau_1}\right]$, v_1 and τ_1 being respectively their velocity and lifetime. Consequently, the number of daughter molecules, originating from a layer of thickness dX located at a distance X from the nucleus, that arrive at the distance r is

$$4\pi\ r_0^2\ N(r_0)\ \frac{1}{v_0\tau_0}\ \exp\left[-\frac{1}{v_0\tau_0}\ (X - r_0)\right]\ \exp\left[-\frac{r - X}{v_1\tau_1}\right]\ dX, \tag{4.4}$$

and so, the total number of daughter molecules reaching the sphere of radius r around the comet

nucleus (per second and per unit area) is given by

$$N_1(r) = N(r_0) \left(\frac{r_0}{r}\right)^2 \frac{1}{v_0\tau_0} \exp\left[\frac{r_0}{v_0\tau_0}\right] \int_{r_0}^{r} \exp\left[-\frac{X}{v_0\tau_0} - \frac{r-X}{v_1\tau_1}\right] dX. \tag{4.5}$$

The molecular density in the coma (i.e., the number of molecules per unit area), noted $D(r)$, is linked to the quantities $N(r_0)$ and $N_1(r)$ defined above through the relations

$$N(r_0) = v_0 D(r_0) \qquad \text{and} \qquad N_1(r) = v_1 D_1(r). \tag{4.6}$$

Moreover, we introduce the quantities β_0 and β_1, which correspond respectively to the characteristic scale lengths of the parent and daughter molecules in the coma, associated to their lifetime before being destroyed by photodissociation. These quantities are defined as

$$\beta_0 = \frac{1}{v_0\tau_0} \qquad \text{and} \qquad \beta_1 = \frac{1}{v_1\tau_1}. \tag{4.7}$$

By using equations 4.6 and 4.7, along with the expression of the molecular production rate Q, that is

$$Q = 4\pi v_0 r_0^2 D(r_0), \tag{4.8}$$

the expression of the density distribution of the daughter molecules in the coma is finally obtained:

$$D_1(r) = \frac{Q}{4\pi r^2 v_1} \beta_0 \frac{\exp[-\beta_0(r-r_0)] - \exp[-\beta_1(r-r_0)]}{\beta_1 - \beta_0}. \tag{4.9}$$

Equation 4.9 is known as the Haser formula. Integrating it along the line of sight enables to obtain the column density $N(r)$ of the daughter species. The integration can either be done analytically or numerically. The analytical method is presented in details in Haser's paper, but was not used for this work. Instead, we used the numerical method which consists in a direct integration of the molecular density along a line of sight. It gives

$$N(r) = \frac{Q}{4\pi v_1} \int_{-z}^{z} e(r) dz, \tag{4.10}$$

where $e(r)$ is the emissivity as a function of the distance r in the coma:

$$e(r) = \frac{1}{r^2} \frac{\beta_0}{\beta_1 - \beta_0} \left[\exp(-\beta_1(r)) - \exp(-\beta_0(r))\right]. \tag{4.11}$$

Finally, the column density $N(r)$ of molecules in the coma can be linked to the flux, per unit solid angle, emitted through fluorescence processes. In the case of an optically thin medium, the

two quantities can be linked via the equation (see Swamy (2010)):

$$N(r) = \frac{4\pi}{g}\frac{1}{\Omega}F, \tag{4.12}$$

where F is the flux emitted within a given solid angle Ω, and g is the fluorescence efficiency of molecules (also called g-factor) which corresponds to the probability of scattering of a solar photon per unit time per molecule. This quantity is given by

$$g_\lambda = \left(\frac{\pi e^2}{m_e c^2}\right) \lambda^2 f_\lambda F_\lambda \frac{A_{ik}}{\sum_k A_{ik}}, \tag{4.13}$$

where f_λ is the absorption oscillator strength, F_λ is the solar flux per unit wavelength and A_{ik} are the Einstein coefficients. The fluorescence efficiency is thus dependent on the considered molecule, and the g-factors for different species are available in the literature.

In this way, the flux of the comets measured with a given narrow-band gas filter can be converted into a column density of the corresponding molecular species in the coma, and this quantity can then be used to estimate the gas production rate of of molecules.

4.1.2 Application of the model

In this work, the molecular production rates have been computed numerically with a program that implements the Haser model. In a few words, the program uses comet images obtained with the gas filters, subtracts the dust continuum from the radial profiles, and then calculates the production rates based on the Haser model using these profiles. The lifetime and g-factor values of the parent and daughter species (OH, NH, CN, C_2, and C_3), necessary for the computation, are automatically taken from D. Schleicher's website[1]. Moreover, the orbital parameters of the comets (not contained in the image headers) are taken from NASA's JPL Horizons website[2]. The model has been adjusted for nucleocentric distances between $10^{3.6}$ and $10^{4.1}$ km (see the dashed, grey line in Figure 3.5). This distance range was chosen as a compromise between seeing effects and dust contamination that can affect the results at smaller nucleocentric distances, and the too low signal-to-noise ratio obtained at larger distances.

4.2 Results and discussion

The gas production rates of OH, NH, CN, C_2, and C_3 have been computed on the basis of each image obtained during the two perihelion passages of both 67P and 103P. In this way, we were

[1]Calculate Comet Fluorescence Efficiency: `https://asteroid.lowell.edu/comet/gfactor.html`
[2]Horizons System: `https://ssd.jpl.nasa.gov/horizons.cgi`

able to follow the evolution of the production rates of the different molecular species as comets were travelling closer to the Sun. This section presents the results we obtained separately for both passages of each comet, as well as a comparison of these results in order to highlight the similarities and differences in comet activity from one perihelion passage to the other. Moreover, when both CN and C_2 data were available, a ratio of the production rates of these two species was computed. The evolution of these ratios as a function of heliocentric distance and their change from one passage to the other were then studied. The results have been used to classify the comets in terms of chemical composition, according to a criterion defined by A'Hearn et al. (1995). Finally, the water production rates of 67P and 103P have been inferred from the computed OH production rates using an empirical formula. The obtained values are given in the last part of this section.

4.2.1 Gas production rates

Comet 67P/Churyumov-Gerasimenko

The gas production rate values (in molecules per second) measured for the 2015 perihelion passage of 67P are given in the appendix in Table A.1. During this passage, only the CN and C_2 gaseous molecules have been probed (see the filters used for the observations in Figure 2.5), and very few data were available for these species. The comet was indeed difficult to observe due to its position in the sky and with respect to the Earth. Consequently, it was difficult to accurately follow the evolution of these production rates. Nonetheless, our values are consistent with those obtained by Opitom et al. (2017) and Snodgrass et al. (2016).

More results have been obtained for the much more favorable passage of 67P in 2021. They are listed in the appendix in Table A.2. The evolution of the production rates Q measured for this second passage is also represented in Figures 4.1 to 4.5 for each molecular species, as a function of time and heliocentric distance. Moreover, the curves representing the heliocentric-distance dependence of Q have been separated into two parts: one part with the data points measured before the peak of gas production rate, and another part with the data points measured after this peak. The two parts have then been fitted separately with a power law with the aim of retrieving the slopes. The result of the fits can be seen in the figures, and the computed slopes are given in Table 4.1.

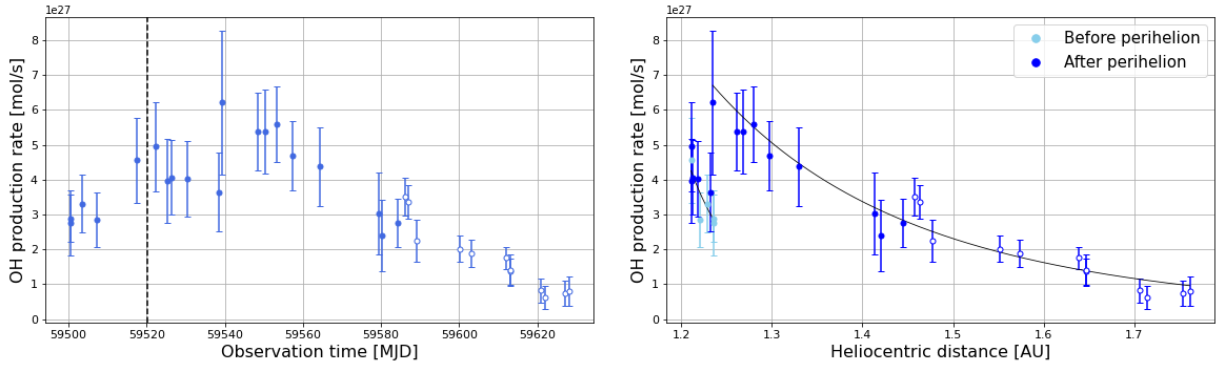

Figure 4.1. Evolution of the OH production rate in the coma of comet 67P as a function of time (left) and heliocentric distance (right) during perihelion passage in 2021. The dashed, black line in the left-hand plot represents the date of perihelion (November 2, 2021). The black curves in the right-hand plot represent the power-law fit applied on the pre-maximum and post-maximum data points. Solid and empty points stand for TS and TN data, respectively.

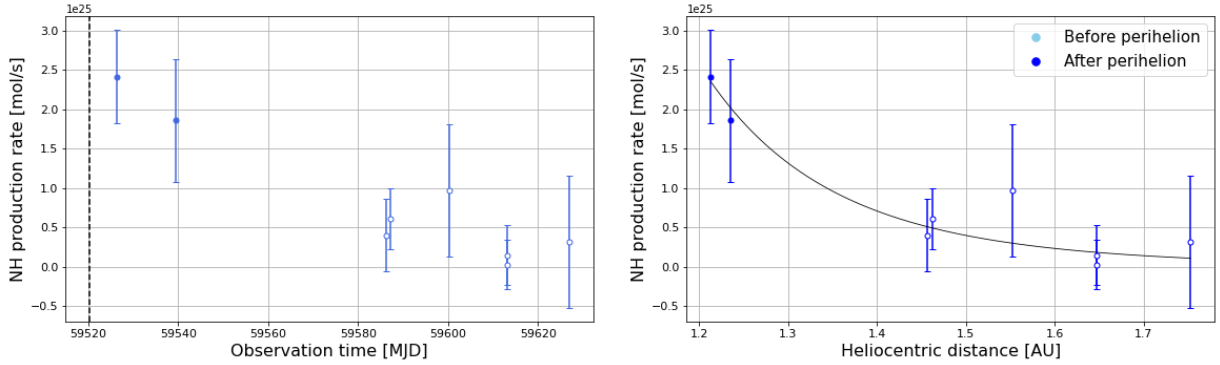

Figure 4.2. Evolution of the NH production rate in the coma of comet 67P as a function of time (left) and heliocentric distance (right) during perihelion passage in 2021. The dashed, black line in the left-hand plot represents the date of perihelion (November 2, 2021). The black curve in the right-hand plot represents the power-law fit applied on the data points. Solid and empty points stand for TS and TN data, respectively.

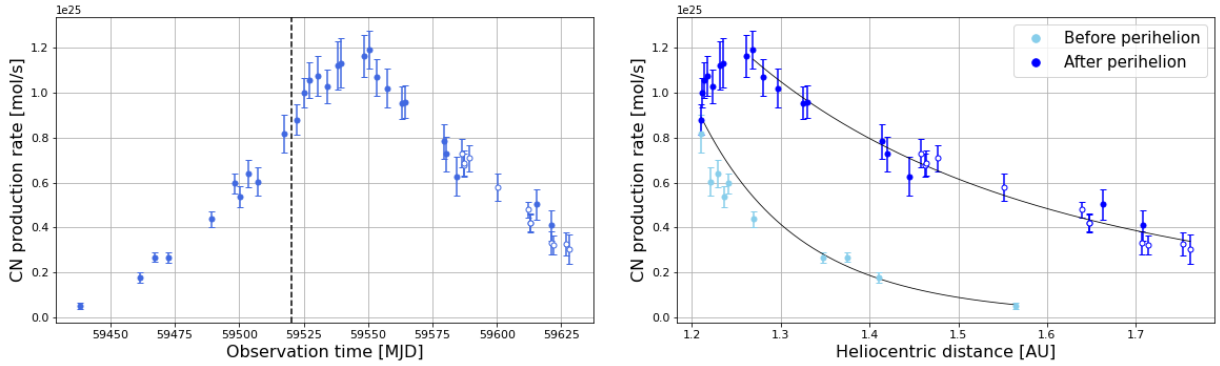

Figure 4.3. Evolution of the CN production rate in the coma of comet 67P as a function of time (left) and heliocentric distance (right) during perihelion passage in 2021. The dashed, black line in the left-hand plot represents the date of perihelion (November 2, 2021). The black curves in the right-hand plot represent the power-law fit applied on the pre-maximum and post-maximum data points. Solid and empty points stand for TS and TN data, respectively.

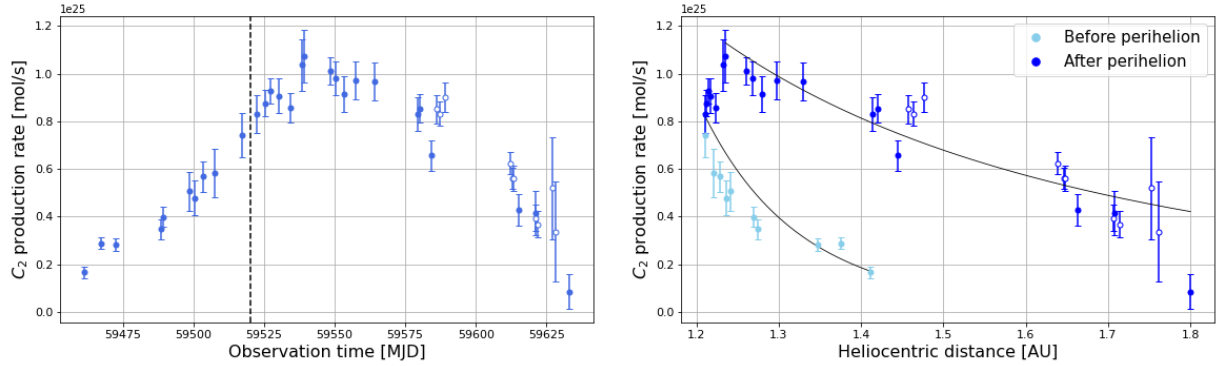

Figure 4.4. Evolution of the C_2 production rate in the coma of comet 67P as a function of time (left) and heliocentric distance (right) during perihelion passage in 2021. The dashed, black line in the left-hand plot represents the date of perihelion (November 2, 2021). The black curves in the right-hand plot represent the power-law fit applied on the pre-maximum and post-maximum data points. Solid and empty points stand for TS and TN data, respectively.

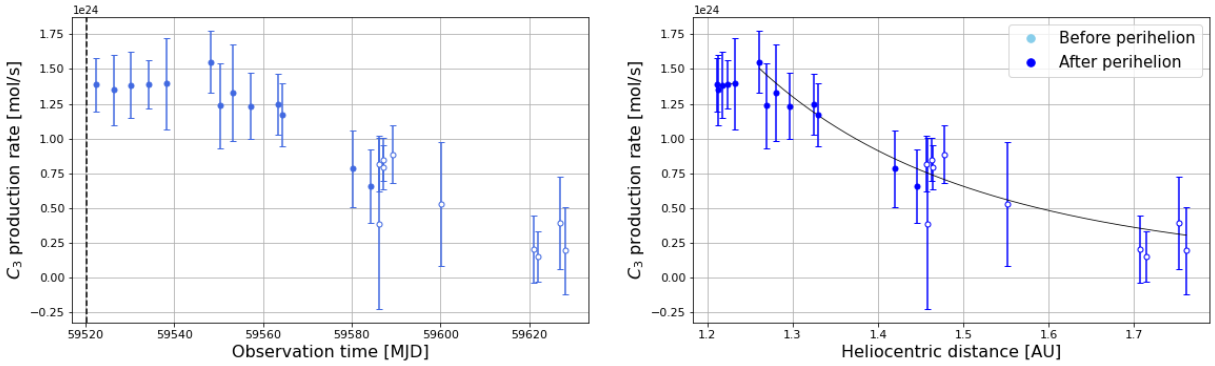

Figure 4.5. Evolution of the C_3 production rate in the coma of comet 67P as a function of time (left) and heliocentric distance (right) during perihelion passage in 2021. The dashed, black line in the left-hand plot represents the date of perihelion (November 2, 2021). The black curves in the right-hand plot represent the power-law fit applied on the pre-maximum and post-maximum data points. Solid and empty points stand for TS and TN data, respectively.

Table 4.1. Fitted power-law slopes derived from the heliocentric-distance dependence of gas production rates measured for the 2021 perihelion passage of comet 67P.

	r_h-dependence	
Species	Before Q maximum	After Q maximum
OH	19.75 ± 5.19	-5.48 ± 0.37
NH	-	-8.38 ± 1.21
CN	10.71 ± 1.40	-3.72 ± 0.14
C_2	10.22 ± 1.25	-2.62 ± 0.31
C_3	0.99 ± 0.97	-4.78 ± 0.45

The comet activity can be studied through the evolution of the production rates of OH, CN, and C_2, for which we have both pre-perihelion and post-perihelion data. We observe an asymmetry in the curves with respect to perihelion, that had already been highlighted thanks to the light curves (see the previous chapter). We notice a difference of two orders of magnitude between the production rates of OH and those of CN and C_2. This is reasonable, since the OH daughter species in the coma come from H_2O molecules, which are abundant in cometary ices. Except this numerical difference, all three species behave approximately the same. The outgassing slowly increases before reaching a maximum value several days after perihelion, and then decreases while the comet gets away from the Sun. Although the exact time interval between the date of perihelion and the date of production rate peak is difficult to determine, it should vary from 10 to 30 days, according to our data. Moreover, it seems to differ from one species to another.

With the aim of finding similarities and differences in the activity of the comet between 2015

and 2021, we also compared the gas production rates obtained for the two passages. Since only the CN and C2 filters have been used to observe the comet during the first passage of 67P, this comparison was not possible with the other filters. Figure 4.6 shows the evolution of the CN and C_2 production rates measured in 2010 and 2023, as a function of the heliocentric distance of the comet.

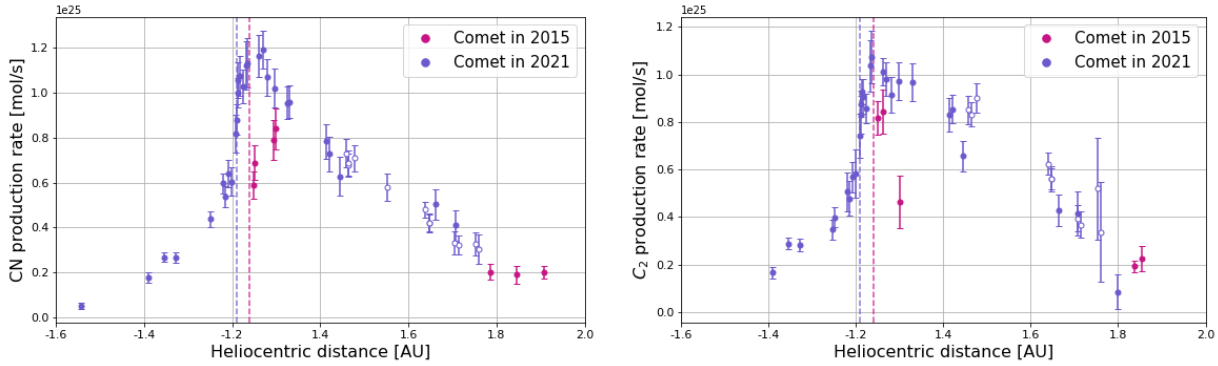

(a) CN production rate

(b) C_2 production rate

Figure 4.6. Comparison of the production rates of comet 67P between 2015 and 2021. The dashed lines represent the heliocentric distances at perihelion (1.24 AU in 2015 and 1.21 AU in 2021) in respective colors. Solid and empty points stand for TS and TN data, respectively.

In the above plots, we can see that the CN and C_2 production rates were slightly lower in 2015 than in 2021, which might indicates a less intense activity of the comet.

Comet 103P/Hartley 2

Let's now have a look at the production rates of the different species measured in the coma of 103P. Table A.3 in the appendix gathers the values obtained for the first passage of the comet. The obtained production rates have also been plotted as a function of time and heliocentric distance. Results are shown in Figures 4.7 to 4.10 for the different species. As a reminder, the observations only started several days after the passage of the comet at perihelion. Please note also that the NH filter was not used for collecting the data, so we were not able to compute the production rates of this species.

To begin with, despite its small size, we see that 103P is a very active comet, with OH production rates of the order of 10^{27} molecules per second. We can compare our values with those obtained by Knight, Schleicher (2013), who also observed the 2010 perihelion passage of 103P with the Hall Telescope at Lowell Observatory. Their methods were comparable to ours: they used the HB narrow-band filters and computed the molecular production rates on the basis of the Haser model. The Q values they obtained for the post-perihelion phase are shown as red data points in our

time-dependent curves of the production rates (see the left-hand part of Figures 4.7 to 4.10). Their results are in excellent agreement with ours. We fitted the power-law slopes of the heliocentric-distance-dependent variation of the gas production rates. The fitted power laws can be seen in the different figures, and the slope values obtained are given in Table 4.2.

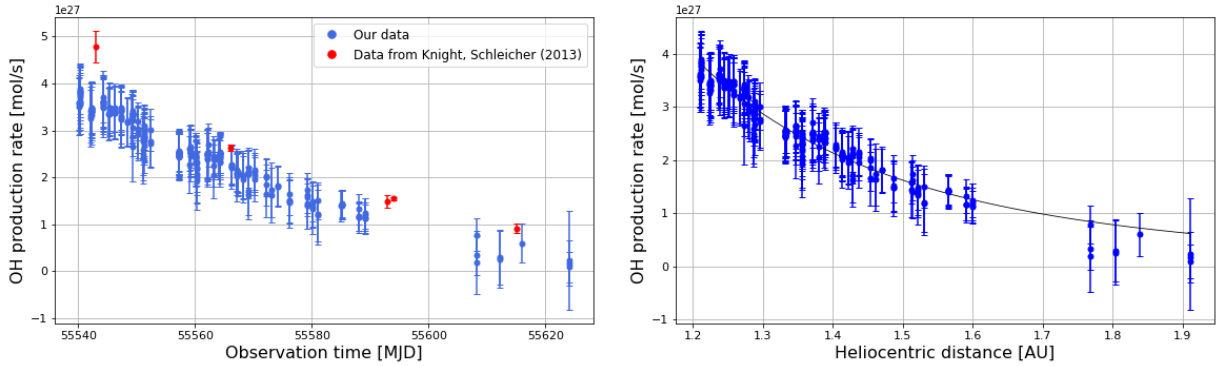

Figure 4.7. Evolution of the OH production rate in the coma of comet 103P as a function of time (left) and heliocentric distance (right) during perihelion passage in 2010. The black curve in the right-hand plot represents the power-law fit applied on the data points.

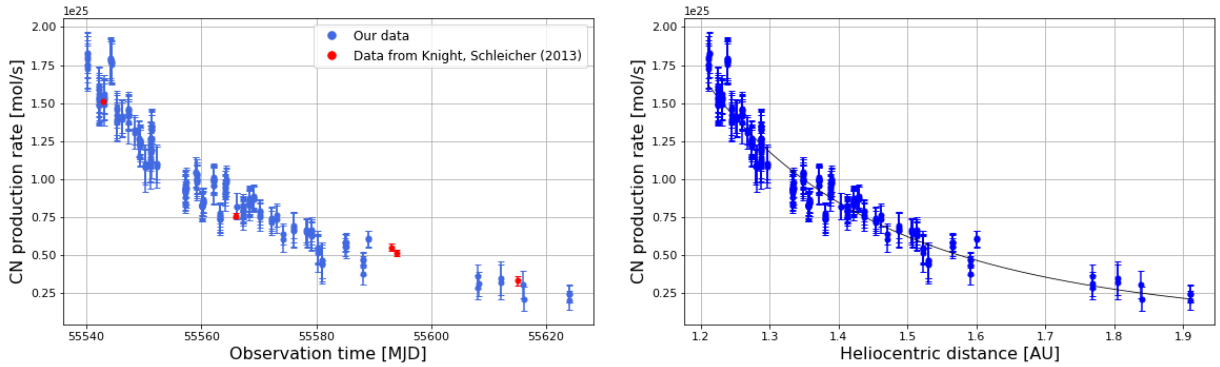

Figure 4.8. Evolution of the CN production rate in the coma of comet 103P as a function of time (left) and heliocentric distance (right) during perihelion passage in 2010. The black curve in the right-hand plot represents the power-law fit applied on the data points.

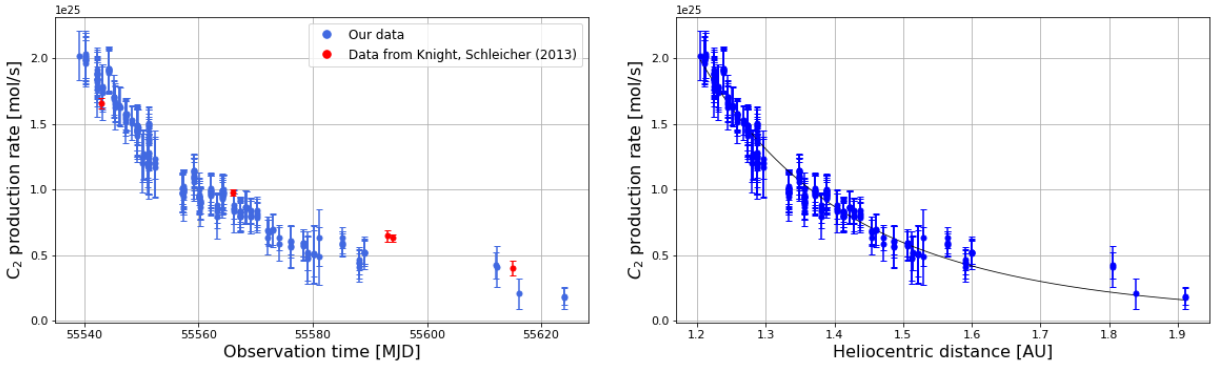

Figure 4.9. Evolution of the C_2 production rate in the coma of comet 103P as a function of time (left) and heliocentric distance (right) during perihelion passage in 2010. The black curve in the right-hand plot represents the power-law fit applied on the data points.

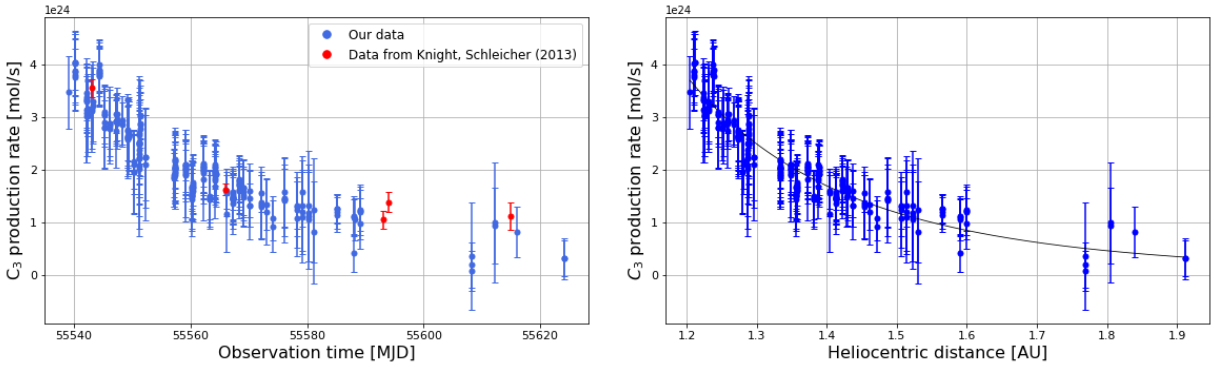

Figure 4.10. Evolution of the C_3 production rate in the coma of comet 103P as a function of time (left) and heliocentric distance (right) during perihelion passage in 2010. The black curve in the right-hand plot represents the power-law fit applied on the data points.

Table 4.2. Fitted power-law slopes derived from the heliocentric-distance dependence of gas production rates measured for the 2010 perihelion passage of comet 103P.

Species	r_h-dependence	Knight, Schleicher (2013)
OH	-4.00 ± 0.07	-3.99 ± 0.05
CN	-4.48 ± 0.09	-3.20 ± 0.10
C_2	-5.50 ± 0.08	-3.45 ± 0.09
C_3	-5.22 ± 0.13	-3.20 ± 0.13

The slopes derived from the C_2 and C_3 production rates are similar. They are slightly higher than the slope derived from the CN production rate, but lower than the one derived from the OH production rate. As compared to the values obtained by Knight, Schleicher (2013) (given in the table), our values are a bit steeper, except for OH. However, it is worth mentioning that our observations started in December 2010, that is more than a month after perihelion, contrarily to Knight

and Schleicher's complete data set that encompasses comet images taken during the passage of the comet at perihelion.

The gas OH, NH, CN, C_2, and C_3 production rates measured for the 2023 passage of 103P are given in the appendix in Table A.4. Figures 4.11 to 4.15 also show the evolution of these production rates as a function of time and heliocentric distance. Again, we fitted separately the data points before and after the peak of gas production with a power law. The fit curves can be seen in the above figures showing the variation of Q as a function of heliocentric distance, and the slopes we derived for each species are given in Table 4.3.

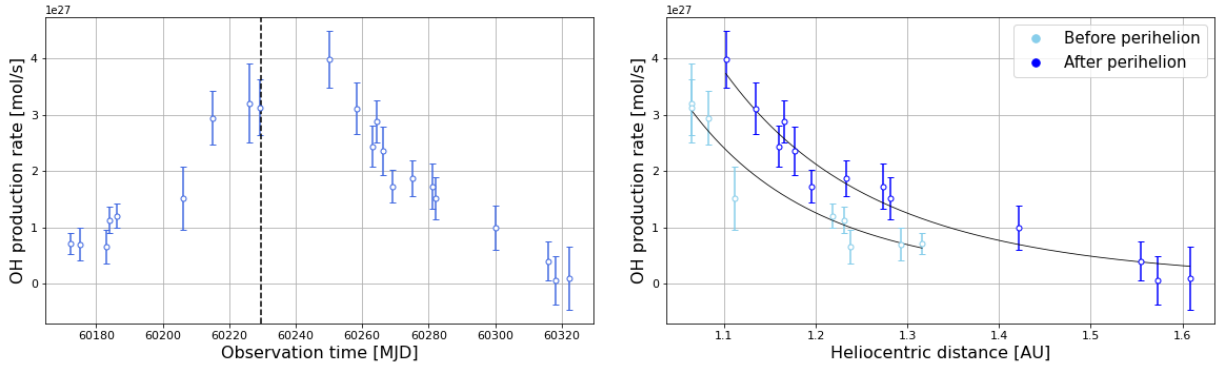

Figure 4.11. Evolution of the OH production rate in the coma of comet 103P as a function of time (left) and heliocentric distance (right) during perihelion passage in 2023. The dashed, black line in the left-hand plot represents the date of perihelion (October 12, 2023). The black curves in the right-hand plot represent the power-law fit applied on the pre-maximum and post-maximum data points. Solid and empty points stand for TS and TN data, respectively.

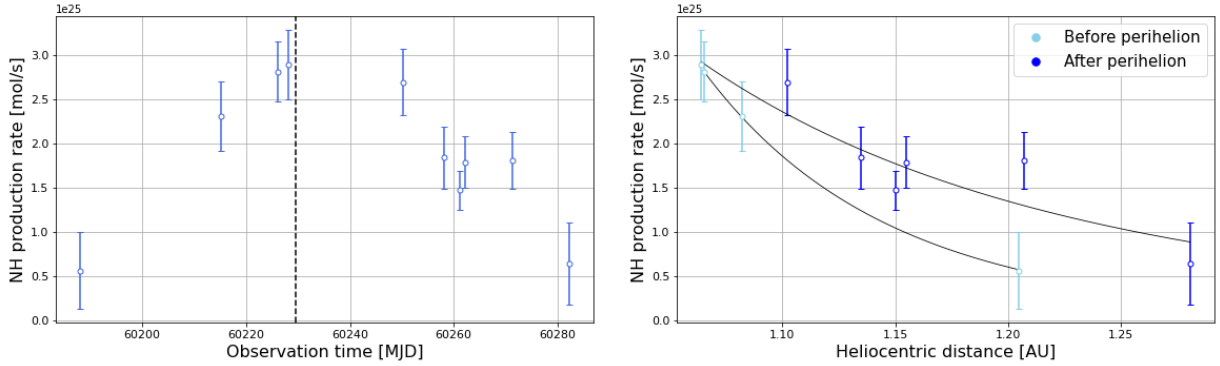

Figure 4.12. Evolution of the NH production rate in the coma of comet 103P as a function of time (left) and heliocentric distance (right) during perihelion passage in 2023. The dashed, black line in the left-hand plot represents the date of perihelion (October 12, 2023). The black curves in the right-hand plot represent the power-law fit applied on the pre-maximum and post-maximum data points. Solid and empty points stand for TS and TN data, respectively.

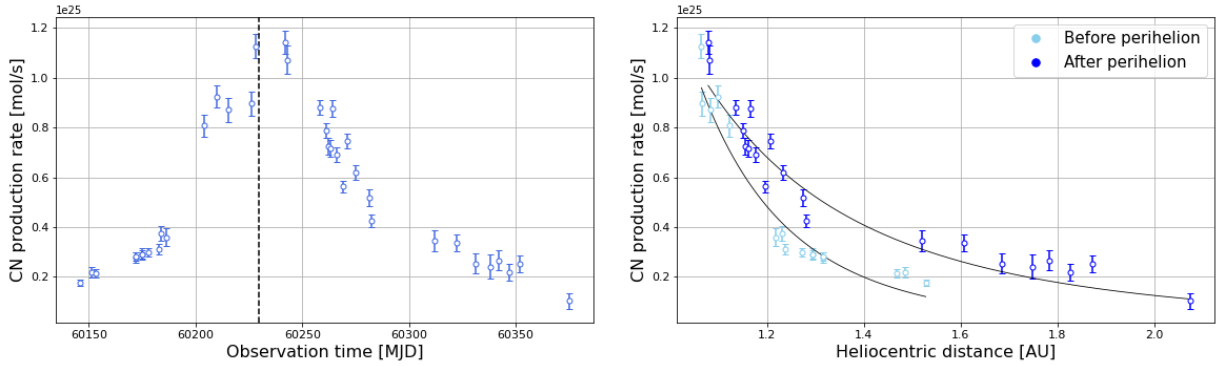

Figure 4.13. Evolution of the CN production rate in the coma of comet 103P as a function of time (left) and heliocentric distance (right) during perihelion passage in 2023. The dashed, black line in the left-hand plot represents the date of perihelion (October 12, 2023). The black curves in the right-hand plot represent the power-law fit applied on the pre-maximum and post-maximum data points. Solid and empty points stand for TS and TN data, respectively.

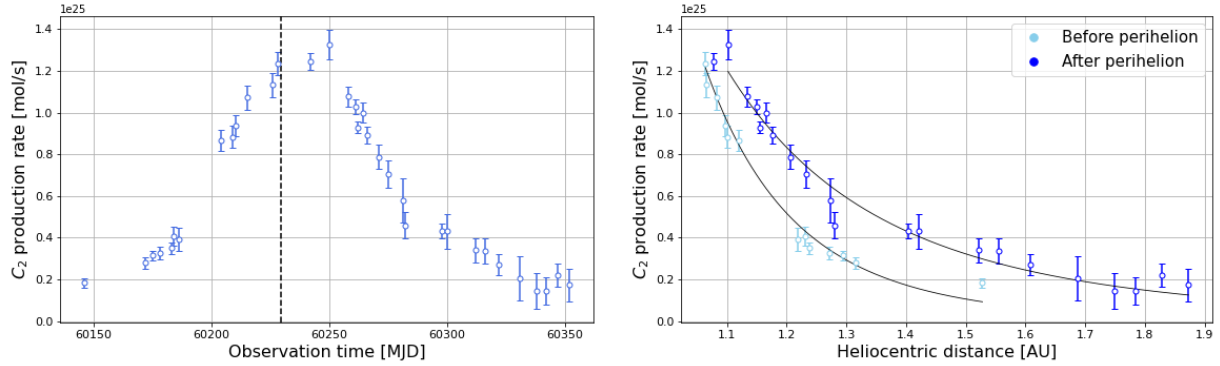

Figure 4.14. Evolution of the C_2 production rate in the coma of comet 103P as a function of time (left) and heliocentric distance (right) during perihelion passage in 2023. The dashed, black line in the left-hand plot represents the date of perihelion (October 12, 2023). The black curves in the right-hand plot represent the power-law fit applied on the pre-maximum and post-maximum data points. Solid and empty points stand for TS and TN data, respectively.

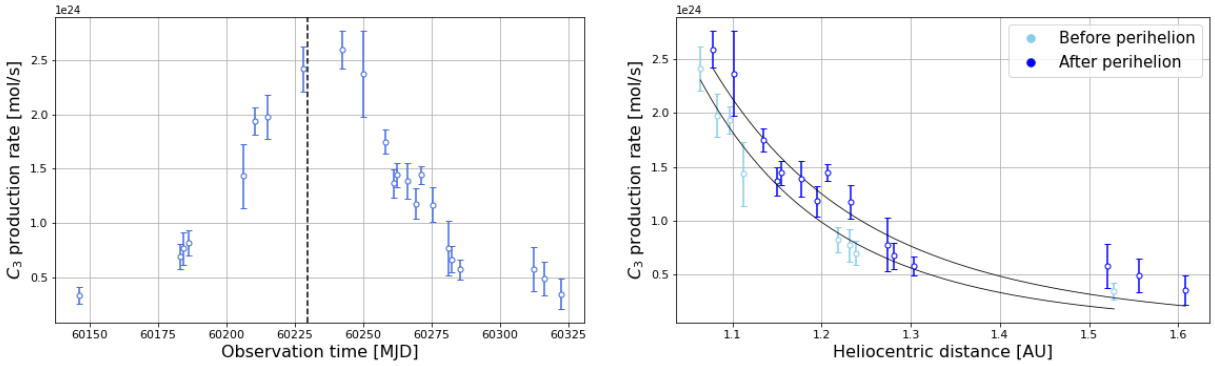

Figure 4.15. Evolution of the C_3 production rate in the coma of comet 103P as a function of time (left) and heliocentric distance (right) during perihelion passage in 2023. The dashed, black line in the left-hand plot represents the date of perihelion (October 12, 2023). The black curves in the right-hand plot represent the power-law fit applied on the pre-maximum and post-maximum data points. Solid and empty points stand for TS and TN data, respectively.

Table 4.3. Fitted power-law slopes derived from the heliocentric-distance dependence of gas production rates measured for the 2023 perihelion passage of comet 103P.

	r_h-dependence	
Species	Before Q maximum	After Q maximum
OH	7.48 ± 0.72	-6.62 ± 0.78
NH	12.93 ± 0.24	-6.43 ± 1.72
CN	5.73 ± 0.46	-3.31 ± 0.38
C_2	7.10 ± 0.43	-4.25 ± 0.25
C_3	7.08 ± 0.73	-6.16 ± 0.74

The C_2 and C_3 production rates undergo similar changes. They slowly increase during the pre-perihelion phase, and the computed power-law slopes are similar. According to our data, the peak of C_2 production is reached 21 days after perihelion, with a maximum value $Q = 1.33 \pm 0.07 \times 10^{25}$, while the peak of C_3 production is reached only 13 days after perihelion, with $Q = 2.59 \pm 0.17 \times 10^{24}$. Then, the production rates decrease until the end of our observations, although the decreasing slope is steeper for C_3 than for C_2. Regarding the CN curve, it behaves roughly like the C_2 and C_3 curves, except that the pre-maximum and post-maximum slopes are both lower The peak of CN production is reached at the same time as the peak of C_3 production, and the maximum Q values is of $1.14 \pm 0.05 \times 10^{25}$. The OH and NH curves do not contain enough data points to accurately determine the time of gas production peak, but we can still observe the same increasing and decreasing trends as for the other species.

Now that the results have been presented separately for the two passages of 103P, let's compare them. Figure 4.16 shows the changes in the production rates of OH, CN, C_2, and C_3 between 2010 and 2023.

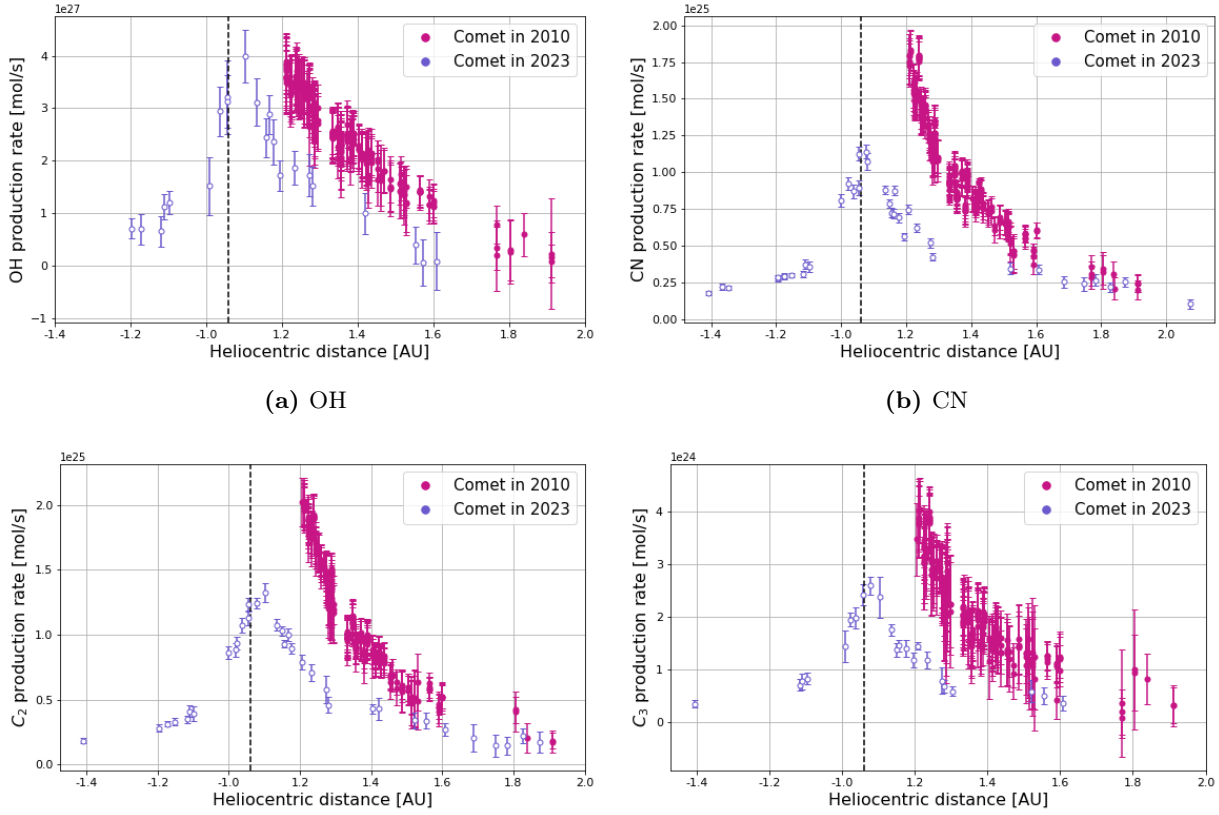

(a) OH **(b)** CN

(c) C_2 **(d)** C_3

Figure 4.16. Comparison of the gas production rates of Comet 103P between 2010 and 2023. The dashed, black line represents the heliocentric distance at perihelion (1.06 AU). Solid and empty points stand for TS and TN data, respectively.

The collected data do not allow any comparison during the pre-perihelion phase. However, in the post-perihelion phase, we unambiguously observe a higher production rate in 2010 as compared to 2023, even when considering the uncertainty ranges. This could indicate, on one hand, that the comet had lost a lot of materials between 2010 and 2023 through intense outgassing events during the activity periods of the comet. Let's remind that the comet also passed close to the Sun in 2017, although it could not be observed. On the other hand, this could simply indicate that the region of the comet that was facing the Sun during the perihelion passage in 2010 contained more volatile elements than the region that was facing the Sun during the second passage.

4.2.2 Production rate ratios and comet taxonomy

Jupiter-family comets can be divided into two categories based on their chemical composition: the typical ones and those displaying a depletion in species containing carbon chains (C_2 and C_3).

According to a criterion defined by A'Hearn et al. (1995), the depleted comets have a C_2-to-CN production rate ratio such that $\log[Q_{C_2}/Q_{CN}] < -0.18$, while the typical comets have a mean value of $\log[Q_{C_2}/Q_{CN}]$ around +0.06. This criterion has been establish following a seventeen-year observation campaign of a sample of 85 comets and an intensive study of their properties. Note also that it is based on cometary gas production rates that have been calculated using the Haser model, and is thus relevant in our case.

To determine the chemical class of 67P and 103P, the ratios of C_2 and CN production rates have been computed for the two comets. We then compared the ratio values obtained for the two perihelion passages of each of our comets, in order to evaluate if there is a difference from one passage to the other or not. The results of our analysis are presented in this section.

Comet 67P/Churyumov-Gerasimenko

The C_2-to-CN production rate ratios computed for 67P are given in the appendix in Table A.5, for the first and second perihelion passages. Please note that, in 2015, there were no nights when both C_2 and CN data were collected. Therefore, the values in the table are based on production rate values obtained with a 1-day interval between them. The ratio values have also been plotted as a function of the heliocentric distance of the comet. The result is shown in Figure 4.17. The ranges of ratio values obtained by A'Hearn et al. for their 85-comet sample are also represented as blue and red areas for the typical and carbon-depleted comets, respectively.

First of all, we can make use of the data obtained during the second passage to evaluate how the ratios vary with heliocentric distance. Indeed, we see that the ratios seem to follow a decreasing trend in the pre-perihelion phase, reach a minimum value close to the perihelion, and finally increase again in the post-perihelion phase. We can also see that, despite their variation as a function of the heliocentric distance of the comet, the data points remain localized above the red area of the graph (except the one measured on September 12/13, 2015). Therefore, we can directly conclude that, according to our results, 67P is a typical comet.

The classification of 67P as a typical comet has not always been supported. Indeed, A'Hearn et al. themselves have classified it as carbon-depleted, based on observations they performed during the 1982 perihelion passage (see A'Hearn et al. (1995)). The comet has also been classified as depleted by other authors. However, observations performed during more recent perihelion passages actually revealed opposite results. For example, the gas production rates measured by Opitom et al. (2017) through observations with TRAPPIST (same data set as ours), but also with the Very Large Telescope (VLT) and the William Herschel Telescope (WHT), during the 2015 perihelion passage, led to the classification of 67P as a typical comet. This result was also supported by other authors

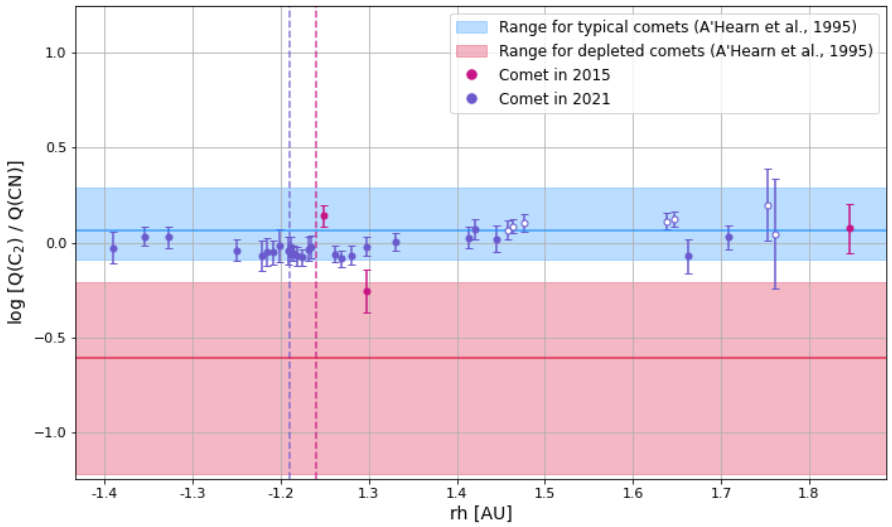

Figure 4.17. Evolution of the C_2-to-CN production rate ratios of comet 67P as a function of the heliocentric distance. The dashed, colored lines represent the heliocentric distances at perihelion for the first (1.24 AU) and second (1.21 AU) passages. Solid and empty points stand for TS and TN data, respectively. The blue area represents the range of ratio values ($-0.09 \longrightarrow 0.29$) obtained by A'Hearn et al. for typical comets, with the horizontal, blue line showing the mean value (0.06). The red area represents the range of ratio values ($-1.22 \longrightarrow -0.21$) obtained by A'Hearn et al. for depleted comets, with the horizontal, red line showing the mean value (-0.61).

(see for example Lara et al. (2011) for the 2009 passage of the comet). As a consequence, astronomers started to wonder if the chemical composition of comets could change over time, due to the activity periods they undergo at each time their orbit brings them close to the Sun. An evolution in the abundance in carbonated species might have effectively led to the change in classification of 67P from depleted to typical. Nonetheless, our data seem to show that, between 2015 and 2021, the gas production rate ratios of 67P have not evolved. They have remained in the same range. Actually, given the unprecedented levels of accuracy in comet observations reached with the TRAPPIST telescopes (thanks notably to the HB narrow-band filters) and the homogeneity of our survey (same telescopes and same methods for both passages), the results we obtained might slightly differ from the previous ones, leading to more relevant conclusions. Thus, it would be interesting to reconsider this hypothesis. Hopefully the observations of future passages of 67P would tell us more about that.

Comet 103P/Hartley 2

The ratio values obtained for the first and second passages of 103P are given in the appendix in Table A.6. They are also represented as a function of the heliocentric distance of the comet in Figure 4.18, along with the range of values obtained by A'Hearn et al. for typical and carbon-depleted comets.

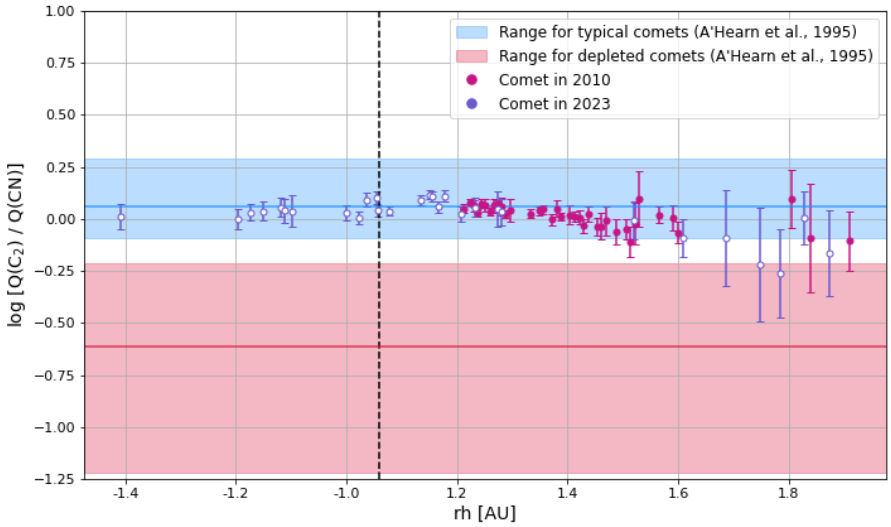

Figure 4.18. Evolution of the C_2-to-CN production rate ratios of comet 103P as a function of the heliocentric distance. The dashed, black line represents the heliocentric distance at perihelion (1.06 AU). Solid and empty points stand for TS and TN data, respectively. The blue area represents the range of ratio values ($-0.09 \longrightarrow 0.29$) obtained for typical comets by A'Hearn et al., with the horizontal, blue line showing the mean value obtained (0.06). The red area represents the range of ratio values ($-1.22 \longrightarrow -0.21$) obtained by A'Hearn for depleted comets, with the horizontal, red line showing the mean value (-0.61).

Contrarily to 67P, the C_2-to-CN production rate ratios of 103P seem to increase during the pre-perihelion phase of the comet, and decrease in the post-perihelion phase. Within the heliocentric-distance range from -1.4 to 1.4 AU, our values are consistent with those obtained by A'Hearn et al. for typical comets. 103P can thus be classified as typical in terms of abundance in carbon-chain species, and this result is in accord with the classification already established by A'Hearn et al. (1995). Moreover, the ratios measured in 2010 are similar to those measured in 2023, which reinforces our reasoning about the fact that production rate ratios might not change over time.

4.2.3 Water production rates

Water is the main chemical component of cometary ices. It is also the main parent molecule of the OH daughter molecule, which is the most abundant species in comae when comets are located within a distance of 3 AU from the Sun. For that reason, Cochran, Schleicher (1993) and Schleicher, A'Hearn (1988) have introduced an empirical formula allowing to derive the H_2O production rate of comets based on their observed OH production rate. It has been established on the basis of a comparison of some chemical properties of the two molecules, such as their mean lifetime and branching ratio (i.e., the probability that a given H_2O molecule will photodissociate into an OH molecule). Thus, the cometary H_2O production rate, Q_{H_2O}, can be derived from the OH production rate, Q_{OH}, via the relation:

$$Q_{H_2O} = 1.361\ r_h^{-0.5}\ Q_{OH}, \tag{4.14}$$

where r_h is the heliocentric distance of the comet.

We used this straightforward relation to compute the water production rates of 67P and 103P from the OH production rates computed previously in this work. The results are presented in this section.

Comet 67P/Churyumov-Gerasimenko

The evolution of the H_2O production rate computed for the 2021 passage of 67P is shown in Figure 4.19 as a function of time and heliocentric distance. This species behaves similarly to the others, with a production rate peak observed approximately 20 days after perihelion. The values increase to $7.61 \pm 2.52 \times 10^{27}$ mol/s, which corresponds approximately to 240 kg of water released per second. This is slightly higher than the maximum production rate observed for OH ($6.22 \pm 2.06 \times 10^{28}$ mol/s). Then, they slowly decrease until the end of our observations.

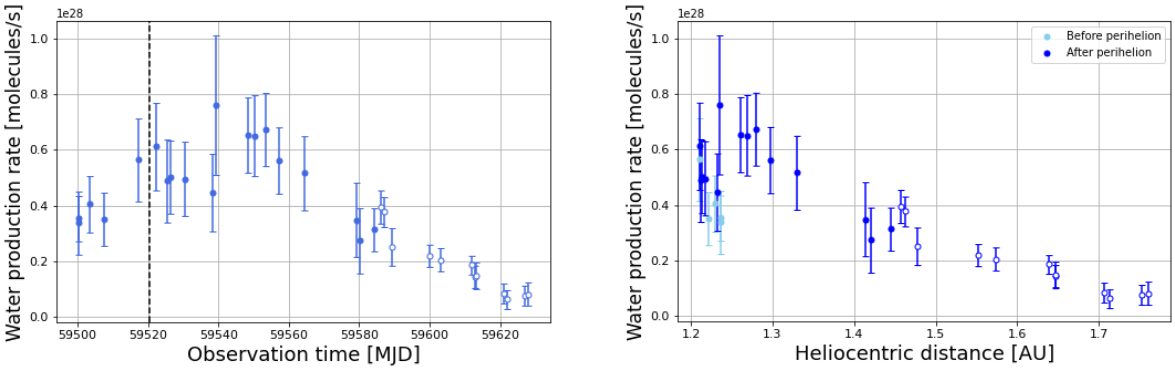

Figure 4.19. Evolution of the water production rate as a function of time (left) and heliocentric distance (right) during the 2021 perihelion passage of comet 67P. The dashed, black line in the left-hand plot represents the date of perihelion (November 2, 2021). Solid and empty points stand for TS and TN data, respectively.

Comet 103P/Hartley 2

The evolution of the H_2O production rate of 103P, computed from the OH production rate measured during the 2010 passage, is represented in Figure 4.20. As for OH, we can not analyze the curve behavior at the time of perihelion. However, among our data set, the maximum production rate observed (at the beginning of the observations) is of $4.47 \pm 0.75 \times 10^{27}$ mol/s, corresponding to ~ 134 kg of water molecules released per second. This is slightly higher than the OH production rate measured at the same date ($3.61 \pm 0.60 \times 10^{27}$ mol/s).

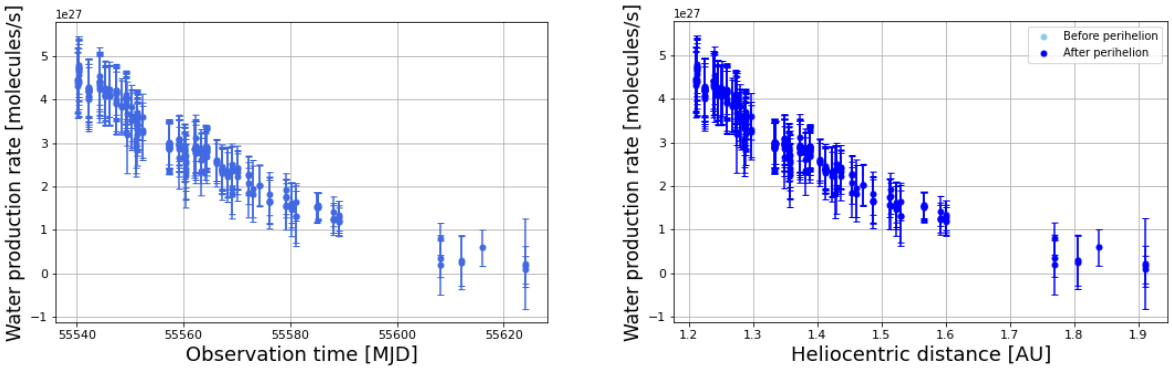

Figure 4.20. Evolution of the water production rate as a function of time (left) and heliocentric distance (right) during the 2010 perihelion passage of comet 103P.

Finally, the evolution of the H_2O production rate computed for the second passage of the comet is shown in Figure 4.21. As there was a lack of OH data especially at the time of perihelion, we can not accurately determine the position of the production rate peak, but it should occur between 10 and 20 days after perihelion. The higher obtained value is of $5.17 \pm 0.65 \times 10^{27}$ mol/s (≈ 155 kg/s), but it might be even larger at the exact time of production rate peak.

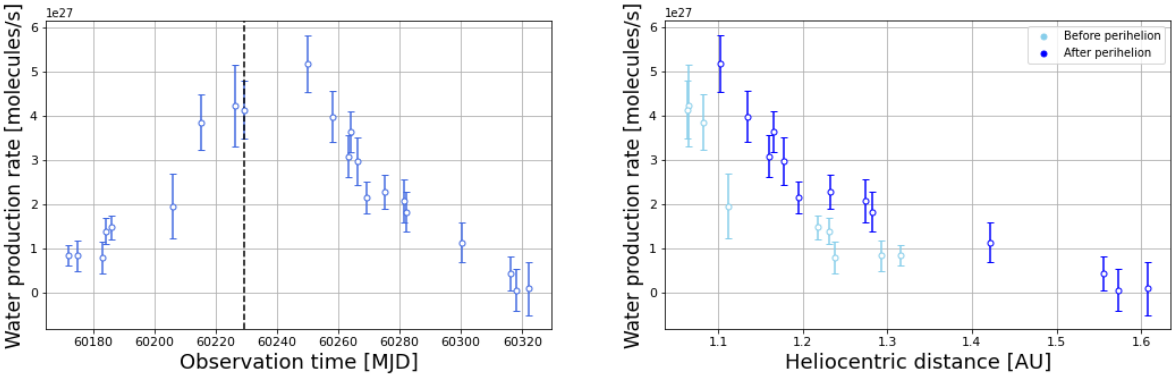

Figure 4.21. Evolution of the water production rate as a function of time (left) and heliocentric distance (right) during the 2023 perihelion passage of comet 103P. The dashed, black line in the left-hand plot represents the date of perihelion (October 12, 2023).

Chapter 5

Dust activity

When a comet is active, some dust particles are driven outside the nucleus due to the escaping gas and end up in the coma. This chapter focuses on an observation-based estimation of the dust production rates of our target comets. This can be performed by using the light fluxes collected with TRAPPIST's narrow-band gas filters, suited for solar light reflected by cometary dust.

The quantification of dust activity is realized through the computation of a parameter known as "Afrho". This parameter is described at the beginning of this chapter. Then, the results are presented and corrected for the so-called phase angle effect, that significantly affects our values. Finally, in order to evaluate the dust richness of the comets, we calculated dust-to-gas ratios by using the computed dust activity proxies, as well as the CN production rates given in the previous chapter.

5.1 The Afrho parameter

The quantity Afrho is used in order to estimate the dust outgassing of comets. This parameter was first introduced in 1984 by Michael A'Hearn, in the framework of its study about the long-period comet C/1980 E1, also known as Comet Bowell (A'Hearn et al., 1984).

5.1.1 Definition of the parameter

The Afrho parameter is so-called because it corresponds to the product of the three following quantities:

- $A(\theta)$, the Bond albedo of cometary dust grains (i.e., the fraction of incident solar light that is reflected by dust grains) at the phase angle θ (i.e., the Sun-comet-observer angle) of the observations;

- f, the filling factor of dust grains in the field of view, i.e., the total area filled with dust grains in the field of view divided by the surface of the field of view, $\pi\rho^2$ (see Figure 5.1);
- ρ, the radius of the coma inside which the dust activity is estimated.

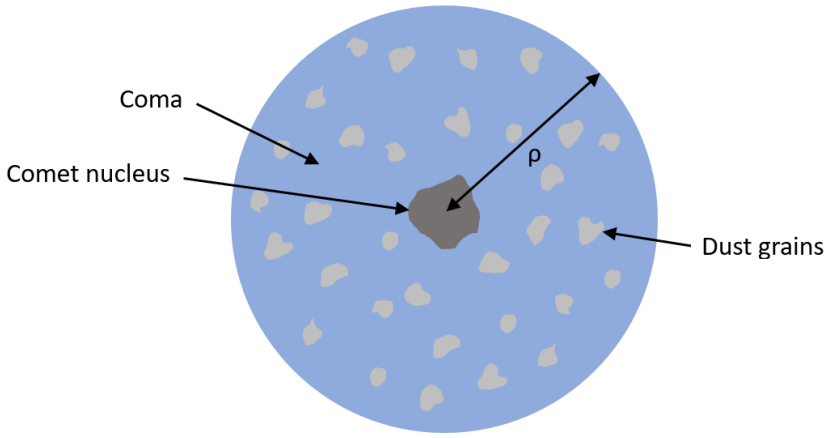

Figure 5.1. Illustration of the filling factor of dust grains in a cometary coma of radius ρ.

This proxy of the cometary dust activity is then defined as

$$A(\theta)f\rho = \frac{(2\Delta r_h)^2}{\rho}\frac{F_{comet}}{F_{sun}}. \tag{5.1}$$

In this expression, Δ and r_h are respectively the geocentric distance (in cm) and the heliocentric distance (in AU) of the comet. F_{comet} is the solar flux reflected in the field of view by the dust grains present within the nucleocentric sphere of radius ρ, and F_{sun} is the solar flux measured at a distance of 1 AU. These fluxes depend on the filter used and are expressed in erg cm^{-2} s^{-1} Å^{-1}. The quantity $A(\theta)f\rho$ is thus given in cm.

5.1.2 The phase angle effect

Once the $A(\theta)f\rho$ values are obtained, it is necessary to apply a correction so that they can be compared to those obtained for other comets, or in the case of this work, during other perihelion passages. This correction is linked to the fact that the albedo A of cometary dust grains depends on the phase angle θ. Indeed, the significance of the solar light scattering by dust, as seen from the surface of the Earth, depends on this phase angle. In particular, the scattering is much more efficient if θ is large. This is known as the phase angle effect, and a correction of the $A(\theta)f\rho$ values for this effect is needed. The correction simply consists in a normalization of the obtained values by a dust phase function (see Section 5.1.3).

5.1.3 Computation method

The Afrho parameter was computed numerically by using Equation 5.1. In practice, for each image obtained with the BC, GC, and RC dust filters, as well as with the R broad-band filter, an $A(\theta)f\rho$ value was computed for each circle of pixels around the comet optocenter, as for the radial brightness profiles. In this way, we obtained an Afrho profile representing the variation of the parameter as a function of the nucleocentric distance ρ. Then, we decided to interpolate the profile to get the $A(\theta)f\rho$ value at a nucleocentric distance of 10,000 km (see the dashed, blue line in Figure 3.4). Theoretically, the choice of the distance ρ for the computation of the Afrho parameter is not supposed to have an impact on the results. Indeed, if a simple radial-outflow model (i.e., a model taking into account an isotropic coma with grains evolving at a constant speed) is considered, then the $A(\theta)f\rho$ values should be independent of the nucleocentric distance. In particular, this is true if the radial luminosity profile measured in the filter used for the computation evolves as $1/\rho$. Let's notice that, in practice, the evolution of $A(\theta)f\rho$ as a function of ρ is not exactly a constant function. It rather displays a slight decrease for increasing values of ρ (see A'Hearn et al. (1984)), due to the fact that radial profiles do not perfectly follow a $1/\rho$ curve. However, this decrease being very low, it is considered negligible. This result is useful notably when it comes to compare some values obtained with telescopes of different aperture sizes.

The $A(\theta)f\rho$ values interpolated at 10,000 km were then normalized to correct for the phase angle effect. For the correction, a composite dust phase function defined by D. Schleider was used[1]. This phase function consists in a combination of two previously defined functions: the Halley curve (which is more suited for small phase angles) and the Marcus curve (more suited for large phase angles). A description of these two individual curves is given on the mentioned website. We chose to normalize the $A(\theta)f\rho$ values at a phase angle θ of 0 degree (corresponding to a back-scattering of the light). The 0°-normalized function used is represented in Figure 5.2.

Finally, we gathered all the phase-angle-corrected values of dust activity proxy collected during the perihelion passages of both 67P and 103P, and we plotted them in order to follow their evolution as a function of time and heliocentric distance.

[1]Composite Dust Phase Function for Comets: `https://asteroid.lowell.edu/comet/dustphase.html`

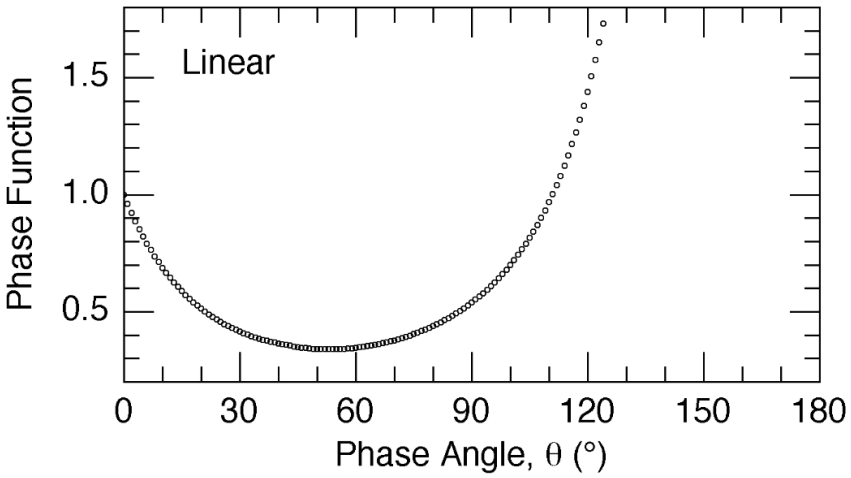

Figure 5.2. Zero-degree-normalized composite dust phase function defined by D. Schleider and used in this work to correct the obtained $A(\theta)f\rho$ values for the phase angle effect.

5.2 Results and discussion

This section presents the results of our computation of the Afrho parameter for the two analyzed passages of comets 67P and 103P. The evolution of dust activities as a function of time and heliocentric distance is discussed in the first part. Then, we give the dust-to-gas ratios of the comets, calculated on the basis of the CN production rates, with the aim of characterizing their dust richness and, eventually, highlighting a change in this richness from one passage to the other.

5.2.1 The dust activity

Comet 67P/Churyumov-Gerasimenko

The phase-angle-uncorrected and corrected $Af\rho$ values computed for the first passage of 67P are given in the appendix, in Table B.1, along with the phase angle of the comet measured at the time of the observations. As few values were obtained with the dust filters, we could not follow their evolution during the perihelion passage. However, it was still possible using the R data. The evolution of $Af\rho$ (corrected for the phase angle effect) during the whole passage of the comet close to the Sun is shown in Figure 5.3, as a function of time and heliocentric distance. The curve representing the r_h dependence of the dust activity has been separated into two parts: before and after the peak. The two parts have fitted separately in order to retrieve the power-law ($A(0)f\rho \propto r_h^n$) slopes, n. The fit result has been overplotted on the curve and can thus be seen in Figure 5.3. The derived slopes are given in Table 5.1.

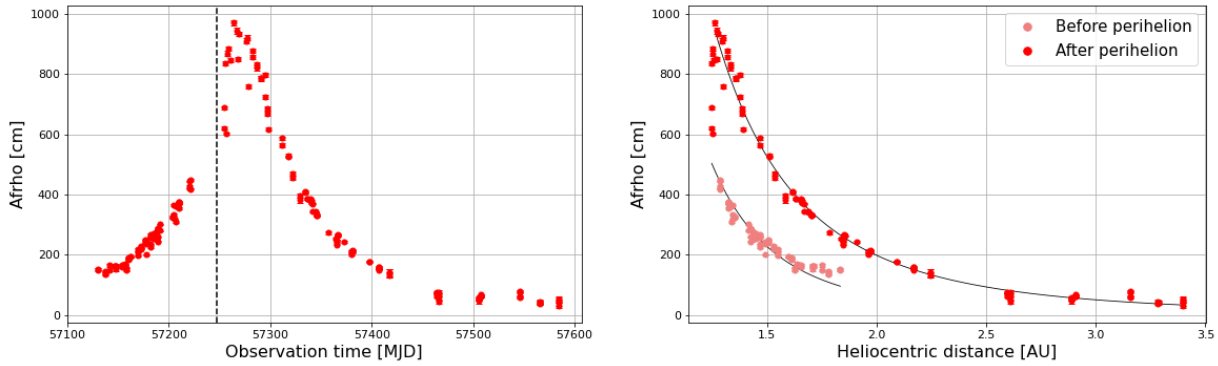

Figure 5.3. Evolution of the Afrho parameter as a function of time (left) and heliocentric distance (right) measured with the R filter for the 2015 perihelion passage of comet 67P. The values are corrected for the phase angle effect. The dashed, black line in the left-hand plot represents the date of perihelion (August 13, 2015). The black curves in the right-hand plot represent the fit applied on the pre-maximum and post-maximum data points.

Table 5.1. Fitted power-law slopes derived from the heliocentric-distance dependence of the dust activity measured for the 2015 perihelion passage of comet 67P.

	r_h-dependence	
Filter	Before $A(0)f\rho$ maximum	After $A(0)f\rho$ maximum
R	4.32 ± 0.22	-3.40 ± 0.04

The seasonal effect of the comet and the resulting asymmetry with respect to perihelion are clearly detectable with these curves. We observe a peak of dust activity 17 days after perihelion, with $A(0)f\rho = 971.14 \pm 23.66$ cm.

Much more results were obtained with the dust filters during the second passage of the comet. They are listed in the appendix in Table B.3, with the phase angles measured for each observation night. The values obtained with the R filter are also given. Moreover, the phase-angle-corrected $A(0)f\rho$ values computed with the BC, GC, and R filters are represented respectively in Figures 5.4, 5.5, and 5.13 as a function of time and heliocentric distance. Again, the curves showing the variation of $A(0)f\rho$ as a function of heliocentric distance have been fitted to retrieve the power-law slopes before and after the peak of dust activity. The fit result can be seen in the right-hand plots of the figures, and the derived slopes are given in Table 5.2.

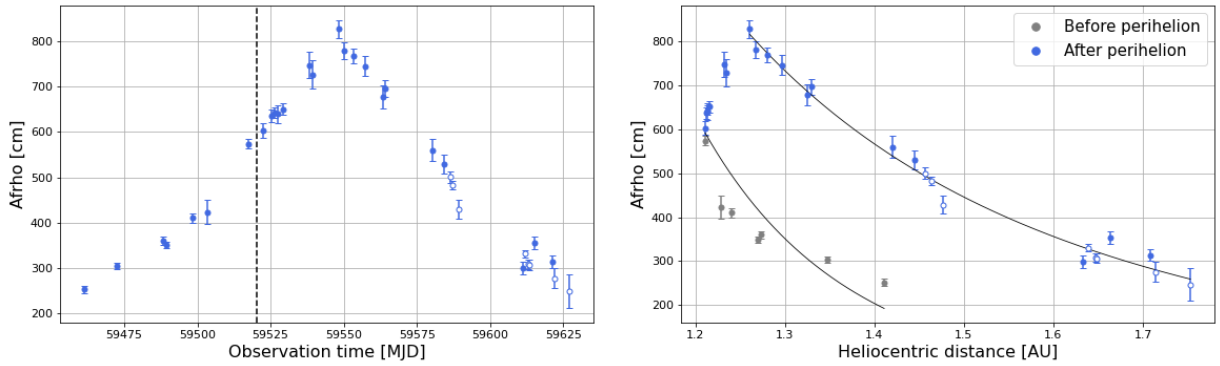

Figure 5.4. Evolution of the Afrho parameter as a function of time (left) and heliocentric distance (right) measured with the BC filter for the 2021 perihelion passage of comet 67P. The values are corrected for the phase angle effect. The dashed, black line in the left-hand plot represents the date of perihelion (November 2, 2021). The black curves in the right-hand plot represent the fit applied on the pre-maximum and post-maximum data points. Solid and empty points stand for TS and TN data, respectively.

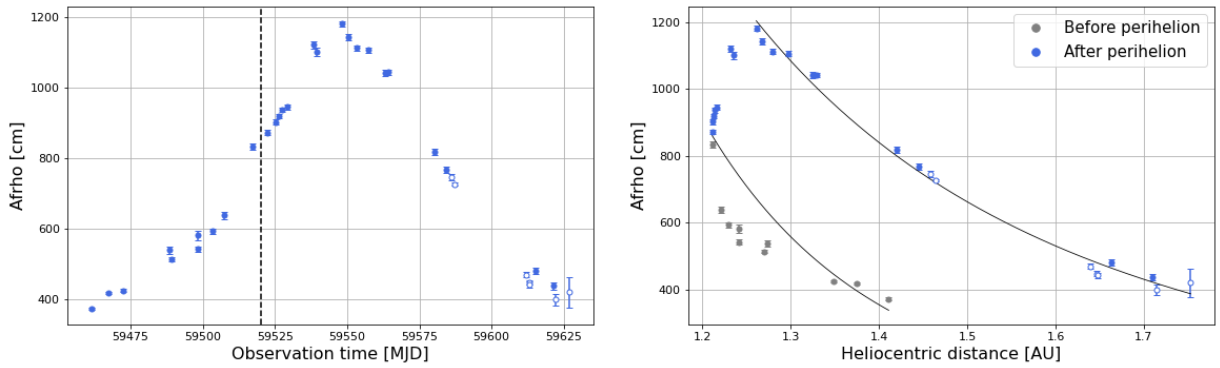

Figure 5.5. Evolution of the Afrho parameter as a function of time (left) and heliocentric distance (right) measured with the RC filter for the 2021 perihelion passage of comet 67P. The values are corrected for the phase angle effect. The dashed, black line in the left-hand plot represents the date of perihelion (November 2, 2021). The black curves in the right-hand plot represent the fit applied on the pre-maximum and post-maximum data points. Solid and empty points stand for TS and TN data, respectively.

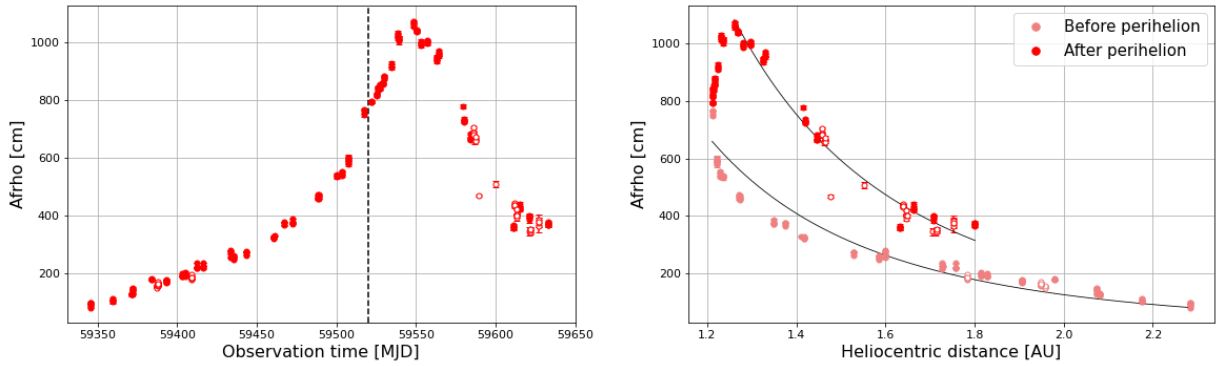

Figure 5.6. Evolution of the Afrho parameter as a function of time (left) and heliocentric distance (right) measured with the R filter for the 2021 perihelion passage of comet 67P. The values are corrected for the phase angle effect. The dashed, black line in the left-hand plot represents the date of perihelion (November 2, 2021). The black curves in the right-hand plot represent the fit applied on the pre-maximum and post-maximum data points. Solid and empty points stand for TS and TN data, respectively.

Table 5.2. Fitted power-law slopes derived from the heliocentric-distance dependence of the dust activity measured for the 2021 perihelion passage of comet 67P.

	r_h-dependence	
Filter	Before $A(0)f\rho$ maximum	After $A(0)f\rho$ maximum
BC	7.34 ± 1.18	-3.48 ± 0.09
RC	6.11 ± 0.81	-3.44 ± 0.09
R	3.29 ± 0.12	-3.46 ± 0.06

Whatever the filter used, the measured dust activity evolves the same. We observe a slow increase in the curves during the pre-perihelion phase, which continues during several weeks after the passage at perihelion. The maximum activity is detected 28 days after perihelion. At that date, we measured $A(0)f\rho$ values of 827.93 ± 57.71 cm in the blue continuum, 1181.36 ± 21.82 cm in the red continuum, and 1072.21 ± 12.99 cm with the R filter. Then, all three curves decrease until the end of our observations. Regarding the power-law slopes, giving the dependence of the dust activity on the heliocentric distance before and after the peak of dust activity, we measure steeper slopes before the peak than after the peak with the dust filters. However, this is not the case with the R filter. The slopes before and after the peak are indeed similar.

With the aim of comparing the dust activity measured with the different filters between 2015 and 2021, we plotted together our results presented above as a function of the heliocentric distance of the comet. The resulting plots are shown in Figure 5.7, and we observe a higher dust activity intensity during the 2021 passage than during the 2015 passage.

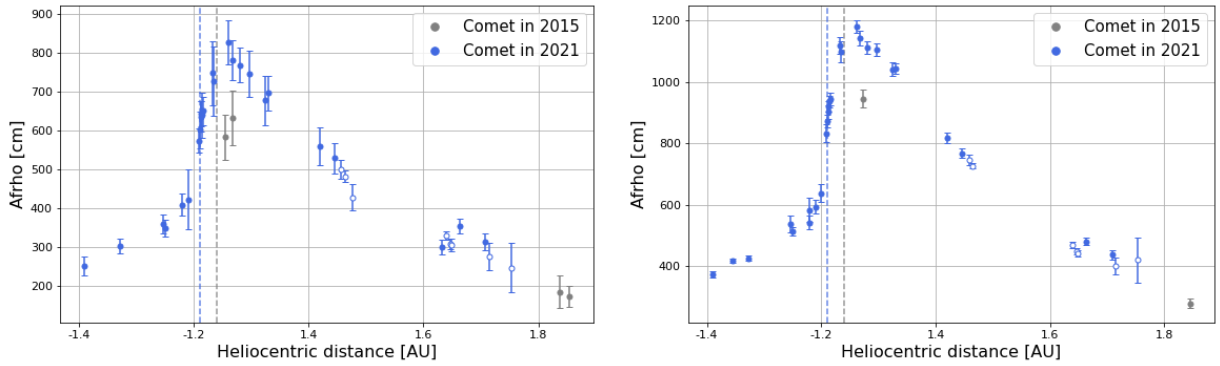

(a) BC filter

(b) RC filter

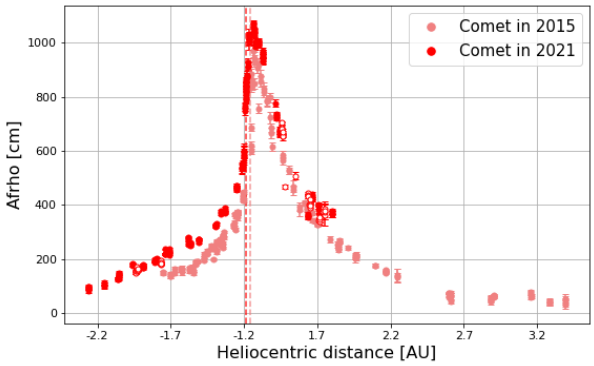

(c) R filter

Figure 5.7. Comparison of the dust activity of comet 67P between 2015 and 2021. The dashed lines represent the heliocentric distances at perihelion (1.24 AU in 2015 and 1.21 AU in 2021) in respective colors. Solid and empty points stand for TS and TN data, respectively.

Comet 103P/Hartley 2

Regarding the 2010 passage of 103P, a lot of GC images have been collected over the whole observation period. Some BC images were also available, but the observations with this filter only started at mid-January 2011. The $Af\rho$ values that we measured on the basis of all these images are listed in the appendix in Table B.5, both for the phase angle of the observations and for a phase angle $\theta = 0°$. The variation of these values as a function of time and heliocentric distance is also shown in Figures 5.8 and 5.9, respectively for the blue continuum and the green continuum. We can only observe in these curves the post-perihelion decrease in the Afrho parameter, as the heliocentric distance increases. The data have also been fitted with a power law. The fit result is shown in the figures, and the derived slopes, giving the heliocentric-distance dependence of the dust activity, are listed in Table 5.3. Unfortunately, although the data collected with the R filter were abundant for this passage, the Afrho parameter could not be computed simply because, at the time of the observations, this filter had another name (Rc) and this was not taken into account in the program

used for the calculations.

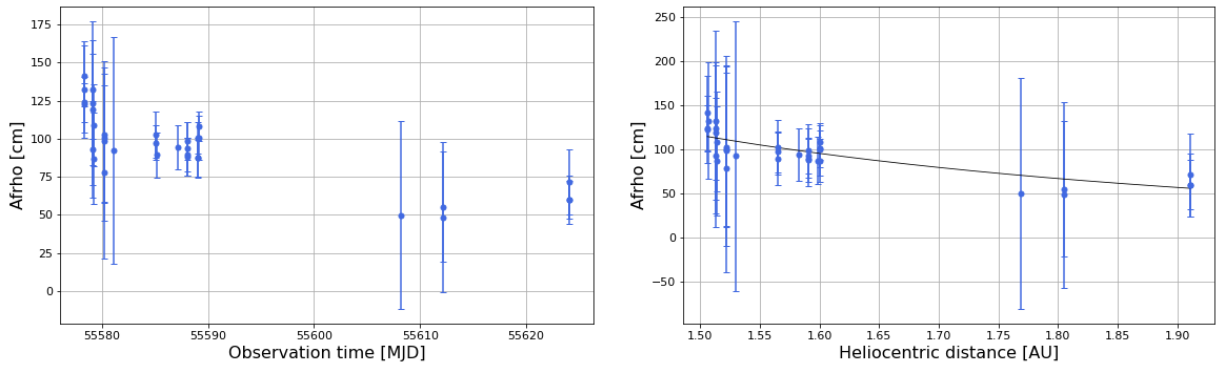

Figure 5.8. Evolution of the Afrho parameter as a function of time (left) and heliocentric distance (right) measured with the BC filter for the 2010 perihelion passage of comet 103P. The values are corrected for the phase angle effect. The black curve in the right-hand plot represents the fit applied on data points.

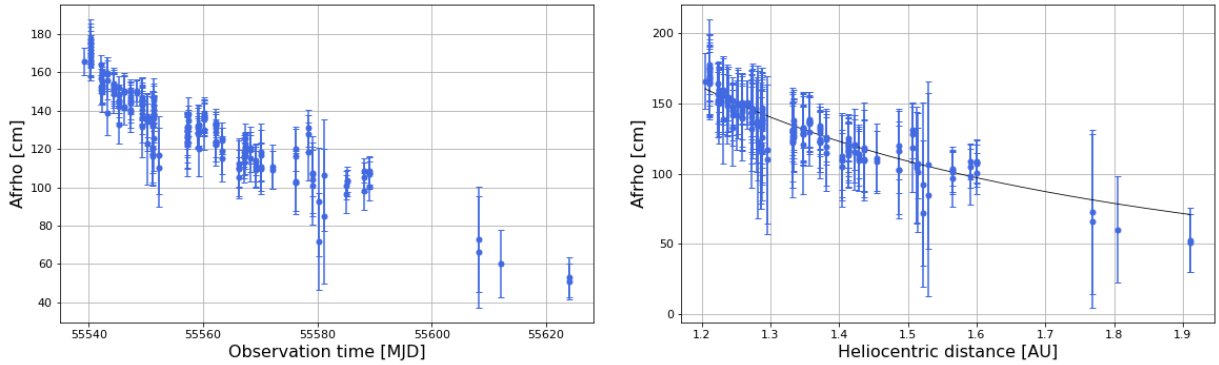

Figure 5.9. Evolution of the Afrho parameter as a function of time (left) and heliocentric distance (right) measured with the GC filter for the 2010 perihelion passage of comet 103P. The values are corrected for the phase angle effect. The black curve in the right-hand plot represents the fit applied on data points.

Table 5.3. Fitted power-law slopes derived from the heliocentric-distance dependence of the dust activity measured for the 2010 perihelion passage of comet 103P.

Filter	r_h-dependence
BC	-2.97 ± 0.40
GC	-1.82 ± 0.05

For the second passage of the comet, lots of images have been collected with the R, BC, and RC filters, and some GC images were also available. The uncorrected and corrected $Af\rho$ values computed on the basis of these images are given in the appendix in Table B.6, and the corrected values have been plotted as a function of time and heliocentric distance. The results are presented

in Figures 5.10, 5.11, and 5.12, respectively for the BC, GC, RC, and R filters. Again, we applied a power-law fit on the data. The retrieved slopes are given in Table 5.4.

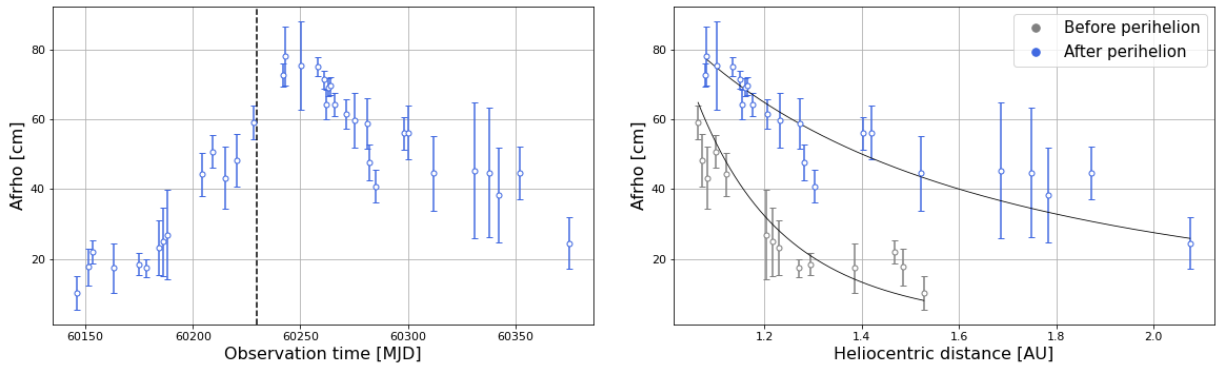

Figure 5.10. Evolution of the Afrho parameter as a function of time (left) and heliocentric distance (right) measured with the BC filter for the 2023 perihelion passage of comet 103P. The values are corrected for the phase angle effect. The dashed, black line in the left-hand plot represents the date of perihelion (October 12, 2023). The black curves in the right-hand plot represent the fit applied on the pre-maximum and post-maximum data points. Solid and empty points stand for TS and TN data, respectively.

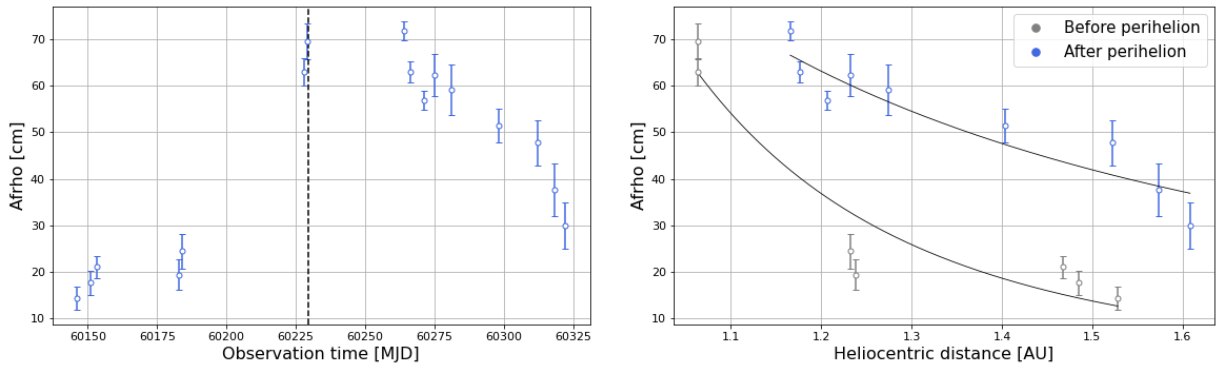

Figure 5.11. Evolution of the Afrho parameter as a function of time (left) and heliocentric distance (right) measured with the GC filter for the 2023 perihelion passage of comet 103P. The values are corrected for the phase angle effect. The dashed, black line in the left-hand plot represents the date of perihelion (October 12, 2023). The black curves in the right-hand plot represent the fit applied on the pre-maximum and post-maximum data points. Solid and empty points stand for TS and TN data, respectively.

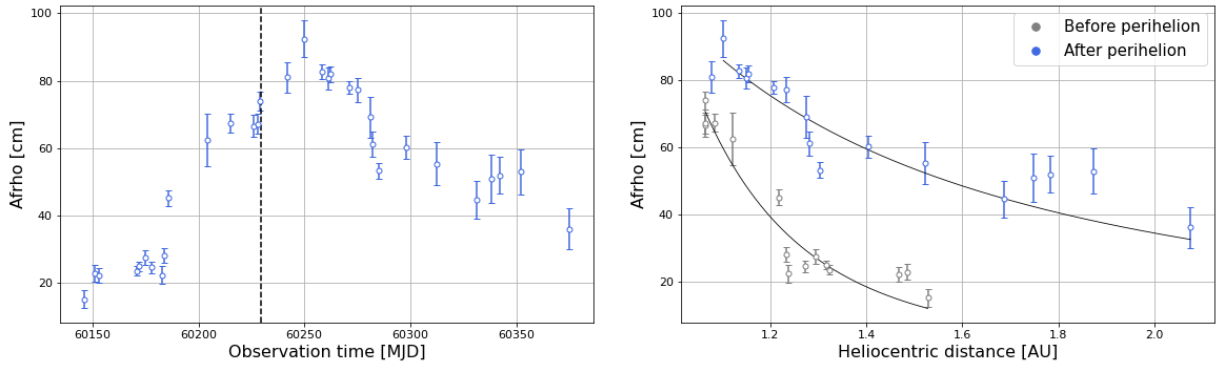

Figure 5.12. Evolution of the Afrho parameter as a function of time (left) and heliocentric distance (right) measured with the RC filter for the 2023 perihelion passage of comet 103P. The values are corrected for the phase angle effect. The dashed, black line in the left-hand plot represents the date of perihelion (October 12, 2023). The black curves in the right-hand plot represent the fit applied on the pre-maximum and post-maximum data points. Solid and empty points stand for TS and TN data, respectively.

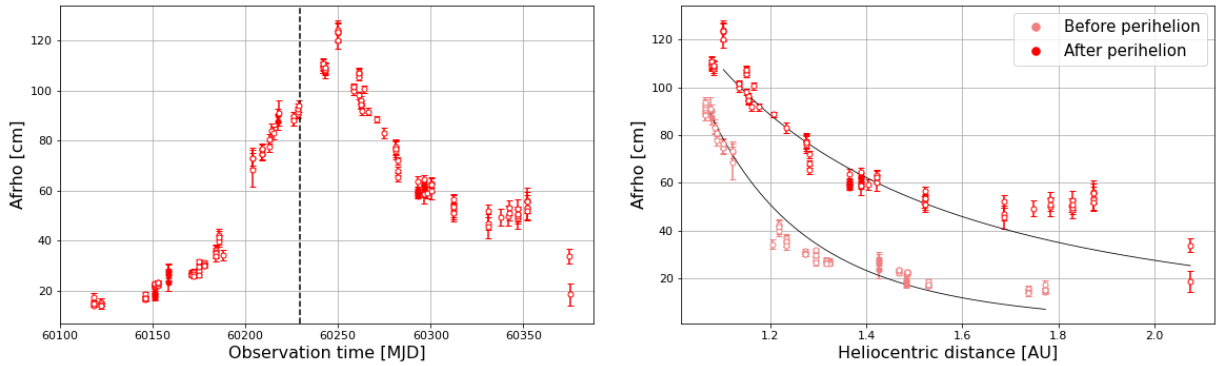

Figure 5.13. Evolution of the Afrho parameter as a function of time (left) and heliocentric distance (right) measured with the R filter for the 2023 perihelion passage of comet 103P. The values are corrected for the phase angle effect. The dashed, black line in the left-hand plot represents the date of perihelion (October 12, 2023). The black curves in the right-hand plot represent the fit applied on the pre-maximum and post-maximum data points. Solid and empty points stand for TS and TN data, respectively.

Table 5.4. Fitted power-law slopes derived from the heliocentric-distance dependence of the dust activity measured for the 2010 perihelion passage of comet 103P.

	r_h-dependence	
Filter	Before $A(0)f\rho$ maximum	After $A(0)f\rho$ maximum
BC	5.76 ± 0.84	-1.68 ± 0.26
GC	4.41 ± 0.75	-1.83 ± 0.41
RC	4.89 ± 0.41	-1.53 ± 0.24
R	5.08 ± 0.18	-2.29 ± 0.11

The evolution of the Afrho parameter computed for 103P can be characterized using notably the BC and RC data, along with the R data. We observe an increase in the dust activity of 103P during the pre-perihelion phase, from the beginning of our observations to the peak, that is measured 14 days after perihelion with the BC filter, and 21 days after perihelion with the RC and R filters. Then, the curves start decreasing slowly. The maximum Afrho parameter reached at the peak of activity is of 78.20 ± 23.45 cm in the blue continuum, 92.46 ± 15.72 cm in the red continuum, and 124.31 ± 11.16 cm in the R filter. Let's note that these values are much lower than those measured at the peak of activity for 67P, which indicates that 103P is a relatively dust-poor comet.

Finally, we have plotted together the corrected BC and GC data obtained for the first and the second passages of the comet in order to compare them. The result is shown in Figure 5.14. Within the r_h range from 1.2 to 1.9 AU, we detect higher $Af\rho$ values for the 2010 passage than for the 2023 passage, in both continua. A possible explanation for this result would be a change in the comet dust activity, because of an important loss of dust particles that the comet might have undergone when it passed close to the Sun in 2010, but also in 2017 when it was not observable.

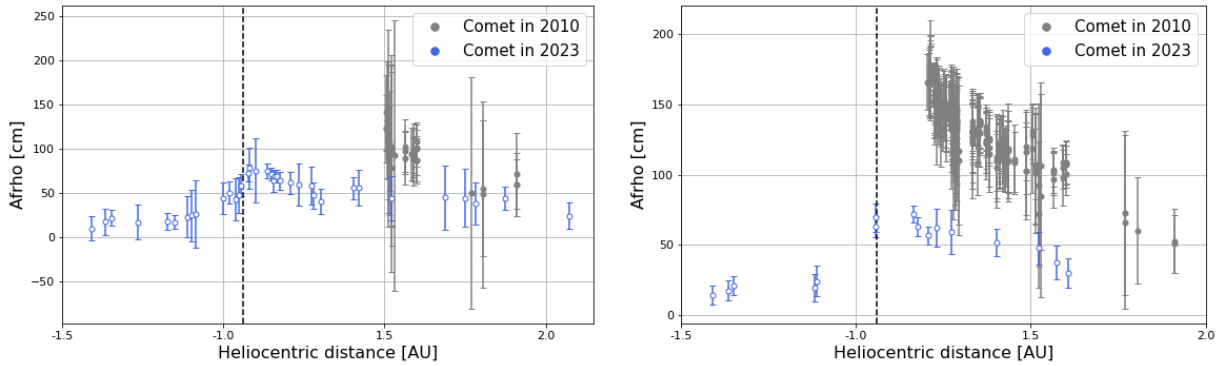

(a) BC filter **(b)** GC filter

Figure 5.14. Comparison of the dust activity of comet 103P between 2010 and 2023. The dashed, black line represents the heliocentric distance at perihelion (1.06 AU). Solid and empty points stand for TS and TN data, respectively.

5.2.2 Dust-to-gas ratios

In the previous chapter, the gas activity of 67P and 103P has been estimated through the computation of gas production rates. In this chapter, we have analyzed their dust activity by means of the Afrho parameter. Thus, both quantities have been evaluated individually. It is also possible to combine them in order to get more information about the comet composition. Indeed, the calculation of dust-to-gas ratios is a straightforward way to know whether a comet is rather dust-rich or gas-rich.

The computation of cometary dust-to-gas ratios is usually done by using CN production rates,

and $Af\rho$ values obtained either with the broad-band R filter or the narrow-band RC filter. In this work, the ratios for 67P have been computed using the CN production rates and the $Af\rho$ values measured with the R filter. However, for 103P, neither R data nor RC data were available for the first passage, so we chose to use the $Af\rho$ values measured with the GC filter, in order to be able to compare the ratios for the two passages.

In this way, we followed the evolution of the dust-to-gas ratios with the heliocentric distance for both comets, and studied their variation from one passage to the other. The results are presented below.

Comet 67P/Churyumov-Gerasimenko

The values of $A(0)f\rho/Q_{\mathrm{CN}}$ computed for 67P are given in logarithms in Table B.8 in the appendix, for both the first and the second passages of the comet. These ratios have also been plotted as a function of heliocentric distance. The results are shown in Figure 5.15.

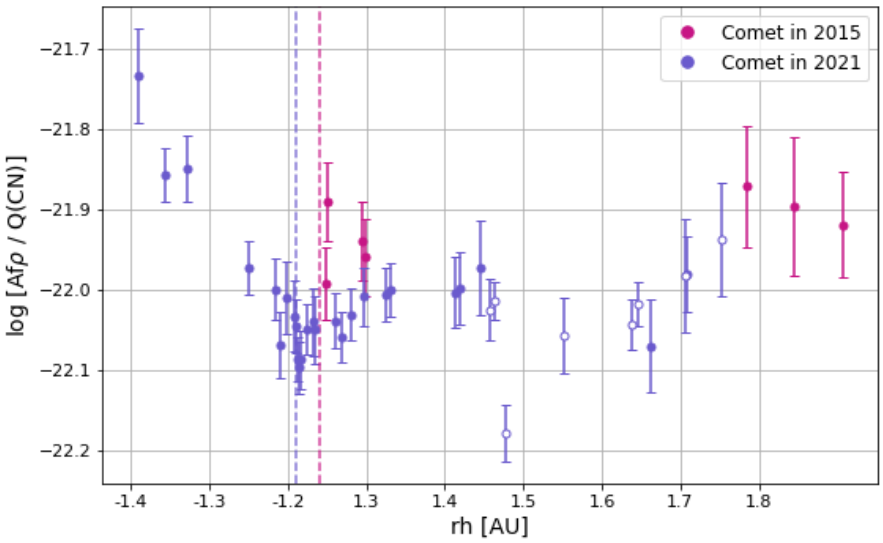

Figure 5.15. Evolution of the dust-to-gas ratios of comet 67P as a function of the heliocentric distance. The dashed, colored lines represent the heliocentric distances at perihelion for the first (1.24 AU) and second (1.21 AU) passages. Solid and empty points stand for TS and TN data, respectively.

Apart from the two data points seen at $r_h > 1.3$ AU in the pre-perihelion phase, the dust-to-gas ratios of 67P measured in 2021 appear approximately constant over the whole perihelion passage. Regarding the data obtained in 2015, the trend followed by the ratio values can not really be evaluated. However, they seem in very good agreement with those obtained in 2021, showing that they have remained constant from one passage to the other.

Comet 103P/Hartley 2

The values of the logarithm of $A(0)f\rho/Q_{\mathrm{CN}}$ computed for the 2010 and 2023 passages of 103P are given in Table B.9 in the appendix, and their variation as a function heliocentric distance is represented in Figure B.9.

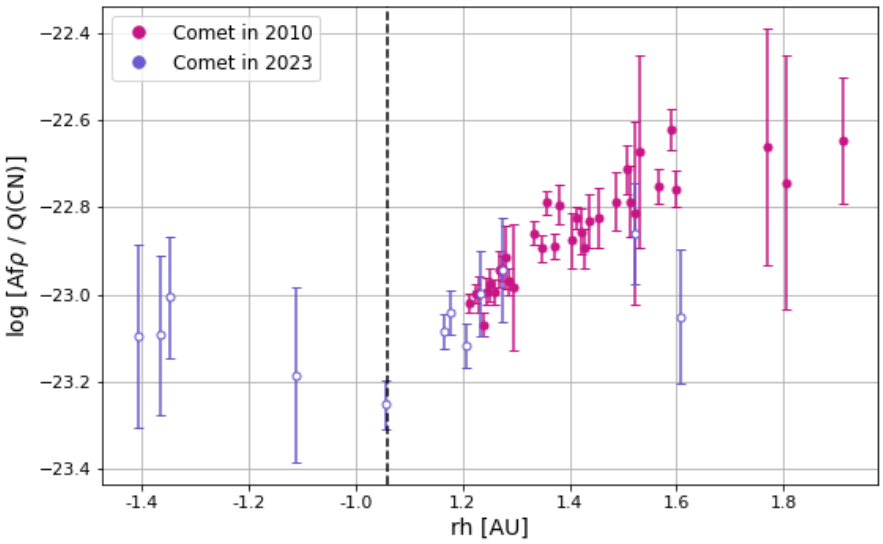

Figure 5.16. Evolution of the dust-to-gas ratios of comet 103P as a function of the heliocentric distance. The dashed, black line represents the heliocentric distance at perihelion (1.06 AU). Solid and empty points stand for TS and TN data, respectively.

Contrarily to 67P, the dust-to-gas ratios of 103P does not remain constant over the perihelion passages. We detect a slight decrease in the ratios (the comet becomes less dusty) as the comet approaches the Sun, and a clear increase (the comet becomes dustier) after perihelion. A possible explanation for this observation is a variation of the dust-emitting region at the surface of the nucleus. We can see that the values of $\log[Af\rho/Q_{\mathrm{CN}}]$ measured for the 2010 and 2023 passages of the comet overlap within the heliocentric distance range from approximately 1.1 to 1.5 AU. They are thus in excellent agreement and indicate, as for 67P, that the dust-to-gas ratios might be constant over time. Moreover, we notice a difference of one order of magnitude between the values measured for this comet and those measured for 67P. Indeed, at perihelion, $\log[Af\rho/Q_{\mathrm{CN}}] = -22.05 \pm 0.04$ for 67P, while $\log[Af\rho/Q_{\mathrm{CN}}] = -23.25 \pm 0.06$ for 103P. This indicates that, as compared to 67P, 103P is a relatively dust-poor comet, and this result is in accord with what we had already established before.

Chapter 6

Coma morphology

So far, we have mainly been interested in cometary coma composition. However, cometary comae also have well-defined internal structures that can be studied based on the images. In general, these structures are due to nucleus-related processes. Indeed, as already mentioned, comet nuclei are non homogeneous. Some regions contain more dust and ice particles than others, and are thus more active. This often gives rise to various morphological features, such as bright jets, fans, or arcs, that can be observed in the coma.

Analyzing the coma morphology is an important part of comet study. It can provide some clues about the properties and structure of the nucleus, whose direct observations are compromised by the large and bright surrounding coma. For instance, the position of active areas on the surface of a comet can be inferred from the structures observed inside its coma. In the case of long comet observation campaigns, it is also possible to derive the rotation period of the nucleus by studying the periodic changes in morphological features.

We attempted to analyze the morphological features in our target comets' coma. This chapter describes the technique we used to enhance our cometary images, in order to be able to distinguish the internal structures, as well as the features we could identify.

6.1 Image enhancement techniques

Because of the brightness of cometary comae, the structural features present both in the outer regions and close to the optocenter are often too difficult to detect on regular (unenhanced) comet images. For that reason, the coma morphology analyses require an enhancement of the images, that aims at improving the contrast between the internal structures and the rest of the coma in order to make the identification of structures easier.

Within the framework of this work, we used the online Cometary Coma Image Enhancement Facility[1] from Planetary Science Institute (PSI) to realize the enhancement of our images. This tool implements enhancement algorithms and codes developed in 2013 by Nalin Samarasinha and Steve Larson. Five different enhancement routines are provided: division by azimuthal average, division by azimuthal median, azimuthal renormalization, division by $1/\rho$, and radially variable spatial filtering. We describe here the technique of division by an azimuthal median profile, that was used in this work, but a complete description of the four other techniques is available on the PSI's website. Division by azimuthal median consists in a division of the brightness value of each pixel located at a given radial distance from the comet center by the median brightness of all the pixels located at the same radial distance. In other words, successive one-pixel wide circles (called the azimuths) are considered from the optocenter to the edges of the image, and the median brightness of each circle is computed. Then, the brightness value of each pixel located in a given circle is divided by the median brightness of the circle.

As an example, Figure 6.1 shows the result of the enhancement process performed on a CN image of comet 103P.

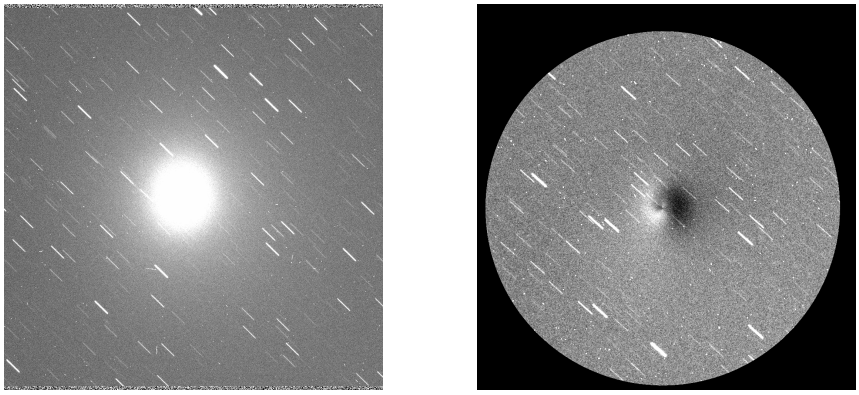

Figure 6.1. CN image of comet 103P obtained on October 1, 2023, before (left) and after (right) enhancement through the technique of division by azimuthal median.

6.2 Results

We applied the enhancement technique on several CN images of 67P and 103P obtained at different dates during their perihelion passages. The resulting enhanced images on which we were able to identify some structural features are presented in this section.

[1]Cometary Coma Image Enhancement Facility: `https://cie.psi.edu/`

Comet 67P/Churyumov-Gerasimenko

According to Lamy et al. (2006), the nucleus of comet 67P is weakly active, with an active fraction of its surface of only $\sim$ 6% at the time of production rate peak. A major part of the nucleus being inactive, this implies that 67P probably displays a small number of active regions on its surface. Given this result, we expect to not observe more than one internal feature in its coma.

Few CN images were available for the first passage of 67P. After their enhancement, only two of them were displaying a clear coma asymmetry that can be identified as a morphological feature. These two enhanced images, obtained in September 2021, are presented in Figures 6.2 and 6.3.

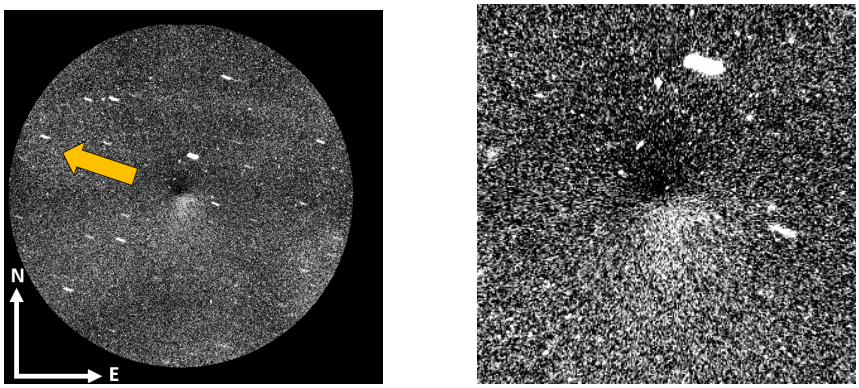

Figure 6.2. Left: CN image of comet 67P obtained on September 11, 2015, enhanced through the technique of division by azimuthal median. Right: Zoom on the optocenter. The North and East directions are indicated. The yellow arrow shows the direction of the Sun.

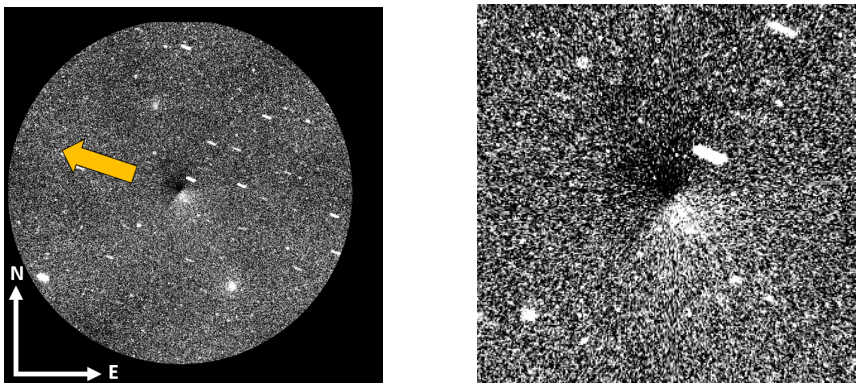

Figure 6.3. Left: CN image of comet 67P obtained on September 12, 2015, enhanced through the technique of division by azimuthal median. Right: Zoom on the optocenter. The North and East directions are indicated. The yellow arrow shows the direction of the Sun.

For the second passage of the comet, more CN images were available, and the best enhancement results were obtained for the images collected during December 2021, January, and the beginning

of February 2022. Some of the enhanced images are presented in Figures 6.4 to 6.7.

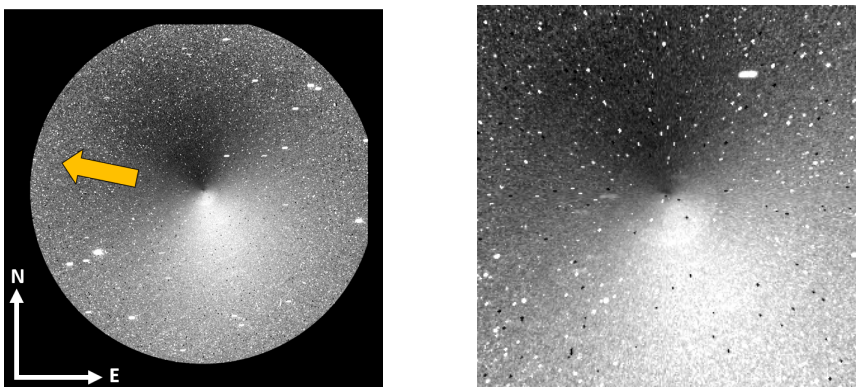

Figure 6.4. Left: CN image of comet 67P obtained on December 9, 2021, enhanced through the technique of division by azimuthal median. Right: Zoom on the optocenter. The North and East directions are indicated. The yellow arrow shows the direction of the Sun.

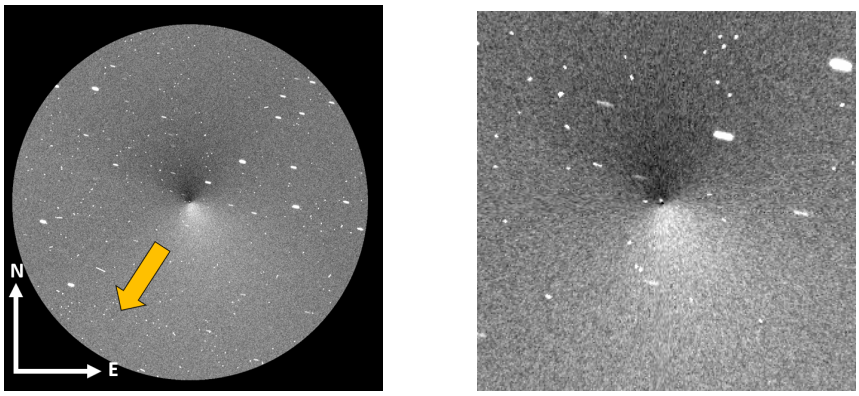

Figure 6.5. Left: CN image of comet 67P obtained on January 21, 2022, enhanced through the technique of division by azimuthal median. Right: Zoom on the optocenter. The North and East directions are indicated. The yellow arrow shows the direction of the Sun.

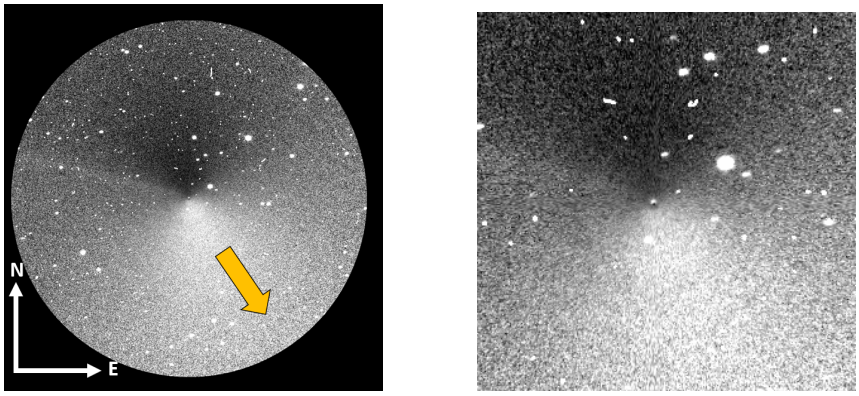

Figure 6.6. Left: CN image of comet 67P obtained on February 2, 2022, enhanced through the technique of division by azimuthal median. Right: Zoom on the optocenter. The North and East directions are indicated. The yellow arrow shows the direction of the Sun.

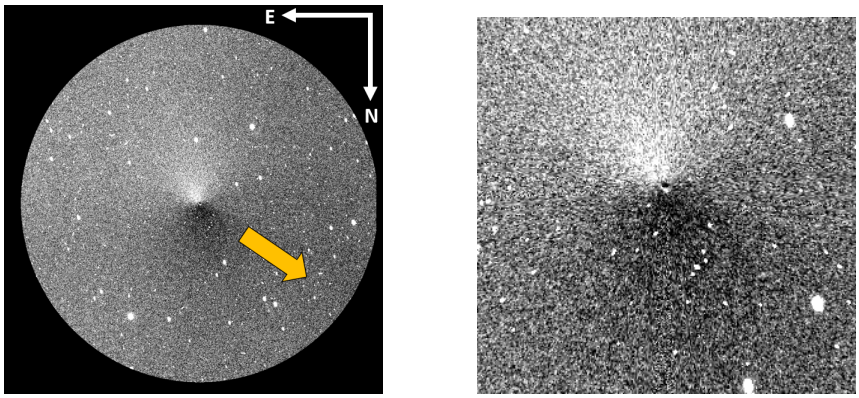

Figure 6.7. Left: CN image of comet 67P obtained on February 11, 2022, enhanced through the technique of division by azimuthal median. Right: Zoom on the optocenter. The North and East directions are indicated. The yellow arrow shows the direction of the Sun.

In each of the above images, we detect a broad, triangular feature (generally called a "fan"), extending radially from the nucleus. It probably indicates the presence of a region of higher activity at the surface of 67P, ejecting larger amounts of gas. This observed structure is fairly constant over the period from December to February.

Comet 103P/Hartley 2

Contrarily to 67P, the nucleus of comet 103P is very active. Indeed, its surface has an active proportion of more than 30% (see for example Groussin et al. (2004)), which is relatively high as compared to most JFCs, for which this fraction is generally lower than 10%. Consequently, we expect to observe large structural features in its coma, probably originating from several regions of the surface. However, as mentioned by Farnham (2009), these features are often difficult to distinguish

given the high active fraction.

A great number of CN images have been collected during the 2010 passage of 103P. However, only faint morphological features could be detected in some images. An example of these features is given in Figure 6.8, showing an enhanced CN image of the comet obtained in December 2010. In this image, we observe a faint spiral-shaped structure originating from the nucleus. As for 67P, it might indicate the existence of an active region on the surface of 103P, the spiral shape being the consequence of the nucleus rotation.

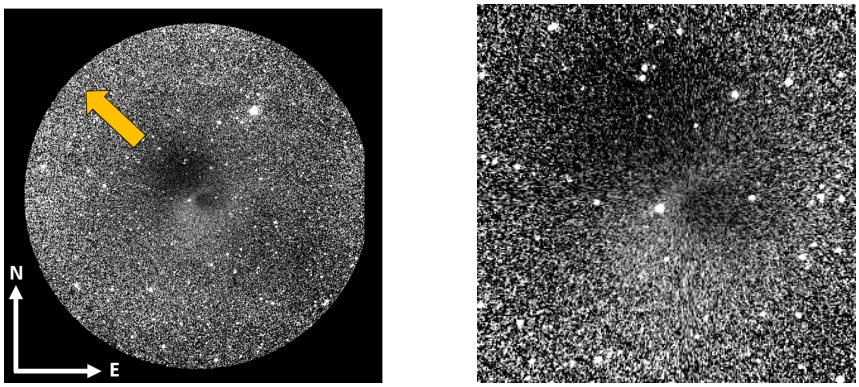

Figure 6.8. Left: CN image of comet 103P obtained on December 9, 2010, enhanced through the technique of division by azimuthal median. Right: Zoom on the optocenter. The North and East directions are indicated. The yellow arrow shows the direction of the Sun.

Finally, the morphological features that we could detect through the enhancement of the CN images obtained in 2023 were much more obvious. Some of the best results are shown in Figures 6.9 to 6.13.

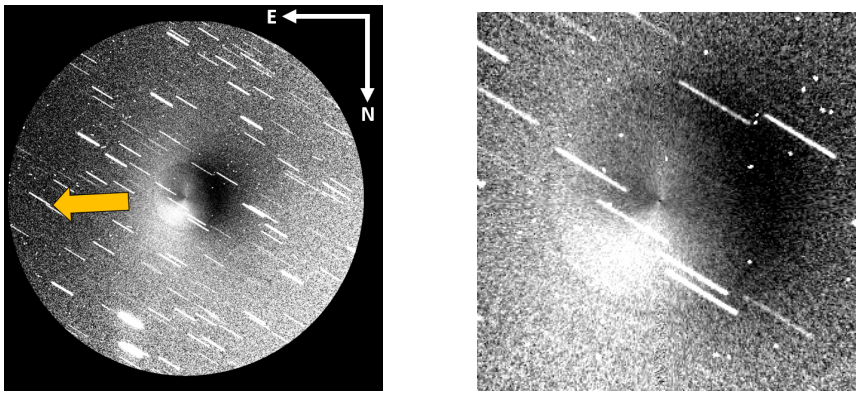

Figure 6.9. Left: CN image of comet 103P obtained on September 22, 2023, enhanced through the technique of division by azimuthal median. Right: Zoom on the optocenter. The North and East directions are indicated. The yellow arrow shows the direction of the Sun.

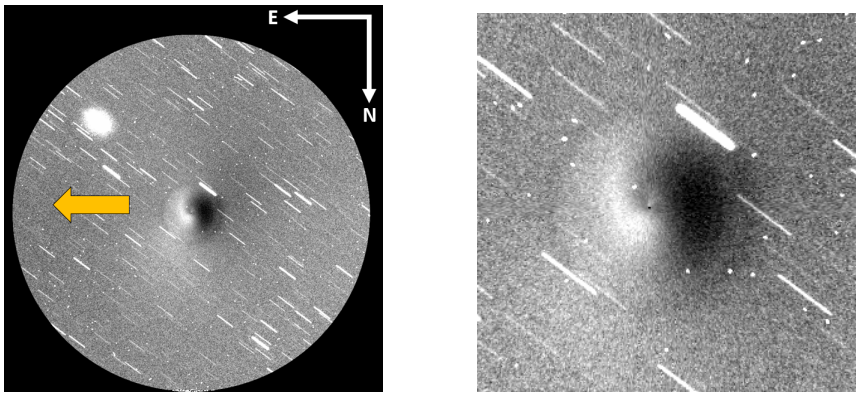

Figure 6.10. Left: CN image of comet 103P obtained on September 27, 2023, enhanced through the technique of division by azimuthal median. Right: Zoom on the optocenter. The North and East directions are indicated. The yellow arrow shows the direction of the Sun.

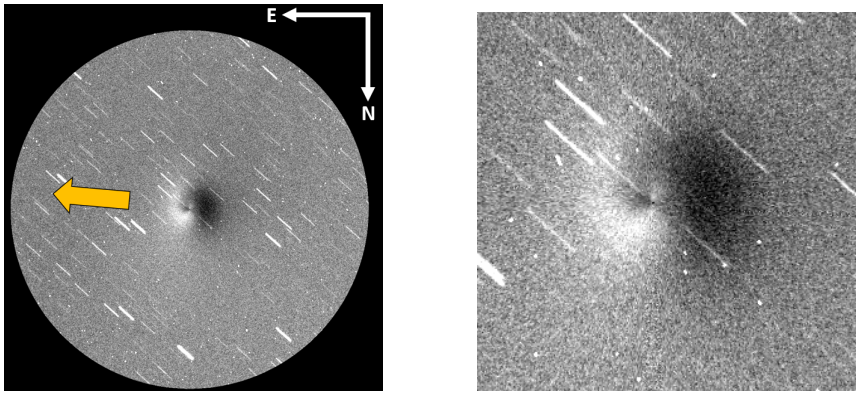

Figure 6.11. Left: CN image of comet 103P obtained on October 1, 2023, enhanced through the technique of division by azimuthal median. Right: Zoom on the optocenter. The North and East directions are indicated. The yellow arrow shows the direction of the Sun.

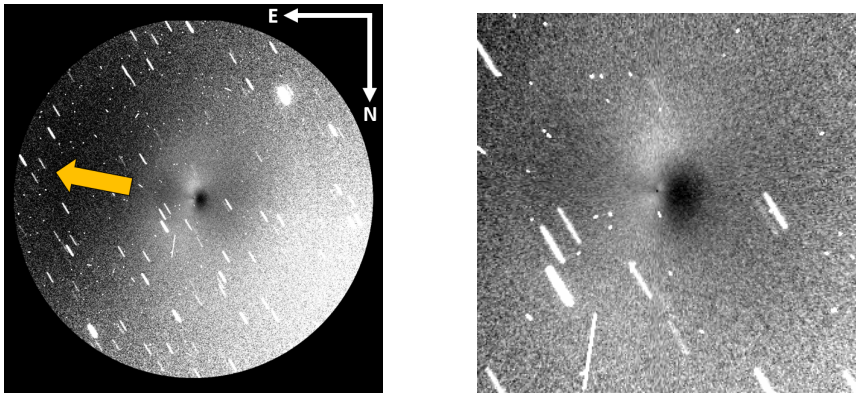

Figure 6.12. Left: CN image of comet 103P obtained on October 25, 2023, enhanced through the technique of division by azimuthal median. Right: Zoom on the optocenter. The North and East directions are indicated. The yellow arrow shows the direction of the Sun.

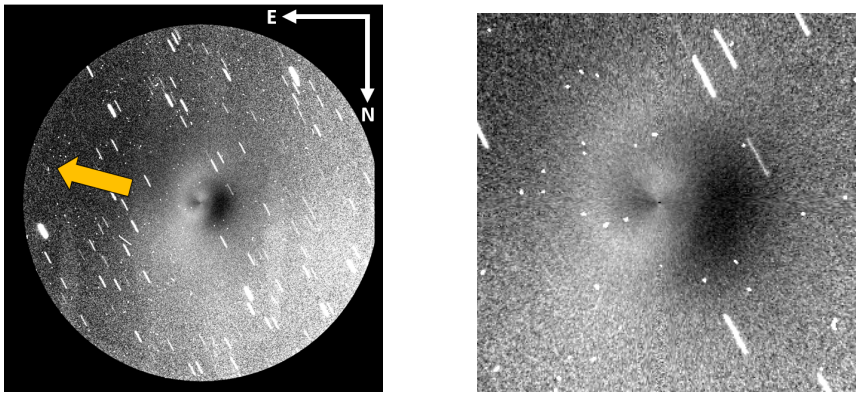

Figure 6.13. Left: CN image of comet 103P obtained on November 10, 2023, enhanced through the technique of division by azimuthal median. Right: Zoom on the optocenter. The North and East directions are indicated. The yellow arrow shows the direction of the Sun.

In Figures 6.9 to 6.11, we unambiguously observe a spiral-shaped structure in the coma of 103P, that is similar to the one observed in the 2010 images but with a higher intensity. We clearly see the jet of gas and dust originating from a region of the nucleus of high activity, and wrapping around the nucleus as the latter is rotating.

In the images obtained during the post-perihelion phase of the comet (i.e., in Figures 6.12 and 6.13), we detect another structure emerging from the nucleus, additionally to the first one already observed during September and the beginning of October. This second structure seems to originate from a different side of the comet surface, indicating the presence of another active region.

Conclusion

The study of comets is of crucial importance to our understanding of the origins and evolution of the Solar System. As remnants of the earliest phases of planetary formation, these celestial bodies contain valuable information about the chemical and physical conditions that prevailed 4.6 billion years ago. The aim of this work was to contribute to this understanding by analyzing the evolution of the activity and composition of two famous periodic comets, 67P/Churyumov-Guerasimenko and 103P/Hartley 2.

To do this, we used high-quality images collected during observing campaigns carried out with the TRAPPIST telescopes. Comet 67P was observed during its last two perihelion passages, in 2015 and 2021, while 103P was observed in 2010 and 2023. In particular, the extensive data collected with BVRI broad-band filters and Hale-Bopp narrow-band filters has enabled us to follow and analyze comet magnitudes, measure the production rates of gaseous molecules in their coma, and quantify dust activity around cometary nuclei. In this way, we were able to compare the activities of the two comets during two different perihelion passages.

Our results for the photometric analysis of comets revealed a strong seasonal effect for 67P, with peak brightness shifted by almost 20 days relative to perihelion, and a consequent asymmetry of light curves relative to perihelion. Conversely, this effect was not visible in the light curves obtained for 103P. Another point worth mentioning is that we did not observe any outbursts in the comets' magnitude curves, although the Rosetta probe had measured a few small ones during its mission around 67P in 2014 and 2015. We then calculated the heliocentric magnitude of the comets by removing the dependence of the Earth-comet distance on the apparent magnitude in order to compare our data for two different passages. This revealed, for both comets, a brighter coma during the second passage than during the first. However, it would be interesting to investigate whether this difference could be attributed to the phase angle during the observations. The data from each passage were fitted to determine the parameters M (absolute magnitude) and n (power-law slope) of the magnitude equation. Finally, we calculated the color indices of the two comets, and obtained values consistent with the average values for Jupiter-family comets, and redder than the solar colors. We also detected a decrease in these indices for 103P between 2010 and 2023, while for 67P the

values remained constant from one passage to the next.

In the second part of this work, we calculated production rates for the molecular species OH, NH, CN, C_2 and C_3 in the coma of both comets, analyzed their evolution as a function of heliocentric distance, and studied their variation from one passage to the next. We found that 67P's gas activity was more intense during its second passage, while 103P's activity was more intense during its first passage. We then calculated the C_2-to-CN production rate ratios in order to classify comets according to their carbonaceous element content, based on a criterion established by A'Hearn et al. (1995). Our data show that 67P and 103P are both typical comets, and that the calculated production rate ratios did not vary from one passage to the other. We also derived the water production rates from the OH production rates of the comets. It would be interesting to compare our values with those obtained by other authors during different comet passages, in order to analyze the long-term variation in these water production rates.

We then estimated the dust activity of comets by calculating its parameter $Af\rho$ and correcting it for the phase angle effect. We analyzed the evolution of this parameter as a function of the comets' heliocentric distance, as well as their variation from one perihelion passage to the other. We observed a similar trend to that of the gases, i.e., 67P's dust activity was more intense during its second passage in 2021 than during its first passage in 2015, while 103P was more active during its first passage in 2010 than during its second passage in 2023. We also calculated dust-to-gas activity ratios to assess the dust content of the comets. Our measurements notably revealed that 103P is a dust-poor comet as compared to 67P.

Finally, we performed an enhancement of several CN images to highlight internal structures in the comae. This revealed several morphological features. For 67P, we observed a large jet of gas expanding radially from the nucleus, indicating the presence of a region of high activity at the surface of the nucleus. For 103P, the jets observed spiraled around the nucleus and seemed to indicate the presence of at least two active regions.

In conclusion, our results do indeed seem to show changes in cometary activity between perihelion passages, with 67P more active in 2021 than in 2015, and 103P more active in 2010 than in 2023. This underlines the importance of continuing these studies over several orbital cycles with the TRAPPIST telescopes, in order to better understand cometary evolution processes.

Appendix A

Computed gas production rates

Table A.1. Gas production rates Q in molecules per second measured during the 2015 perihelion passage of comet 67P.

Date	r_h [AU][a]	Q_{CN} [mol/s]	$Q_{\mathrm{C_2}}$ [mol/s]
2015-08-22	1.25	$5.91 \pm 0.61 \times 10^{24}$	-
2015-08-23	1.25	-	$8.16 \pm 0.69 \times 10^{24}$
2015-08-24	1.25	$6.88 \pm 0.77 \times 10^{24}$	-
2015-08-30	1.26	-	$8.43 \pm 0.93 \times 10^{24}$
2015-09-11	1.29	$7.91 \pm 0.88 \times 10^{24}$	-
2015-09-12	1.30	$8.39 \pm 0.91 \times 10^{24}$	-
2015-09-13	1.30	-	$4.65 \pm 1.11 \times 10^{24}$
2015-12-01	1.79	$2.03 \pm 0.34 \times 10^{24}$	-
2015-12-08	1.84	-	$1.92 \pm 0.23 \times 10^{24}$
2015-12-09	1.85	$1.90 \pm 0.37 \times 10^{24}$	-
2015-12-10	1.85	-	$2.25 \pm 0.51 \times 10^{24}$
2015-12-17	1.91	$2.02 \pm 0.30 \times 10^{24}$	-

[a] Heliocentric distance of the comet.

Table A.2. Gas production rates Q in molecules per second measured during the 2021 perihelion passage of comet 67P. Please note that, for the species observed several times over a given night, only the average value obtained is given.

Date	r_h [AU][a]	Q_{OH} [mol/s]	Q_{NH} [mol/s]	Q_{CN} [mol/s]	$Q_{\mathrm{C_2}}$ [mol/s]	$Q_{\mathrm{C_3}}$ [mol/s]
2021-08-12	1.56	-	-	$0.05 \pm 0.01 \times 10^{25}$	-	-
2021-09-04	1.41	-	-	$0.18 \pm 0.02 \times 10^{25}$	$0.17 \pm 0.02 \times 10^{25}$	-
2021-09-10	1.38	-	-	$0.27 \pm 0.02 \times 10^{25}$	$0.29 \pm 0.02 \times 10^{25}$	-
2021-09-15	1.35	-	-	$0.27 \pm 0.03 \times 10^{25}$	$0.28 \pm 0.03 \times 10^{25}$	-
2021-10-01	1.27	-	-	-	$0.35 \pm 0.04 \times 10^{25}$	-
2021-10-02	1.27	-	-	$0.44 \pm 0.03 \times 10^{25}$	$0.40 \pm 0.04 \times 10^{25}$	-
2021-10-11	1.24	-	-	$0.60 \pm 0.05 \times 10^{25}$	$0.51 \pm 0.08 \times 10^{25}$	-
2021-10-13	1.24	$2.83 \pm 0.58 \times 10^{27}$	-	$0.54 \pm 0.05 \times 10^{25}$	$0.48 \pm 0.07 \times 10^{25}$	-
2021-10-16	1.23	$3.31 \pm 0.83 \times 10^{27}$	-	$0.64 \pm 0.06 \times 10^{25}$	$0.57 \pm 0.06 \times 10^{25}$	-
2021-10-20	1.22	$2.84 \pm 0.78 \times 10^{27}$	-	$0.60 \pm 0.06 \times 10^{25}$	$0.58 \pm 0.10 \times 10^{25}$	-
2021-10-30	1.21	$4.56 \pm 1.22 \times 10^{27}$	-	$0.82 \pm 0.08 \times 10^{25}$	$0.74 \pm 0.09 \times 10^{25}$	-
2021-11-04	1.21	$4.95 \pm 1.28 \times 10^{27}$	-	$0.88 \pm 0.07 \times 10^{25}$	$0.83 \pm 0.08 \times 10^{25}$	$1.39 \pm 0.19 \times 10^{24}$
2021-11-07	1.21	$3.96 \pm 1.21 \times 10^{27}$	-	$1.00 \pm 0.06 \times 10^{25}$	$0.87 \pm 0.06 \times 10^{25}$	-
2021-11-08	1.21	$4.06 \pm 1.08 \times 10^{27}$	$2.41 \pm 0.60 \times 10^{25}$	-	-	$1.35 \pm 0.25 \times 10^{24}$
2021-11-09	1.21	-	-	$1.06 \pm 0.08 \times 10^{25}$	$0.93 \pm 0.05 \times 10^{25}$	-
2021-11-12	1.22	$4.02 \pm 1.08 \times 10^{27}$	-	$1.07 \pm 0.09 \times 10^{25}$	$0.91 \pm 0.07 \times 10^{25}$	$1.39 \pm 0.24 \times 10^{24}$
2021-11-16	1.22	-	-	$1.03 \pm 0.07 \times 10^{25}$	$0.87 \pm 0.06 \times 10^{25}$	$1.39 \pm 0.17 \times 10^{24}$
2021-11-20	1.23	$3.64 \pm 1.13 \times 10^{27}$	-	$1.12 \pm 0.11 \times 10^{25}$	$1.04 \pm 0.11 \times 10^{25}$	$1.40 \pm 0.33 \times 10^{24}$
2021-11-21	1.24	$6.22 \pm 2.06 \times 10^{27}$	$1.86 \pm 0.78 \times 10^{25}$	$1.12 \pm 0.11 \times 10^{25}$	$1.07 \pm 0.11 \times 10^{25}$	-
2021-11-30	1.26	$5.39 \pm 1.12 \times 10^{27}$	-	$1.16 \pm 0.09 \times 10^{25}$	$1.01 \pm 0.06 \times 10^{25}$	$1.55 \pm 0.22 \times 10^{24}$
2021-12-02	1.27	$5.39 \pm 1.21 \times 10^{27}$	-	$1.19 \pm 0.08 \times 10^{25}$	$0.98 \pm 0.07 \times 10^{25}$	$1.24 \pm 0.31 \times 10^{24}$
2021-12-05	1.28	$5.59 \pm 1.08 \times 10^{27}$	-	$1.07 \pm 0.08 \times 10^{25}$	$0.91 \pm 0.08 \times 10^{25}$	$1.33 \pm 0.34 \times 10^{24}$
2021-12-09	1.30	$4.69 \pm 9.97 \times 10^{27}$	-	$1.02 \pm 0.09 \times 10^{25}$	$0.97 \pm 0.08 \times 10^{25}$	$1.24 \pm 0.24 \times 10^{24}$
2021-12-15	1.33	-	-	$0.95 \pm 0.07 \times 10^{25}$	-	$1.25 \pm 0.22 \times 10^{24}$
2021-12-16	1.33	$4.38 \pm 1.13 \times 10^{27}$	-	$0.96 \pm 0.07 \times 10^{25}$	$0.97 \pm 0.08 \times 10^{25}$	$1.17 \pm 0.23 \times 10^{24}$
2021-12-31	1.41	$3.04 \pm 1.17 \times 10^{27}$	-	$0.78 \pm 0.08 \times 10^{25}$	$0.83 \pm 0.07 \times 10^{25}$	-
2022-01-01	1.42	$2.40 \pm 1.02 \times 10^{27}$	-	$0.73 \pm 0.08 \times 10^{25}$	$0.85 \pm 0.06 \times 10^{25}$	$0.78 \pm 0.27 \times 10^{24}$
2022-01-05	1.45	$2.77 \pm 0.69 \times 10^{27}$	-	$0.63 \pm 0.08 \times 10^{25}$	$0.66 \pm 0.06 \times 10^{25}$	$0.66 \pm 0.26 \times 10^{24}$
2022-01-07	1.46	$3.51 \pm 5.41 \times 10^{27}$	$0.40 \pm 0.46 \times 10^{25}$	$0.72 \pm 0.06 \times 10^{25}$	$0.85 \pm 0.06 \times 10^{25}$	$0.60 \pm 0.32 \times 10^{24}$
2022-01-08	1.46	$3.35 \pm 4.84 \times 10^{27}$	$0.61 \pm 0.39 \times 10^{25}$	$0.69 \pm 0.04 \times 10^{25}$	$0.83 \pm 0.05 \times 10^{25}$	$0.82 \pm 0.11 \times 10^{24}$
2022-01-10	1.48	$2.25 \pm 5.95 \times 10^{27}$	-	$0.71 \pm 0.06 \times 10^{25}$	$0.90 \pm 0.06 \times 10^{25}$	$0.89 \pm 0.21 \times 10^{24}$
2022-01-21	1.55	$2.02 \pm 3.66 \times 10^{27}$	$0.97 \pm 0.84 \times 10^{25}$	$0.58 \pm 0.06 \times 10^{25}$	-	$0.53 \pm 0.45 \times 10^{24}$
2022-01-24	1.57	$1.89 \pm 0.39 \times 10^{27}$	-	-	-	-
2022-02-02	1.64	$1.76 \pm 3.15 \times 10^{27}$	-	$0.48 \pm 0.03 \times 10^{25}$	$0.62 \pm 0.05 \times 10^{25}$	-
2022-02-03	1.65	$1.38 \pm 0.30 \times 10^{27}$	$0.09 \pm 0.25 \times 10^{25}$	$0.42 \pm 0.03 \times 10^{25}$	$0.56 \pm 0.03 \times 10^{25}$	-
2022-02-05	1.66	-	-	$0.50 \pm 0.07 \times 10^{25}$	$0.43 \pm 0.07 \times 10^{25}$	-
2022-02-10	1.71	$0.82 \pm 0.35 \times 10^{27}$	-	$0.33 \pm 0.05 \times 10^{25}$	$0.40 \pm 0.05 \times 10^{25}$	$0.20 \pm 0.24 \times 10^{24}$
2022-02-11	1.71	$0.62 \pm 0.33 \times 10^{27}$	-	$0.32 \pm 0.04 \times 10^{25}$	$0.37 \pm 0.05 \times 10^{25}$	$0.15 \pm 0.18 \times 10^{24}$
2022-02-16	1.75	$0.73 \pm 0.35 \times 10^{27}$	-	-	-	-
2022-02-17	1.75	-	$0.31 \pm 0.84 \times 10^{25}$	$0.33 \pm 0.05 \times 10^{25}$	$0.52 \pm 0.22 \times 10^{25}$	$0.39 \pm 0.34 \times 10^{24}$
2022-02-18	1.76	$0.79 \pm 0.42 \times 10^{27}$	-	$0.30 \pm 0.07 \times 10^{25}$	$0.34 \pm 0.21 \times 10^{25}$	$0.19 \pm 0.32 \times 10^{24}$

[a] Heliocentric distance of the comet.

Table A.3. Gas production rates Q in molecules per second measured during the 2010 perihelion passage of comet 103P. Please note that, for the species observed several times over a given night, only the average value obtained is given.

Date	r_h [AU][a]	Q_{OH} [mol/s]	Q_{CN} [mol/s]	Q_{C_2} [mol/s]	Q_{C_3} [mol/s]
2010-12-09	1.21	-	-	$20.21 \pm 1.89\times10^{24}$	$3.47 \pm 0.69\times10^{24}$
2010-12-10	1.21	$3.69\pm 0.17\times10^{27}$	$17.81 \pm 0.55\times10^{24}$	$19.97 \pm 0.66\times10^{24}$	$3.91 \pm 0.23\times10^{24}$
2010-12-12	1.22	$3.40 \pm 0.17\times10^{27}$	$15.38 \pm 0.42\times10^{24}$	$18.48 \pm 0.48\times10^{24}$	$3.20 \pm 0.20\times10^{24}$
2010-12-13	1.23	-	$15.28 \pm 0.58\times10^{24}$	$17.68 \pm 0.91\times10^{24}$	$3.198 \pm 0.38\times10^{24}$
2010-12-14	1.24	$3.58 \pm 0.20\times10^{27}$	$17.78 \pm 0.51\times10^{24}$	$19.09 \pm 0.63\times10^{24}$	$3.87 \pm 0.20\times10^{24}$
2010-12-15	1.25	$3.41 \pm 0.22\times10^{27}$	$14.15 \pm 0.50\times10^{24}$	$16.74 \pm 0.60\times10^{24}$	$2.95 \pm 0.24\times10^{24}$
2010-12-16	1.25	$3.40\pm 0.28\times10^{27}$	$14.04 \pm 0.56\times10^{24}$	$16.35 \pm 0.84\times10^{24}$	$2.85 \pm 0.31\times10^{24}$
2010-12-17	1.26	$3.38\pm 0.19\times10^{27}$	$14.30 \pm 0.38\times10^{24}$	$15.58 \pm 0.49\times10^{24}$	$2.93 \pm 0.17\times10^{24}$
2010-12-18	1.27	$3.18\pm 0.36\times10^{27}$	$13.14 \pm 0.72\times10^{24}$	$15.19 \pm 0.85\times10^{24}$	$2.90 \pm 0.31\times10^{24}$
2010-12-19	1.27	$3.25\pm 0.15\times10^{27}$	$12.39 \pm 0.30\times10^{24}$	$14.59 \pm 0.47\times10^{24}$	$2.65 \pm 0.18\times10^{24}$
2010-12-20	1.28	$3.02 \pm 0.25\times10^{27}$	$10.86 \pm 0.64\times10^{24}$	$12.43 \pm 0.98\times10^{24}$	$2.04 \pm 0.34\times10^{24}$
2010-12-21	1.29	$2.83 \pm 0.12\times10^{27}$	$12.41 \pm 0.32\times10^{24}$	$13.04 \pm 0.45\times10^{24}$	$2.53 \pm 0.21\times10^{24}$
2010-12-22	1.30	$2.83 \pm 0.29\times10^{27}$	$10.94 \pm 0.72\times10^{24}$	$12.01 \pm 1.25\times10^{24}$	$2.18 \pm 0.55\times10^{24}$
2010-12-27	1.33	$2.50 \pm 0.12\times10^{27}$	$9.317 \pm 0.26\times10^{24}$	$9.893 \pm 0.38\times10^{24}$	$2.01 \pm 0.15\times10^{24}$
2010-12-29	1.35	$2.53 \pm 0.16\times10^{27}$	$10.12 \pm 0.32\times10^{24}$	$11.10 \pm 0.46\times10^{24}$	$2.01 \pm 0.19\times10^{24}$
2010-12-30	1.36	$2.29 \pm 0.13\times10^{27}$	$8.35 \pm 0.22\times10^{24}$	$9.28 \pm 0.34\times10^{24}$	$1.60 \pm 0.15\times10^{24}$
2011-01-01	1.37	$2.49 \pm 0.17\times10^{27}$	$9.87 \pm 0.33\times10^{24}$	$9.81 \pm 0.48\times10^{24}$	$2.01 \pm 0.17\times10^{24}$
2011-01-02	1.38	$2.30 \pm 0.20\times10^{27}$	$7.53 \pm 0.36\times10^{24}$	$8.42 \pm 0.65\times10^{24}$	$1.46 \pm 0.25\times10^{24}$
2011-01-03	1.39	$2.45 \pm 0.12\times10^{27}$	$9.44 \pm 0.24\times10^{24}$	$9.68 \pm 0.35\times10^{24}$	$1.93 \pm 0.13\times10^{24}$
2011-01-04	1.40	$2.25 \pm 0.21\times10^{27}$	$8.20 \pm 0.62\times10^{24}$	$8.56 \pm 0.64\times10^{24}$	$1.44 \pm 0.31\times10^{24}$
2011-01-06	1.41	$2.09 \pm 0.14\times10^{27}$	$7.93 \pm 0.24\times10^{24}$	$8.15 \pm 0.35\times10^{24}$	$1.46 \pm 0.15\times10^{24}$
2011-01-07	1.42	$2.01 \pm 0.29\times10^{27}$	$8.50 \pm 0.30\times10^{24}$	$8.65 \pm 0.62\times10^{24}$	$1.72 \pm 0.16\times10^{24}$
2011-01-08	1.43	$1.97 \pm 0.20\times10^{27}$	$8.75 \pm 0.35\times10^{24}$	$8.12 \pm 0.51\times10^{24}$	$1.57 \pm 0.25\times10^{24}$
2011-01-09	1.44	$2.07 \pm 0.22\times10^{27}$	$7.71 \pm 0.41\times10^{24}$	$8.10 \pm 0.55\times10^{24}$	$1.43 \pm 0.26\times10^{24}$
2011-02-11	1.45	$1.88 \pm 0.21\times10^{27}$	$7.29 \pm 0.40\times10^{24}$	$6.70 \pm 0.55\times10^{24}$	$1.39 \pm 0.29\times10^{24}$
2011-02-12	1.46	$1.68 \pm 0.41\times10^{27}$	$7.49 \pm 0.58\times10^{24}$	$6.92 \pm 0.86\times10^{24}$	$1.27 \pm 0.40\times10^{24}$
2011-02-13	1.47	$1.81 \pm 0.30\times10^{27}$	$6.22 \pm 0.54\times10^{24}$	$6.10 \pm 0.80\times10^{24}$	$1.00 \pm 0.32\times10^{24}$
2011-02-15	1.49	$1.53 \pm 0.24\times10^{27}$	$6.75 \pm 0.52\times10^{24}$	$5.86 \pm 0.69\times10^{24}$	$1.47 \pm 0.34\times10^{24}$
2011-02-17	1.51	-	$6.50 \pm 0.44\times10^{24}$	$5.82 \pm 0.54\times10^{24}$	$1.23 \pm 3.1 \times 10^{23}$
2011-02-18	1.51	$1.55 \pm 0.19\times10^{27}$	$6.42 \pm 0.35\times10^{24}$	$4.96 \pm 0.79\times10^{24}$	$1.30 \pm 0.40\times10^{24}$
2011-02-19	1.52	$1.41 \pm 0.24\times10^{27}$	$5.34 \pm 0.52\times10^{24}$	$5.07 \pm 1.05\times10^{24}$	$1.16 \pm 0.47\times10^{24}$
2011-02-20	1.53	$1.30 \pm 0.31\times10^{27}$	$4.51 \pm 0.59\times10^{24}$	$5.63 \pm 0.16\times10^{24}$	$1.02 \pm 0.69\times10^{24}$
2011-02-24	1.57	$1.42 \pm 0.14\times10^{27}$	$5.70 \pm 0.28\times10^{24}$	$5.97 \pm 0.43\times10^{24}$	$1.21 \pm 0.15\times10^{24}$
2011-02-27	1.59	$1.20 \pm 0.16\times10^{27}$	$4.34 \pm 0.28\times10^{24}$	$4.40 \pm 0.51\times10^{24}$	$0.92 \pm 0.18\times10^{24}$
2011-02-28	1.60	$1.18 \pm 0.16\times10^{27}$	$6.06 \pm 0.37\times10^{24}$	$5.22 \pm 0.52\times10^{24}$	$1.15 \pm 0.23\times10^{24}$
2011-02-16	1.77	$0.44 \pm 0.29\times10^{27}$	$3.18 \pm 0.46\times10^{24}$	-	$0.20 \pm 0.39\times10^{24}$
2011-02-20	1.81	$0.28 \pm 0.42\times10^{27}$	$3.33 \pm 0.79\times10^{24}$	$4.16 \pm 0.93\times10^{24}$	$0.96 \pm 0.67\times10^{24}$
2011-02-24	1.84	$0.60 \pm 0.42\times10^{27}$	$2.57 \pm 0.59\times10^{24}$	$2.08 \pm 1.15\times10^{24}$	$0.81 \pm 0.48\times10^{24}$
2011-03-04	1.91	$0.16 \pm 0.40\times10^{27}$	$2.29 \pm 0.34\times10^{24}$	$1.80 \pm 0.53\times10^{24}$	$0.31 \pm 0.26\times10^{24}$

[a] Heliocentric distance of the comet.

Table A.4. Gas production rates Q in molecules per second measured during the 2023 perihelion passage of comet 103P.

Date	r_h [AU][a]	Q_{OH} [mol/s]	Q_{NH} [mol/s]	Q_{CN} [mol/s]	Q_{C_2} [mol/s]	Q_{C_3} [mol/s]
2023-07-21	1.53	-	-	$1.78 \pm 0.13 \times 10^{24}$	$1.83 \pm 0.22 \times 10^{24}$	$3.43 \pm 0.78 \times 10^{24}$
2023-07-26	1.49	-	-	$2.19 \pm 0.20 \times 10^{24}$	-	-
2023-07-28	1.47	-	-	$2.14 \pm 0.18 \times 10^{24}$	-	-
2023-08-16	1.32	$7.10 \pm 1.91 \times 10^{26}$	-	$2.80 \pm 0.14 \times 10^{24}$	$2.80\pm 0.29 \times 10^{24}$	-
2023-08-19	1.29	$6.99 \pm 2.92 \times 10^{26}$	-	$2.92 \pm 0.15 \times 10^{24}$	$3.14 \pm 0.23 \times 10^{24}$	-
2023-08-22	1.27	-	-	$2.99 \pm 0.17 \times 10^{24}$	$3.27 \pm 0.29 \times 10^{24}$	-
2023-08-27	1.24	$6.54 \pm 3.00 \times 10^{26}$	-	$3.10 \pm 0.21 \times 10^{24}$	$3.51 \pm 0.29 \times 10^{24}$	$6.97 \pm 0.11 \times 10^{24}$
2023-08-28	1.23	$1.13 \pm 0.24 \times 10^{27}$	-	$3.74 \pm 0.31 \times 10^{24}$	$4.09 \pm 0.45 \times 10^{24}$	$7.70 \pm 0.15 \times 10^{24}$
2023-08-30	1.22	$1.20 \pm 0.22 \times 10^{27}$	-	$3.59 \pm 0.37 \times 10^{24}$	$3.91 \pm 0.56 \times 10^{24}$	$8.20 \pm 0.12 \times 10^{24}$
2023-09-01	1.21	-	$5.63 \pm 4.34 \times 10^{24}$	-	-	-
2023-09-17	1.12	-	-	$8.09 \pm 0.44 \times 10^{24}$	$8.66 \pm 0.49 \times 10^{24}$	-
2023-09-19	1.11	$1.52 \pm 0.56 \times 10^{27}$	-	-	-	$1.43 \pm 0.30 \times 10^{24}$
2023-09-22	1.10	-	-	-	$8.84 \pm 0.52 \times 10^{24}$	-
2023-09-23	1.10	-	-	$9.25 \pm 0.45 \times 10^{24}$	$9.37 \pm 0.51 \times 10^{24}$	$1.94 \pm 0.13 \times 10^{24}$
2023-09-28	1.08	$2.94 \pm 0.48 \times 10^{27}$	$2.31 \pm 0.39 \times 10^{25}$	$8.71 \pm 0.49 \times 10^{24}$	$1.07 \pm 0.57 \times 10^{24}$	$1.98 \pm 0.20 \times 10^{24}$
2023-10-09	1.07	$3.21\pm 0.70 \times 10^{27}$	$2.81 \pm 0.34 \times 10^{25}$	$8.96 \pm 0.49 \times 10^{24}$	$11.32 \pm 0.57 \times 10^{24}$	-
2023-10-11	1.06	-	$2.90 \pm 0.39 \times 10^{25}$	$11.27 \pm 0.50 \times 10^{24}$	$12.35 \pm 0.54 \times 10^{24}$	$2.42 \pm 0.21 \times 10^{24}$
2023-10-12	1.06	$3.13 \pm 0.50 \times 10^{27}$	-	-	-	-
2023-10-25	1.08	-	-	$11.41 \pm 0.47 \times 10^{24}$	$12.45 \pm 0.42 \times 10^{24}$	$2.59 \pm 0.17 \times 10^{24}$
2023-10-26	1.08	-	-	$10.71 \pm 0.57 \times 10^{24}$	-	-
2023-11-02	1.10	$3.99 \pm 0.50 \times 10^{27}$	$2.70 \pm 0.37 \times 10^{25}$	-	$13.25 \pm 0.71 \times 10^{24}$	$2.37 \pm 0.40 \times 10^{24}$
2023-11-10	1.14	$3.12 \pm 0.45 \times 10^{27}$	$1.84 \pm 0.35 \times 10^{25}$	$8.81 \pm 0.30 \times 10^{24}$	$10.77 \pm 0.47 \times 10^{24}$	$1.75 \pm 0.11 \times 10^{24}$
2023-11-13	1.15	-	$1.47 \pm 0.22 \times 10^{25}$	$7.89 \pm 0.29 \times 10^{24}$	$10.29 \pm 0.35 \times 10^{24}$	$1.37 \pm 0.13 \times 10^{24}$
2023-11-14	1.16	-	$1.79 \pm 0.29 \times 10^{25}$	$7.25 \pm 0.33 \times 10^{24}$	$9.30 \pm 0.30 \times 10^{24}$	$1.45 \pm 0.11 \times 10^{24}$
2023-11-15	1.16	$2.44 \pm 0.37 \times 10^{27}$	-	$7.16 \pm 0.33 \times 10^{24}$	-	-
2023-11-16	1.17	$2.89 \pm 0.37 \times 10^{27}$	-	$8.75 \pm 0.33 \times 10^{24}$	$10.00 \pm 0.48 \times 10^{24}$	-
2023-11-18	1.18	$2.37 \pm 0.43 \times 10^{27}$	-	$6.91 \pm 0.29 \times 10^{24}$	$8.92 \pm 0.41 \times 10^{24}$	$1.39 \pm 0.16 \times 10^{24}$
2023-11-21	1.20	$1.73 \pm 0.29 \times 10^{27}$	-	$5.63 \pm 0.25 \times 10^{24}$	-	$1.18 \pm 0.14 \times 10^{24}$
2023-11-23	1.21	-	$1.81 \pm 0.32 \times 10^{25}$	$7.46 \pm 0.31 \times 10^{24}$	$7.88 \pm 0.58 \times 10^{24}$	$1.44 \pm 0.08 \times 10^{24}$
2023-11-27	1.23	$1.87 \pm 0.32 \times 10^{27}$	-	$6.20 \pm 0.30 \times 10^{24}$	$7.06 \pm 0.65 \times 10^{24}$	$1.17 \pm 0.16 \times 10^{24}$
2023-12-03	1.27	$1.73 \pm 0.40 \times 10^{27}$	-	$5.18 \pm 0.34 \times 10^{24}$	$5.80 \pm 1.07 \times 10^{24}$	$7.77 \pm 0.25 \times 10^{24}$
2023-12-04	1.28	$1.52 \pm 0.37 \times 10^{27}$	$6.42 \pm 4.68 \times 10^{24}$	$4.25 \pm 0.24 \times 10^{24}$	$4.59 \pm 0.63 \times 10^{24}$	$6.72 \pm 1.22 \times 10^{23}$
2023-12-07	1.30	-	-	-	-	$5.79 \pm 0.92 \times 10^{23}$
2023-12-20	1.40	-	-	-	$4.32 \pm 0.36 \times 10^{24}$	-
2023-12-22	1.42	$9.96 \pm 3.93 \times 10^{26}$	-	-	$4.31 \pm 0.85 \times 10^{24}$	-
2024-01-03	1.52	-	-	$3.46 \pm 0.42 \times 10^{24}$	$3.39 \pm 0.58 \times 10^{24}$	$5.79 \pm 2.05 \times 10^{23}$
2024-01-07	1.56	$3.95 \pm 3.47 \times 10^{26}$	-	-	$3.35 \pm 0.61 \times 10^{24}$	$4.94 \pm 1.56 \times 10^{23}$
2024-01-09	1.57	$5.59 \pm 43.70 \times 10^{25}$	-	-	-	-
2024-01-13	1.61	$8.94 \pm 55.74 \times 10^{25}$	-	$3.37 \pm 3.22 \times 10^{24}$	$2.71 \pm 0.50 \times 10^{24}$	$3.54 \pm 0.14 \times 10^{24}$
2024-01-22	1.69	-	-	$2.54 \pm 0.39 \times 10^{24}$	$2.06 \pm 1.05 \times 10^{24}$	-
2024-01-29	1.75	-	-	$2.40 \pm 0.49 \times 10^{24}$	$1.45 \pm 0.85 \times 10^{24}$	-
2024-02-02	1.78	-	-	$2.65 \pm 0.40 \times 10^{24}$	$1.45 \pm 0.67 \times 10^{24}$	-
2024-02-07	1.83	-	-	$2.18 \pm 0.34 \times 10^{24}$	$2.20 \pm 0.55 \times 10^{24}$	-
2024-02-12	1.87	-	-	$2.54 \pm 0.34 \times 10^{24}$	$1.74 \pm 0.79 \times 10^{24}$	-
2024-03-06	2.08	-	-	$1.03 \pm 0.32 \times 10^{24}$	-	-

[a] Heliocentric distance of the comet.

Table A.5. C_2-to-CN production rate ratios measured for the 2015 (left) and 2021 (right) perihelion passages of comet 67P.

Date	r_h [AU]	$\log[Q_{C_2}/Q_{CN}]$
2015-08-22/23	1.25	0.14 ± 0.06
2015-09-12/13	1.30	-0.26 ± 0.11
2015-12-09/10	1.85	0.07 ± 0.13

Date	r_h [AU]	$\log[Q_{C_2}/Q_{CN}]$
2021-09-04	1.41	-0.03 ± 0.09
2021-09-10	1.38	0.03 ± 0.05
2021-09-15	1.35	0.03 ± 0.06
2021-10-02	1.27	-0.04 ± 0.06
2021-11-10	1.24	-0.07 ± 0.08
2021-13-10	1.24	-0.05 ± 0.07
2021-10-16	1.23	-0.05 ± 0.06
2021-10-20	1.22	-0.02 ± 0.09
2021-10-30	1.21	-0.04 ± 0.07
2021-11-04	1.21	-0.02 ± 0.05
2021-11-07	1.21	-0.06 ± 0.04
2021-11-09	1.21	-0.06 ± 0.04
2021-11-12	1.22	-0.07 ± 0.05
2021-11-16	1.22	-0.08 ± 0.04
2021-11-20	1.23	-0.03 ± 0.06
2021-11-21	1.24	-0.02 ± 0.06
2021-11-30	1.26	-0.06 ± 0.04
2021-12-02	1.27	-0.08 ± 0.04
2021-12-05	1.28	-0.07 ± 0.05
2021-12-09	1.30	-0.02 ± 0.05
2021-12-16	1.33	0.01 ± 0.05
2021-12-31	1.41	0.03 ± 0.06
2022-01-01	1.42	0.07 ± 0.05
2022-01-05	1.45	0.02 ± 0.07
2022-01-07	1.46	0.07 ± 0.05
2022-01-08	1.46	0.09 ± 0.04
2022-01-10	1.48	0.10 ± 0.05
2022-02-02	1.64	0.11 ± 0.04
2022-02-03	1.65	0.13 ± 0.04
2022-02-05	1.66	-0.07 ± 0.09
2022-02-11	1.71	0.03 ± 0.06
2022-02-17	1.75	0.20 ± 0.19
2022-02-18	1.76	0.05 ± 0.29

Table A.6. C_2-to-CN production rate ratios measured for the 2010 (left) and 2023 (right) perihelion passages of comet 103P.

Date	r_h [AU]	$\log[Q_{C_2}/Q_{CN}]$
2010-12-10	1.21	0.05 ± 0.02
2010-12-12	1.22	0.08 ± 0.02
2010-12-13	1.23	0.06 ± 0.03
2010-12-14	1.24	0.03 ± 0.02
2010-12-15	1.25	0.07 ± 0.02
2010-12-16	1.25	0.07 ± 0.03
2010-12-17	1.26	0.04 ± 0.02
2010-12-18	1.27	0.06 ± 0.03
2010-12-19	1.27	0.07 ± 0.02
2010-12-20	1.28	0.06 ± 0.04
2010-12-21	1.29	0.02 ± 0.02
2010-12-22	1.30	0.04 ± 0.05
2010-12-27	1.33	0.03 ± 0.02
2010-12-29	1.35	0.04 ± 0.02
2010-12-30	1.36	0.05 ± 0.02
2011-12-01	1.37	-0.01 ± 0.03
2011-12-02	1.38	0.05 ± 0.04
2011-12-03	1.39	0.01 ± 0.02
2011-01-05	1.40	0.02 ± 0.05
2011-01-06	1.41	0.01 ± 0.02
2011-01-07	1.42	0.01 ± 0.03
2011-01-08	1.43	-0.03 ± 0.03
2011-01-09	1.44	0.02 ± 0.04
2011-01-11	1.45	-0.04 ± 0.04
2011-01-12	1.46	-0.03 ± 0.06
2011-01-13	1.47	-0.01 ± 0.07
2011-01-15	1.49	-0.06 ± 0.06
2011-01-17	1.50	-0.05 ± 0.05
2011-01-18	1.51	-0.11 ± 0.07
2011-01-19	1.52	-0.02 ± 0.10
2011-01-20	1.53	0.10 ± 0.13
2011-01-24	1.57	0.02 ± 0.04
2011-01-27	1.59	0.01 ± 0.06
2011-01-28	1.60	-0.07 ± 0.05
2011-02-20	1.80	0.10 ± 0.14
2011-02-24	1.84	-0.09 ± 0.26
2011-03-04	1.91	-0.11 ± 0.14

Date	r_h [AU]	$\log[Q_{C_2}/Q_{CN}]$
2023-07-21	1.53	0.01 ± 0.06
2023-08-16	1.32	0.00 ± 0.05
2023-08-19	1.29	0.03 ± 0.04
2023-08-22	1.27	0.04 ± 0.05
2023-08-27	1.23	0.05 ± 0.05
2023-08-28	1.23	0.04 ± 0.06
2023-08-30	1.22	0.04 ± 0.08
2023-09-17	1.12	0.03 ± 0.03
2023-09-23	1.10	0.01 ± 0.03
2023-09-28	1.08	0.09 ± 0.03
2023-10-09	1.07	0.10 ± 0.03
2023-10-11	1.06	0.04 ± 0.03
2023-10-25	1.08	0.04 ± 0.02
2023-11-10	1.14	0.09 ± 0.02
2023-11-13	1.15	0.12 ± 0.02
2023-11-14	1.16	0.11 ± 0.02
2023-11-16	1.17	0.06 ± 0.03
2023-11-18	1.18	0.11 ± 0.03
2023-11-23	1.21	0.02 ± 0.04
2023-11-27	1.23	0.06 ± 0.05
2023-12-03	1.27	0.05 ± 0.08
2023-12-04	1.28	0.03 ± 0.06
2024-01-03	1.52	-0.01 ± 0.09
2024-01-13	1.61	-0.09 ± 0.09
2024-01-22	1.69	-0.09 ± 0.23
2024-01-29	1.75	-0.21 ± 0.27
2024-02-02	1.78	-0.26 ± 0.21
2024-02-07	1.83	0.00 ± 0.13
2024-02-12	1.87	-0.16 ± 0.21

Appendix B

Computed $Af\rho$ parameters

Table B.1. Afrho parameter computed with the narrow-band dust filters for the 2015 perihelion passage of comet 67P, before ($A(\theta)f\rho$) and after ($A(0)f\rho$) the correction for the phase angle effect.

			Blue continuum		Green continuum		Red continuum	
Date	r_h [AU][a]	Phase angle [°]	$A(\theta)f\rho$ [cm]	$A(0)f\rho$ [cm]	$A(\theta)f\rho$ [cm]	$A(0)f\rho$ [cm]	$A(\theta)f\rho$ [cm]	$A(0)f\rho$ [cm]
2015-08-26	1.25	33.96	227.16 ± 22.82	583.20 ± 58.58	-	-	-	-
2015-09-02	1.27	33.91	246.78 ± 27.51	633.13 ± 70.58	-	-	-	-
2015-09-03	1.27	33.90	-	-	250.71 ± 10.86	643.12 ± 27.85	-	-
2015-09-04	1.27	33.89	-	-	-	-	369.07 ± 11.66	946.58 ± 29.91
2015-12-08	1.84	31.91	73.96 ± 16.85	184.23 ± 41.96	-	-	-	-
2015-12-09	1.85	31.83	-	-	86.72 ± 5.74	215.72 ± 14.28	111.94 ± 6.40	278.43 ± 15.92
2015-12-10	1.85	31.74	69.65 ± 11.17	173.01 ± 27.76	91.03 ± 4.46	226.12 ± 11.08	-	-

[a] Heliocentric distance of the comet.

Table B.2. Afrho parameter computed with the broad-band R filter for the 2015 perihelion passage of comet 67P, before ($A(\theta)f\rho$) and after ($A(0)f\rho$) the correction for the phase angle effect. Please note that, for the species observed several times over a given night, only the average value obtained is given.

Date	r_h [AU][a]	Phase angle [°]	$A(\theta)f\rho$ [cm]	$A(0)f\rho$ [cm]
2015-04-18	1.83	15.61	86.65 ± 3.06	150.16 ± 5.31
2015-04-25	1.78	17.20	77.29 ± 2.81	140.12 ± 5.09
2015-04-29	1.75	18.11	84.27 ± 3.28	156.61 ± 6.10
2015-05-04	1.71	19.23	84.80 ± 3.58	162.32 ± 6.86
2015-05-05	1.71	19.46	82.48 ± 3.16	158.79 ± 6.08
2015-05-12	1.66	21.01	81.22 ± 2.21	162.60 ± 4.43
2015-05-15	1.63	21.67	82.88 ± 2.63	168.58 ± 5.36
2015-05-16	1.63	21.88	74.25 ± 1.92	151.82 ± 3.94
2015-05-18	1.61	22.32	90.29 ± 1.39	186.48 ± 2.87
2015-05-19	1.60	22.75	92.48 ± 1.48	192.93 ± 3.10
2015-05-20	1.55	24.22	96.24 ± 1.40	207.55 ± 3.02
2015-05-30	1.53	24.84	102.51 ± 1.76	224.05 ± 3.85
2015-06-03	1.51	25.64	110.23 ± 1.98	245.05 ± 4.42
2015-06-05	1.49	26.04	101.11 ± 1.69	226.61 ± 3.80
2015-06-09	1.47	26.81	109.49 ± 1.33	249.18 ± 3.04
2015-06-12	1.45	27.37	114.76 ± 1.21	264.07 ± 2.78
2015-06-14	1.44	27.73	113.79 ± 0.89	263.68 ± 2.07
2015-06-15	1.43	27.92	113.21 ± 1.28	263.28 ± 2.98
2015-06-16	1.43	28.09	115.34 ± 0.94	269.12 ± 2.21
2015-06-18	1.42	28.44	123.65 ± 1.55	290.36 ± 3.63
2015-06-30	1.35	30.35	133.74 ± 1.78	324.81 ± 4.34
2015-07-02	1.34	30.63	139.00 ± 1.77	339.18 ± 4.32
2015-07-04	1.34	30.91	136.43 ± 1.91	334.47 ± 4.67
2015-07-07	1.32	31.29	149.54 ± 1.22	368.84 ± 3.01
2015-07-17	1.29	32.40	171.41 ± 1.60	430.14 ± 4.01
2015-07-18	1.28	32.49	172.67 ± 2.11	433.91 ± 5.29
2015-08-20	1.25	33.96	254.80 ± 3.78	654.11 ± 9.70
2015-08-21	1.25	33.96	326.01 ± 6.55	836.97 ± 16.81
2015-08-22	1.25	33.97	234.49 ± 5.09	602.04 ± 13.05
2015-08-23	1.25	33.97	337.79 ± 8.64	867.28 ± 22.17
2015-08-24	1.25	33.97	344.67 ± 7.60	884.94 ± 19.50
2015-08-26	1.25	33.96	329.18 ± 7.27	845.12 ± 18.67
2015-08-30	1.26	33.94	378.38 ± 9.22	971.13 ± 23.65
2015-09-02	1.27	33.91	367.83 ± 9.02	943.69 ± 23.15
2015-09-03	1.27	33.90	331.53 ± 7.67	850.44 ± 19.68
2015-09-04	1.27	33.89	363.88 ± 8.11	933.29 ± 20.81
2015-09-11	1.29	33.81	355.10 ± 8.55	909.62 ± 21.90
2015-09-12	1.30	33.79	359.61 ± 8.61	921.00 ± 22.04
2015-09-13	1.30	33.78	295.83 ± 6.90	757.51 ± 17.65
2015-09-17	1.32	33.73	338.92 ± 5.85	867.17 ± 14.98
2015-09-21	1.33	33.67	322.88 ± 6.37	825.49 ± 16.29
2015-09-26	1.36	33.61	307.76 ± 5.56	786.09 ± 14.20
2015-09-30	1.38	33.56	298.08 ± 5.40	760.87 ± 13.79
2015-10-02	1.39	33.54	265.12 ± 4.76	676.54 ± 12.15
2015-10-03	1.39	33.53	241.84 ± 6.03	617.07 ± 15.38
2015-10-16	1.47	33.43	225.77 ± 3.99	575.22 ± 10.15
2015-10-23	1.51	33.38	207.37 ± 3.86	527.98 ± 9.83
2015-10-27	1.54	33.35	181.65 ± 5.21	462.28 ± 13.26
2015-11-03	1.58	33.28	152.64 ± 5.08	388.07 ± 12.92
2015-11-08	1.62	33.21	160.41 ± 2.42	407.42 ± 6.13
2015-11-10	1.63	33.17	151.82 ± 2.85	385.39 ± 7.24
2015-11-13	1.65	33.11	150.84 ± 1.92	382.58 ± 4.87
2015-11-14	1.66	33.09	147.54 ± 2.45	374.08 ± 6.22
2015-11-15	1.67	33.06	140.89 ± 2.05	357.10 ± 5.19
2015-11-18	1.69	32.98	134.79 ± 1.90	341.23 ± 4.79
2015-11-20	1.70	32.91	130.65 ± 1.45	330.42 ± 3.68
2015-12-01	1.79	32.40	108.75 ± 4.35	272.90 ± 10.94
2015-12-08	1.84	31.91	101.69 ± 4.28	253.29 ± 10.65
2015-12-09	1.85	31.83	97.02 ± 1.80	241.34 ± 4.47
2015-12-10	1.85	31.74	106.75 ± 1.53	265.17 ± 3.80
2015-12-17	1.91	31.02	98.89 ± 2.69	242.87 ± 6.61
2015-12-24	1.96	30.09	85.83 ± 2.68	207.53 ± 6.48
2015-12-25	1.97	29.93	87.54 ± 2.70	211.08 ± 6.50
2016-01-10	2.09	26.73	78.09 ± 1.91	177.44 ± 4.35
2016-01-20	2.17	23.92	72.29 ± 0.83	154.87 ± 1.78
2016-01-30	2.25	20.44	69.27 ± 6.60	136.72 ± 13.02
2016-03-17	2.60	4.47	58.83 ± 1.14	70.24 ± 1.36
2016-03-19	2.61	5.02	49.62 ± 4.18	60.51 ± 5.22
2016-04-27	2.89	16.25	29.33 ± 3.18	51.77 ± 5.60
2016-04-30	2.91	16.72	35.26 ± 1.50	63.07 ± 2.68
2016-06-07	3.16	18.74	36.20 ± 1.90	68.41 ± 3.58
2016-06-27	3.28	17.50	22.31 ± 2.70	40.78 ± 4.93
2016-07-14	3.40	15.53	24.99 ± 4.59	43.21 ± 7.93

[a] Heliocentric distance of the comet.

Table B.3. Afrho parameter computed with the narrow-band dust filters for the 2021 perihelion passage of comet 67P, before ($A(\theta)f\rho$) and after ($A(0)f\rho$) the correction for the phase angle effect.

			Blue continuum		Green continuum		Red continuum	
Date	r_h [AU][a]	Phase angle [°]	$A(\theta)f\rho$ [cm]	$A(0)f\rho$ [cm]	$A(\theta)f\rho$ [cm]	$A(0)f\rho$ [cm]	$A(\theta)f\rho$ [cm]	$A(0)f\rho$ [cm]
2021-09-04	1.41	41.61	90.21 ± 8.32	251.56 ± 23.20	-	-	133.73 ± 3.51	372.93 ± 9.78
2021-09-10	1.38	41.61	-	-	-	-	148.46 ± 2.41	418.04 ± 6.78
2021-09-15	1.35	43.62	106.71 ± 6.82	303.10 ± 19.37	-	-	149.94 ± 3.16	425.87 ± 8.99
2021-10-01	1.27	46.82	123.79 ± 8.58	359.67 ± 24.94	-	-	185.62 ± 9.38	539.34 ± 27.27
2021-10-02	1.27	47.91	120.02 ± 7.06	349.12 ± 20.52	-	-	176.85 ± 7.06	514.42 ± 14.62
2021-10-11	1.24	48.61	139.83 ± 9.80	409.75 ± 28.71	-	-	191.94 ± 7.63	562.46 ± 22.36
2021-10-16	1.23	49.29	144.04 ± 26.35	423.14 ± 77.40	-	-	202.17 ± 7.25	593.92 ± 21.30
2021-10-20	1.22	49.70	-	-	-	-	217.15 ± 10.41	638.67 ± 30.63
2021-10-30	1.21	49.97	194.99 ± 10.42	573.95 ± 30.68	-	-	283.26 ± 9.62	833.76 ± 28.33
2021-11-04	1.21	49.62	204.99 ± 16.19	602.79 ± 47.60	-	-	296.62 ± 7.21	872.21 ± 21.21
2021-11-07	1.21	49.24	216.68 ± 13.56	636.43 ± 39.84	-	-	307.28 ± 7.63	902.54 ± 22.40
2021-11-08	1.21	49.09	219.00 ± 11.16	642.95 ± 32.76	-	-	313.39 ± 6.05	920.07 ± 17.76
2021-11-09	1.21	48.92	218.15 ± 19.50	640.07 ± 57.21	-	-	319.23 ± 6.56	936.67 ± 19.25
2021-11-11	1.22	48.52	222.14 ± 12.16	650.73 ± 35.62	244.29 ± 9.03	715.61 ± 26.44	322.64 ± 7.51	945.13 ± 21.99
2021-11-20	1.23	46.06	258.70 ± 28.70	748.37 ± 83.03	-	-	387.45 ± 9.53	1120.82 ± 27.56
2021-11-21	1.24	45.71	251.94 ± 31.05	727.08 ± 89.62	-	-	381.29 ± 11.95	1100.40 ± 34.48
2021-11-30	1.26	41.92	296.18 ± 20.64	827.93 ± 57.71	-	-	422.60 ± 7.81	1181.36 ± 21.82
2021-12-02	1.27	40.92	281.56 ± 18.68	780.90 ± 51.81	-	-	412.12 ± 8.56	1143.02 ± 23.74
2021-12-05	1.28	39.31	281.31 ± 16.66	769.14 ± 45.54	-	-	406.99 ± 7.81	1112.80 ± 21.35
2021-12-09	1.30	36.99	279.60 ± 22.03	746.07 ± 58.78	-	-	414.42 ± 7.94	1105.85 ± 21.19
2021-12-15	1.33	33.14	267.22 ± 24.73	677.98 ± 62.74	-	-	410.69 ± 8.59	1042.05 ± 21.79
2021-12-16	1.33	32.46	277.41 ± 18.02	696.71 ± 45.26	-	-	415.41 ± 6.49	1043.34 ± 16.29
2022-01-01	1.42	20.52	283.06 ± 24.60	559.82 ± 48.66	-	-	414.09 ± 8.82	819.01 ± 17.44
2022-01-05	1.45	17.40	290.33 ± 21.50	529.16 ± 39.18	-	-	421.48 ± 8.73	768.26 ± 15.91
2022-01-07	1.46	15.89	286.18 ± 13.34	500.10 ± 23.32	317.73 ± 11.03	555.18 ± 19.28	426.93 ± 9.69	745.92 ± 16.92
2022-01-08	1.46	15.18	282.09 ± 8.87	482.83 ± 15.18	323.90 ± 5.63	554.35 ± 9.64	424.82 ± 4.54	727.01 ± 7.77
2022-01-10	1.48	13.61	262.36 ± 20.49	428.47 ± 33.47	-	-	-	-
2022-02-01	1.63	7.96	220.65 ± 14.02	299.40 ± 19.03	-	-	-	-
2022-02-02	1.64	8.29	240.86 ± 7.86	330.63 ± 10.79	-	-	342.42 ± 7.54	470.06 ± 10.35
2022-02-03	1.65	8.76	220.205 ± 7.67	307.30 ± 10.71	-	-	319.12 ± 5.30	445.36 ± 7.40
2022-02-05	1.66	9.73	245.51 ± 13.71	353.99 ± 19.77	-	-	333.65 ± 8.38	481.15 ± 12.08
2022-02-10	1.71	12.75	198.45 ± 13.94	294.89 ± 20.92	-	-	276.85 ± 9.79	437.96 ± 15.49
2022-02-11	1.71	12.92	-	-	-	-	250.20 ± 16.64	400.13 ± 26.61
2022-02-17	1.75	15.19	144.31 ± 37.49	247.07 ± 64.19	-	-	245.76 ± 43.21	420.77 ± 73.99

[a] Heliocentric distance of the comet.

Table B.4. Afrho parameter computed with the broad-band R filter for the 2021 perihelion passage of comet 67P, before ($A(\theta)f\rho$) and after ($A(0)f\rho$) the correction for the phase angle effect. Please note that, for the species observed several times over a given night, only the average value obtained is given.

Date	r_h [AU][a]	Phase angle [°]	$A(\theta)f\rho$ [cm]	$A(0)f\rho$ [cm]
2021-05-11	2.28	24.36	42.43 ± 1.22	91.79 ± 2.64
2021-05-25	2.17	26.86	46.78 ± 1.89	106.59 ± 4.30
2021-06-06	2.08	28.86	54.01 ± 1.33	127.81 ± 3.15
2021-06-07	2.07	29.02	59.02 ± 1.38	140.08 ± 3.28
2021-06-19	1.98	30.87	73.26 ± 1.32	179.47 ± 3.22
2021-06-22	1.96	31.29	62.32 ± 1.13	153.70 ± 2.78
2021-06-23	1.95	31.44	65.55 ± 0.74	162.06 ± 1.84
2021-06-28	1.90	32.20	69.40 ± 1.00	173.62 ± 2.51
2021-07-08	1.83	33.59	75.44 ± 0.66	192.65 ± 1.68
2021-07-10	1.81	33.86	77.09 ± 0.88	197.61 ± 2.25
2021-07-14	1.78	34.36	71.84 ± 0.47	185.44 ± 1.22
2021-07-17	1.76	34.79	86.33 ± 0.67	224.14 ± 1.73
2021-07-21	1.73	35.31	86.55 ± 0.63	226.26 ± 1.66
2021-08-07	1.60	37.49	100.52 ± 0.65	269.71 ± 1.73
2021-08-09	1.58	37.76	95.10 ± 0.63	255.93 ± 1.70
2021-08-17	1.53	38.83	99.72 ± 0.65	271.40 ± 1.77
2021-09-03	1.42	41.44	116.36 ± 0.91	324.07 ± 2.53
2021-09-04	1.41	41.61	118.31 ± 1.75	329.93 ± 4.87
2021-09-10	1.38	42.67	132.47 ± 0.89	372.99 ± 2.50
2021-09-15	1.35	43.61	133.04 ± 0.74	377.85 ± 2.09
2021-10-01	1.27	46.81	159.59 ± 1.45	463.68 ± 4.21
2021-10-02	1.27	47.00	160.37 ± 1.44	466.48 ± 4.17
2021-10-13	1.24	48.90	183.10 ± 3.16	537.20 ± 9.28
2021-10-16	1.23	49.29	185.79 ± 2.66	545.79 ± 7.80
2021-10-20	1.22	49.70	200.79 ± 3.43	590.54 ± 10.08
2021-10-30	1.21	49.97	257.71 ± 2.45	758.56 ± 7.21
2021-11-04	1.21	49.62	269.78 ± 2.71	793.29 ± 7.96
2021-11-07	1.21	49.24	278.38 ± 2.59	817.67 ± 7.60
2021-11-08	1.21	49.09	285.81 ± 2.47	839.09 ± 7.26
2021-11-09	1.21	48.92	287.65 ± 3.01	844.00 ± 8.84
2021-11-11	1.22	48.52	292.89 ± 2.58	857.99 ± 7.56
2021-11-12	1.22	48.32	299.85 ± 2.82	877.64 ± 8.24
2021-11-16	1.22	47.31	315.19 ± 3.07	918.17 ± 8.95
2021-11-20	1.23	46.06	353.19 ± 3.52	1021.71 ± 10.20
2021-11-21	1.24	45.71	350.15± 3.85	1010.56 ± 11.11
2021-11-30	1.26	41.92	380.46 ± 2.57	1063.57 ± 7.18
2021-12-02	1.27	40.92	374.53 ± 2.54	1038.80 ± 7.05
2021-12-05	1.28	39.32	363.75 ± 2.33	994.62 ±6.38
2021-12-09	1.30	36.99	374.74 ± 2.33	1000.02 ± 6.23
2021-12-15	1.33	33.14	370.94 ± 3.20	941.24 ± 8.13
2021-12-16	1.33	32.46	381.89 ± 2.94	959.23 ± 7.39
2021-12-31	1.41	21.28	385.84 ± 6.25	777.46 ± 12.59
2022-01-01	1.42	20.52	368.62 ± 2.41	729.18 ± 4.76
2022-01-05	1.45	17.41	367.30 ± 2.36	669.63 ± 4.30
2022-01-07	1.46	15.95	393.60 ± 3.90	689.03 ± 6.83
2022-01-08	1.46	15.24	386.06 ± 2.92	662.05 ± 5.00
2022-01-10	1.48	13.65	286.50 ± 4.58	468.52 ± 7.49
2022-01-21	1.55	7.14	386.17 ± 11.153	508.94 ± 14.70
2022-02-01	1.63	7.94	265.30 ± 3.19	359.84 ± 4.33
2022-02-02	1.64	8.27	318.08 ± 2.28	436.31 ± 3.13
2022-02-03	1.65	8.72	289.59 ± 2.13	403.47 ± 2.97
2022-02-05	1.66	9.71	297.20 ± 3.09	428.33 ± 4.45
2022-02-10	1.71	12.43	219.34 ± 13.14	345.39 ± 20.70
2022-02-11	1.71	12.56	242.76 ± 3.07	383.81 ± 4.86
2022-02-12	1.71	12.92	219.65 ± 4.40	351.30 ± 7.04
2022-02-16	1.75	15.15	212.99 ± 22.76	364.31 ± 38.93
2022-02-17	1.75	15.20	221.39 ± 9.78	379.07 ± 16.74
2022-02-23	1.80	17.60	202.22 ± 2.49	370.63 ± 4.56

[a] Heliocentric distance of the comet.

Table B.5. Afrho parameter computed with the narrow-band dust filters for the 2010 perihelion passage of comet 103P, before ($A(\theta)f\rho$) and after ($A(0)f\rho$) the correction for the phase angle effect. Please note that, for the filters used several times over a given night, only the average value obtained is given.

			Blue continuum		Green continuum	
Date	r_h [AU][a]	Phase angle [°]	$A(\theta)f\rho$ [cm]	$A(0)f\rho$ [cm]	$A(\theta)f\rho$ [cm]	$A(0)f\rho$ [cm]
2010-12-09	1.21	42.16	-	-	59.15 ± 7.04	165.71 ± 19.73
2010-12-10	1.21	41.45	-	-	60.80 ± 2.55	170.34 ± 7.47
2010-12-12	1.22	40.10	-	-	56.30 ± 2.40	155.02 ± 6.61
2010-12-13	1.23	39.45	-	-	56.01 ± 4.89	153.33 ± 13.39
2010-12-14	1.24	38.70	-	-	55.87 ± 3.22	151.80 ± 8.75
2010-12-15	1.25	38.02	-	-	53.34 ± 3.07	143.94 ± 8.28
2010-12-16	1.25	37.41	-	-	55.12 ± 4.47	147.75 ± 11.97
2010-12-17	1.26	36.69	-	-	54.57 ± 3.31	145.07 ± 8.81
2010-12-18	1.27	35.99	-	-	56.80 ± 4.48	149.75 ± 11.80
2010-12-19	1.27	35.42	-	-	54.66 ± 3.11	142.34 ± 8.74
2010-12-20	1.28	34.77	-	-	50.90 ± 7.76	132.11 ± 20.13
2010-12-21	1.29	34.18	-	-	50.82 ± 3.46	132.85 ± 8.42
2010-12-22	1.30	33.46	-	-	44.57 ± 14.60	113.59 ± 37.21
2010-12-27	1.33	30.56	-	-	52.34 ± 2.84	128.89 ± 6.94
2010-12-29	1.35	29.51	-	-	54.00 ± 3.52	129.22 ± 8.43
2010-12-30	1.36	28.97	-	-	48.88 ± 2.97	135.85 ± 7.76
2011-01-01	1.37	27.95	-	-	54.71 ± 2.96	127.29 ± 6.88
2011-01-02	1.38	27.41	-	-	52.49 ± 4.97	120.86 ± 11.44
2011-01-05	1.40	26.10	-	-	48.70 ± 6.10	109.29 ± 13.69
2011-01-06	1.41	25.67	-	-	53.45 ± 2.78	118.84 ± 6.18
2011-01-07	1.42	25.24	-	-	56.02 ± 3.73	118.45 ± 13.71
2011-01-08	1.43	24.94	-	-	50.99 ± 4.79	111.69 ± 10.50
2011-01-09	1.44	24.57	-	-	52.37 ± 6.76	113.80 ± 14.68
2011-01-11	1.45	23.91	-	-	36.31 ± 6.78	109.79 ± 16.34
2011-01-15	1.49	22.88	-	-	52.78 ± 7.22	110.43 ± 15.11
2011-01-17	1.51	22.44	164.42 ± 8.66	129.98 ± 22.66	63.93 ± 5.82	125.83 ± 14.05
2011-01-18	1.51	22.30	53.66 ± 14.84	110.77 ± 30.63	50.78 ± 9.14	104.83 ± 18.87
2011-01-19	1.52	22.14	46.17 ± 24.62	94.97 ± 50.64	39.97 ± 18.97	82.21 ± 39.02
2011-01-20	1.53	22.02	45.06 ± 74.66	92.44 ± 153.18	46.61 ± 22.83	95.62 ± 46.84
2011-01-24	1.57	21.68	47.44 ± 7.99	96.50 ± 16.27	49.64 ± 3.92	100.99 ± 7.97
2011-01-26	1.58	21.61	24.99 ± 7.37	94.38 ± 29.81	-	-
2011-01-27	1.59	21.60	45.53 ± 6.75	92.44 ± 13.70	51.19 ± 4.59	103.93 ± 9.33
2011-01-28	1.60	21.60	47.70 ± 5.41	96.85 ± 10.99	52.10 ± 3.70	105.80 ± 7.52
2011-02-16	1.77	23.29	33.20 ± 27.51	49.90 ± 130.87	37.55 ± 17.03	69.51 ± 42.47
2011-02-20	1.81	23.78	24.34 ± 30.57	51.98 ± 65.29	28.17 ± 17.69	60.16 ± 37.78
2011-03-04	1.91	25.11	29.00 ± 9.86	63.77 ± 21.69	23.56 ± 7.02	51.80 ± 15.43

[a] Heliocentric distance of the comet.

Table B.6. Afrho parameter computed with the narrow-band dust filters for the 2023 perihelion passage of comet 103P, before ($A(\theta)f\rho$) and after ($A(0)f\rho$) the correction for the phase angle effect.

Date	r_h [AU][a]	Phase angle [°]	Blue continuum		Green continuum		Red continuum	
			$A(\theta)f\rho$ [cm]	$A(0)f\rho$ [cm]	$A(\theta)f\rho$ [cm]	$A(0)f\rho$ [cm]	$A(\theta)f\rho$ [cm]	$A(0)f\rho$ [cm]
2023-07-21	1.53	38.68	3.76 ± 4.94	10.22 ± 13.43	5.25 ± 2.49	14.27 ± 6.77	5.61 ± 2.72	15.24 ± 7.40
2023-07-26	1.49	39.83	6.43 ± 5.38	17.68 ± 14.78	6.45 ± 2.64	17.71 ± 7.25	8.35 ± 2.38	22.93 ± 6.54
2023-07-28	1.47	40.33	8.00 ± 3.32	22.08 ± 9.15	7.66 ± 2.36	21.13 ± 6.51	8.09 ± 2.18	22.33 ± 6.02
2023-08-07	1.39	43.22	6.13 ± 6.96	17.34 ± 19.71	-	-	-	-
2023-08-15	1.32	46.13	-	-	-	-	8.16 ± 1.43	23.62 ± 4.13
2023-08-16	1.32	46.51	-	-	-	-	8.62 ± 1.37	25.01 ± 3.96
2023-08-19	1.29	47.78	6.33 ± 3.23	18.49 ± 9.44	-	-	9.43 ± 2.14	27.52 ± 6.26
2023-08-22	1.27	49.13	5.92 ± 2.65	17.39 ± 7.78	-	-	8.40 ± 1.70	24.67 ± 4.99
2023-08-26	1.24	51.51	-	-	6.58 ± 3.23	19.44 ± 9.54	7.59 ± 2.74	22.42 ± 8.10
2023-08-28	1.23	52.04	7.89 ± 7.90	23.31 ± 23.33	8.27 ± 3.78	24.44 ± 11.17	9.52 ± 2.18	28.12 ± 6.44
2023-08-30	1.22	53.09	8.43 ± 9.80	24.91 ± 28.97	-	-	15.28 ± 2.41	45.18 ± 7.11
2023-09-01	1.21	54.20	9.13 ± 12.88	26.97 ± 38.04	-	-	-	-
2023-09-17	1.12	63.03	15.57 ± 6.16	44.25 ± 17.52	-	-	21.98 ± 7.77	62.48 ± 22.10
2023-09-22	1.10	65.43	18.25 ± 4.54	50.84 ± 12.65	-	-	-	-
2023-09-28	1.08	67.74	15.87 ± 8.88	43.22 ± 24.18	-	-	24.76 ± 2.77	67.41 ± 7.55
2023-10-03	1.07	69.01	18.00 ± 7.55	48.32 ± 20.26	-	-	-	-
2023-10-09	1.07	69.67	-	-	-	-	25.00 ± 3.32	66.59 ± 8.86
2023-10-11	1.06	69.69	22.20 ± 4.85	59.14 ± 12.92	23.64 ± 2.93	62.97 ± 7.81	25.24 ± 3.04	67.22 ± 8.11
2023-10-12	1.06	69.66	-	-	26.08 ± 3.80	69.48 ± 10.13	27.77 ± 2.71	73.99 ± 7.21
2023-10-25	1.08	67.22	26.60 ± 3.38	72.81 ± 9.26	-	-	29.59 ± 4.60	81.00 ± 12.59
2023-10-26	1.08	66.91	28.48 ± 8.54	78.20 ± 23.45	-	-	-	-
2023-11-02	1.10	64.28	26.82 ± 12.80	75.46 ± 36.01	-	-	32.87 ± 5.59	92.46 ± 15.72
2023-11-10	1.14	60.63	26.04 ± 2.79	75.19 ± 8.06	-	-	28.65 ± 2.11	82.75 ± 6.11
2023-11-13	1.15	59.13	24.53 ± 2.50	71.44 ± 7.29	-	-	27.70 ± 3.12	80.64 ± 9.08
2023-11-14	1.16	58.61	22.02 ± 4.19	64.26 ± 12.23	-	-	28.06 ± 2.48	81.89 ± 7.24
2023-11-15	1.16	58.09	23.65 ± 2.56	69.15 ± 7.49	-	-	-	-
2023-11-16	1.17	57.57	23.74 ± 2.50	69.57 ± 7.32	24.51 ± 2.04	71.84 ± 5.99	-	-
2023-11-18	1.18	56.52	21.87 ± 3.39	64.30 ± 9.97	21.39 ± 2.32	62.89 ± 6.81	-	-
2023-11-23	1.21	53.73	20.88 ± 4.24	61.69 ± 12.53	19.22 ± 2.08	56.80 ± 6.16	26.39 ± 1.87	77.99 ± 5.53
2023-11-27	1.23	51.45	20.25 ± 7.91	59.77 ± 23.35	21.11 ± 4.57	62.32 ± 13.49	26.17 ± 3.67	77.27 ± 10.85
2023-12-03	1.27	47.88	20.13 ± 7.28	58.82 ± 21.26	20.22 ± 5.43	59.09 ± 15.86	23.67 ± 6.15	69.16 ± 17.97
2023-12-04	1.28	47.29	16.33 ± 5.08	47.58 ± 14.80	-	-	21.01 ± 3.64	61.21 ± 10.62
2023-12-07	1.30	45.41	14.19 ± 4.79	40.86 ± 13.79	-	-	18.50 ± 2.33	53.28 ± 6.71
2023-12-20	1.40	37.21	20.95 ± 4.63	56.04 ± 12.38	19.25 ± 3.63	51.49 ± 9.70	22.54 ± 3.29	60.29 ± 8.81
2023-12-22	1.42	35.79	21.39 ± 7.61	56.26 ± 20.02	-	-	-	-
2024-01-03	1.52	28.05	19.09 ± 10.79	44.51 ± 25.16	20.46 ± 4.87	47.70 ± 11.35	23.78 ± 6.25	55.43 ± 14.57
2024-01-09	1.57	24.40	-	-	17.40 ± 5.57	37.67 ± 12.06	-	-
2024-01-13	1.61	22.18	-	-	14.57 ± 4.95	30.00 ± 10.19	-	-
2024-01-22	1.69	18.18	24.37 ± 19.46	45.38 ± 36.23	-	-	23.95 ± 5.62	44.59 ± 10.46
2024-01-29	1.75	16.32	25.29 ± 18.49	44.73 ± 32.70	-	-	28.80 ± 7.09	50.94 ± 12.54
2024-02-02	1.78	15.84	21.95 ± 13.58	38.31 ± 23.70	-	-	29.81 ± 5.42	52.02 ± 9.46
2024-02-12	1.87	16.25	25.26 ± 7.51	44.58 ± 13.26	-	-	30.00 ± 6.70	52.95 ± 11.82
2024-03-06	2.08	20.51	12.37 ± 7.38	24.46 ± 14.59	-	-	18.28 ± 6.08	36.15 ± 12.01

[a] Heliocentric distance of the comet.

Table B.7. Afrho parameter computed with the broad-band R filter for the 2023 perihelion passage of comet 103P, before ($A(\theta)f\rho$) and after ($A(0)f\rho$) the correction for the phase angle effect. Please note that, for the species observed several times over a given night, only the average value obtained is given.

Date	r_h [AU][a]	Phase angle [°]	$A(\theta)f\rho$ [cm]	$A(0)f\rho$ [cm]
2023-06-23	1.77	33.96	5.98 ± 0.63	15.35 ± 1.63
2023-06-27	1.74	34.54	5.70 ± 0.61	14.76 ± 1.58
2023-07-21	1.53	38.67	6.39 ± 0.41	17.36 ± 1.13
2023-07-26	1.49	39.82	7.50 ± 0.33	20.62 ± 0.92
2023-07-28	1.47	40.31	8.34 ± 0.36	23.01 ± 1.01
2023-08-02	1.43	41.73	9.40 ± 1.48	26.25 ± 4.15
2023-08-15	1.32	46.12	9.23 ± 0.49	26.73 ± 1.42
2023-08-16	1.32	46.50	9.31 ± 0.41	27.02 ± 1.21
2023-08-19	1.29	47.76	9.91 ± 0.47	28.94 ± 1.39
2023-08-22	1.27	49.11	10.37 ± 0.42	30.46 ± 1.24
2023-08-27	1.23	52.02	11.95 ± 1.05	35.32 ± 3.11
2023-08-30	1.22	53.08	13.96 ± 1.39	41.26 ± 4.13
2023-08-31	1.21	54.19	11.59 ± 2.09	34.23 ± 6.19
2023-09-17	1.12	63.01	25.17 ± 2.84	71.56 ± 8.09
2023-09-22	1.10	65.42	27.12 ± 1.10	75.56 ± 3.07
2023-09-26	1.09	67.03	28.88 ± 1.42	79.21 ± 3.91
2023-09-27	1.09	67.41	30.64 ± 3.02	83.71 ± 8.26
2023-09-28	1.08	67.73	30.45 ± 2.47	82.90 ± 6.74
2023-09-30	1.08	68.38	32.84 ± 2.08	88.79 ± 5.62
2023-10-01	1.08	68.55	33.69 ± 4.98	90.93 ± 13.44
2023-10-09	1.07	69.67	33.35 ± 1.28	88.86 ± 3.43
2023-10-11	1.06	69.68	34.38 ± 1.20	91.59 ± 3.20
2023-10-12	1.06	69.65	35.21 ± 2.19	93.82 ± 5.83
2023-10-25	1.08	67.22	40.15 ± 1.13	109.89 ± 3.09
2023-10-26	1.08	66.91	39.56 ± 1.22	108.63 ± 3.35
2023-11-02	1.10	64.28	43.63 ± 1.86	122.76 ± 5.25
2023-11-10	1.14	60.63	34.93 ± 0.71	100.89 ± 2.07
2023-11-13	1.15	59.13	35.88 ± 0.76	104.48 ± 2.22
2023-11-14	1.16	58.62	32.54 ± 0.71	94.98 ± 2.09
2023-11-15	1.16	58.09	31.48 ± 2.01	92.07 ± 5.89
2023-11-16	1.17	57.57	34.30 ± 1.59	100.53 ± 4.66
2023-11-18	1.18	56.52	31.17 ± 1.63	91.68 ± 4.80
2023-11-23	1.21	53.74	30.00 ± 1.23	88.64 ± 3.64
2023-11-27	1.23	51.46	28.09 ± 2.13	82.94 ± 6.31
2023-12-03	1.27	47.90	26.33 ± 1.62	76.95 ± 4.73
2023-12-04	1.28	47.30	23.50 ± 0.96	68.45 ± 2.81
2023-12-15	1.36	40.40	21.74 ± 0.59	60.04 ± 1.63
2023-12-18	1.39	38.45	22.49 ± 0.79	60.97 ± 2.15
2023-12-20	1.40	37.22	22.13 ± 2.19	59.22 ± 5.86
2023-12-22	1.42	35.82	23.48 ± 1.56	61.79 ± 4.10
2024-01-03	1.52	28.08	22.80 ± 1.42	53.19 ± 3.32
2024-01-22	1.69	18.18	25.89 ± 2.00	48.22 ± 3.74
2024-01-29	1.75	16.32	27.86 ± 3.43	49.28 ± 6.07
2024-02-02	1.78	15.84	29.41 ± 1.91	51.32 ± 3.34
2024-02-07	1.83	15.79	28.97 ± 1.46	50.49 ± 2.55
2024-02-12	1.87	16.24	30.62 ± 1.79	54.05 ± 3.16
2024-03-05	2.08	20.50	17.10 ± 2.86	33.82 ± 5.66
2024-03-06	2.08	20.51	9.43 ± 4.41	18.66 ± 8.73

[a] Heliocentric distance of the comet.

Table B.8. Ratios of $A(0)f\rho$ (R) values and CN production rates measured for the 2015 (left) and 2021 (right) perihelion passages of comet 67P.

Date	r_h [AU]	$\log[Af\rho/Q_{\rm CN}]$
2015-08-22	1.25	-21.99 ± 0.05
2015-08-24	1.25	-21.89 ± 0.05
2015-09-11	1.29	-21.94 ± 0.05
2015-09-12	1.30	-21.96 ± 0.05
2015-12-01	1.79	-21.87 ± 0.08
2015-12-09	1.85	-21.90 ± 0.09
2015-12-17	1.91	-21.92 ± 0.07

Date	r_h [AU]	$\log[Af\rho/Q_{\rm CN}]$
2021-09-04	1.41	-21.73 ± 0.06
2021-09-10	1.38	-21.86 ± 0.03
2021-09-15	1.35	-21.85 ± 0.04
2021-10-02	1.27	-21.97 ± 0.03
2021-10-13	1.24	-22.00 ± 0.04
2021-10-16	1.23	-22.07 ± 0.04
2021-10-20	1.22	-22.01 ± 0.05
2021-10-30	1.21	-22.03 ± 0.04
2021-11-04	1.21	-22.04 ± 0.03
2021-11-07	1.21	-22.09 ± 0.03
2021-11-09	1.21	-22.10 ± 0.03
2021-11-12	1.22	-22.09 ± 0.04
2021-11-16	1.22	-22.05 ± 0.03
2021-11-20	1.23	-22.04 ± 0.04
2021-11-21	1.24	-22.05 ± 0.04
2021-11-30	1.26	-22.04 ± 0.04
2021-12-02	1.27	-22.06 ± 0.03
2021-12-05	1.28	-22.03 ± 0.03
2021-12-09	1.30	-22.01 ± 0.04
2021-12-15	1.33	-22.01 ± 0.03
2021-12-16	1.33	-22.00 ± 0.03
2021-12-31	1.41	-22.00 ± 0.04
2022-01-01	1.42	-22.00 ± 0.05
2022-01-05	1.45	-21.97 ± 0.06
2022-01-07	1.46	-22.03 ± 0.04
2022-01-08	1.46	-22.01 ± 0.02
2022-01-10	1.48	-22.18 ± 0.04
2022-01-21	1.55	-22.06 ± 0.05
2022-02-02	1.64	-22.04 ± 0.03
2022-02-03	1.65	-22.02 ± 0.03
2022-02-05	1.66	-22.07 ± 0.06
2022-02-10	1.71	-21.98 ± 0.07
2022-02-11	1.71	-21.98 ± 0.05
2022-02-17	1.75	-21.94 ± 0.07

Table B.9. Ratios of $A(0)f\rho$ (GC) values and CN production rates measured for the 2010 (left) and 2023 (right) perihelion passages of comet 103P.

Date	r_h [AU]	$\log[Af\rho/Q_{\rm CN}]$
2010-12-10	1.21	-23.02 ± 0.02
2010-12-12	1.22	-23.00 ± 0.02
2010-12-13	1.23	-23.00 ± 0.04
2010-12-14	1.24	-23.07 ± 0.03
2010-12-15	1.25	-23.00 ± 0.03
2010-12-16	1.25	-22.98 ± 0.04
2010-12-17	1.26	-22.99 ± 0.03
2010-12-18	1.27	-22.94 ± 0.04
2010-12-19	1.27	-22.94 ± 0.03
2010-12-20	1.28	-22.91 ± 0.07
2010-12-21	1.29	-22.97 ± 0.03
2010-12-22	1.30	-22.98 ± 0.15
2010-12-27	1.33	-22.86 ± 0.03
2010-12-29	1.35	-22.89 ± 0.03
2010-12-30	1.36	-22.79 ± 0.03
2011-01-01	1.37	-22.89 ± 0.03
2011-01-02	1.38	-22.79 ± 0.05
2011-01-05	1.40	-22.88 ± 0.06
2011-01-06	1.41	-22.82 ± 0.03
2011-01-07	1.42	-22.86 ± 0.05
2011-01-08	1.43	-22.89 ± 0.04
2011-01-09	1.44	-22.83 ± 0.06
2011-01-11	1.45	-22.82 ± 0.07
2011-01-15	1.49	-22.79 ± 0.07
2011-01-17	1.51	-22.71 ± 0.06
2011-01-18	1.51	-22.79 ± 0.08
2011-01-19	1.52	-22.81 ± 0.21
2011-01-20	1.53	-22.67 ± 0.22
2011-01-24	1.57	-22.75 ± 0.04
2011-01-27	1.59	-22.62 ± 0.05
2011-01-28	1.60	-22.76 ± 0.04
2011-02-16	1.77	-22.66 ± 0.27
2011-02-20	1.81	-22.74 ± 0.29
2011-03-04	1.91	-22.65 ± 0.14

Date	r_h [AU]	$\log[Af\rho/Q_{\rm CN}]$
2023-07-21	1.53	-23.10 ± 0.21
2023-07-26	1.49	-23.09 ± 0.18
2023-07-28	1.47	-23.01 ± 0.14
2023-08-28	1.23	-23.18 ± 0.20
2023-10-11	1.06	-23.25 ± 0.06
2023-11-16	1.17	-23.09 ± 0.04
2023-11-18	1.18	-23.04 ± 0.05
2023-11-23	1.21	-23.12 ± 0.05
2023-11-27	1.23	-23.00 ± 0.10
2023-12-03	1.27	-22.94 ± 0.12
2024-01-03	1.52	-22.86 ± 0.12
2024-01-13	1.61	-23.05 ± 0.15

Bibliography

A'Hearn Michael F, Millis Robert C, Schleicher David G, Osip David J, Birch Peter V. The ensemble properties of comets: Results from narrowband photometry of 85 comets, 1976-1992 // Icarus. 1995. 118, 2. 223–270.

A'Hearn Michael F, Schleicher DG, Millis RL, Feldman PD, Thompson Don T. Comet bowell 1980b // Astronomical Journal (ISSN 0004-6256), vol. 89, April 1984, p. 579-591. 1984. 89. 579–591.

Dynamical evolution of short-period comets. // . 1987.

Cochran Anita L, Levasseur-Regourd Anny-Chantal, Cordiner Martin, Hadamcik Edith, Lasue Jérémie, Gicquel Adeline, Schleicher David G, Charnley Steven B, Mumma Michael J, Paganini Lucas, others . The composition of comets // Space Science Reviews. 2015. 197. 9–46.

Cochran Anita L, Schleicher David G. Observational constraints on the lifetime of cometary H2O // Icarus. 1993. 105, 1. 235–253.

De Pater Imke, Lissauer Jack J. Planetary sciences. 2015.

Farnham Tony L. Coma morphology of Jupiter-family comets // Planetary and Space Science. 2009. 57, 10. 1192–1217.

Farnham Tony L, Schleicher David G, A'Hearn Michael F. The HB narrowband comet filters: Standard stars and calibrations // Icarus. 2000. 147, 1. 180–204.

Feldman Paul D, A'hearn Michael F, Feaga Lori M, Bertaux Jean-Loup, Noonan John, Parker Joel Wm, Schindhelm Rebecca N, Steffl Andrew J, Stern S Alan, Weaver Harold A. The nature and frequency of the gas outbursts in comet 67P/Churyumov–Gerasimenko observed by the Alice far-ultraviolet spectrograph on Rosetta // The Astrophysical journal letters. 2016. 825, 1. L8.

Festou MC, Keller HU, Weaver HA. A brief conceptual history of cometary science // Comets II. 2004. 3–16.

Festou Michel C. The density distribution of neutral compounds in cometary atmospheres. I-Models and equations // Astronomy and Astrophysics, vol. 95, no. 1, Feb. 1981, p. 69-79. 1981. 95. 69–79.

Groussin O, Lamy P, Jorda L, Toth I. The nuclei of comets 126P/IRAS and 103P/Hartley 2 // Astronomy & Astrophysics. 2004. 419, 1. 375–383.

Haser L, Oset Shawn, Bodewits D. Intensity distribution in the heads of comets // The Planetary Science Journal. 2020. 1, 3. 83.

Haser Leo. Distribution d'intensité dans la tête d'une comète // Bulletins de l'Académie Royale de Belgique. 1957. 43, 1. 740–750.

Holmberg Johan, Flynn Chris, Portinari Laura. The colours of the Sun // Monthly Notices of the Royal Astronomical Society. 2006. 367, 2. 449–453.

Jehin Emmanuël, Gillon Michaël, Queloz Didier, Magain Pierre, Manfroid Jean, Chantry Virginie, Lendl Monica, Hutsemékers Damien, Udry Stephane. TRAPPIST: TRAnsiting planets and PlanetesImals small telescope // The Messenger. 2011. 145, 2.

Knight Matthew M, Schleicher David G. The highly unusual outgassing of Comet 103P/Hartley 2 from narrowband photometry and imaging of the coma // Icarus. 2013. 222, 2. 691–706.

Lamy Philippe L, Toth I, Weaver HA, Jorda L, Kaasalainen Mikko, Gutiérrez PJ. Hubble Space Telescope observations of the nucleus and inner coma of comet 67P/Churyumov-Gerasimenko // Astronomy & Astrophysics. 2006. 458, 2. 669–678.

Lamy Philippe L, Toth Imre, Davidsson Björn JR, Groussin Olivier, Gutiérrez Pedro, Jorda Laurent, Kaasalainen Mikko, Lowry Stephen C. A portrait of the nucleus of comet 67P/Churyumov-Gerasimenko // Space science reviews. 2007. 128. 23–66.

Lamy Philippe L, Toth Imre, Fernández Yanga R, Weaver Harold A, others . The sizes, shapes, albedos, and colors of cometary nuclei // Comets II. 2004. 1. 223–264.

Lara Luisa María, Lin Z-Y, Rodrigo R, Ip W-H. 67P/Churyumov-Gerasimenko activity evolution during its last perihelion before the Rosetta encounter // Astronomy & Astrophysics. 2011. 525. A36.

Meierhenrich Uwe. Comets and their origin: the tools to decipher a comet. 2014.

Opitom C, Snodgrass Colin, Fitzsimmons A, Jehin Emmanuel, Manfroid Jean, Tozzi GP, Faggi S, Gillon Michaël. Ground-based monitoring of comet 67P/Churyumov–Gerasimenko gas activity throughout the Rosetta mission // Monthly Notices of the Royal Astronomical Society. 2017. 469, Suppl_2. S222–S229.

Rinaldi GIOVANNA, Bockelée-Morvan D, Ciarniello Mauro, Tozzi G P, Capaccioni FABRIZIO, Ivanovski S L, Filacchione GIANRICO, Fink U, Doose L, Taylor F, others . Summer outbursts

in the coma of comet 67P/Churyumov–Gerasimenko as observed by Rosetta–VIRTIS // Monthly Notices of the Royal Astronomical Society. 2018. 481, 1. 1235–1250.

Schleicher David G, A'Hearn Michael F. The fluorescence of cometary OH // Astrophysical Journal, Part 1 (ISSN 0004-637X), vol. 331, Aug. 15, 1988, p. 1058-1077. Research supported by the Lowell Observatory Research Fund. 1988. 331. 1058–1077.

Snodgrass Colin, A'Hearn Michael F, Aceituno Francisco, Afanasiev Viktor, Bagnulo Sefano, Bauer J, Bergond G, Besse S, Biver Nicolas, Bodewits Dennis, others . The 67P/Churyumov–Gerasimenko observation campaign in support of the Rosetta mission // Philosophical Transactions of the Royal Society A: Mathematical, Physical and Engineering Sciences. 2017. 375, 2097. 20160249.

Snodgrass Colin, Opitom Cyrielle, Val-Borro Miguel de, Jehin Emmanuel, Manfroid Jean, Lister Tim, Marchant Jon, Jones Geraint H, Fitzsimmons Alan, Steele Iain A, others . The perihelion activity of comet 67P/Churyumov–Gerasimenko as seen by robotic telescopes // Monthly Notices of the Royal Astronomical Society. 2016. 462, Suppl_1. S138–S145.

Solontoi Michael, Ivezić Željko, Jurić Mario, Becker Andrew C, Jones Lynne, West Andrew A, Kent Steve, Lupton Robert H, Claire Mark, Knapp Gillian R, others . Ensemble properties of comets in the Sloan Digital Sky Survey // Icarus. 2012. 218, 1. 571–584.

Swamy KS Krishna. Physics of comets. 12. 2010.

Thomas Nicolas. An Introduction to Comets: Post-Rosetta Perspectives. 2020.

Weidenschilling SJ. From icy grains to comets // Comets II. 2004. 745. 97–104.

Whipple Fred L. A comet model. I. The acceleration of Comet Encke // Astrophysical Journal, vol. 111, p. 375-394 (1950). 1950. 111. 375–394.